Magnetic Devices and Techniques for the Study of Viscoelasticity of Biomaterials and Myocardial Forces

Kevin Bielawski

A dissertation
submitted in partial fulfillment of the
requirements for the degree of

Doctor of Philosophy

University of Washington

2016

Reading Committee:

Nathan J. Sniadecki, Chair

Santosh Devasia

Nathan J. White

Program Authorized to Offer Degree:
Mechanical Engineering

University of Washington

Abstract

Magnetic Devices and Techniques for the Study of Viscoelasticity of Biomaterials and Myocardial Forces

Kevin Bielawski

Chair of the Supervisory Committee:
Associate Professor Nathan J. Sniadecki
Mechanical Engineering

Magnetic microdevices comprise a set of popular tools to study a number of properties of biological systems. In particular, magnetic microdevices are useful as methods to apply force to systems, and to measure the force being produced. One of the great benefits of using magnetic devices is the ability to produce force from a distance, and to develop devices that work *in situ*. Many systems, especially biological systems, have changes that occur between samples, even when split from the same sample, so the ability to measure trends on the same sample is ideal. Additionally, some materials may be valuable, and the ability to run multiple tests using large volumes is not possible. One particular application of this is the measurement of platelet viscoelasticity under shear flows. Traditionally, multiple blood samples are run through several different analysis systems to generate the desired data on the functionality of platelets. One of the intentions of my thesis is to develop new devices to measure elasticity of the shear-developed platelet clots *in situ*. In addition to applying forces to biomaterials, magnetic microdevices can also be useful for measuring forces without the need for a microscope and intensive imaging systems. The final aim of my thesis is to develop a force sensing device for the measurement of cardiomyocyte forces without the need for a microscope. I have split my thesis into three specific aims that I plan to accomplish to meet the goals described above: *AIM 1*: Fabricate and characterize a

microfluidic device to measure viscoelasticity, *AIM 2*: Miniaturize the magnetic device for use in a shear flow device to measure platelet elasticity, *AIM 3*: Create a magnetic sensor for measuring cardiomyocyte twitch forces. Each of these three aims involves creating new magnetic devices and showcasing them in experiments to demonstrate their utilities. In aim 1, experiments are run with collagen gels to demonstrate the ability of the new tool to measure viscoelasticity. In aim 2, the device is miniaturized and placed into microfluidic flow channels. Whole blood is run through the channels to form platelet plugs, then *in situ* testing is used to measure the modulus of the platelet plugs. In aim 3, engineered heart tissues derived from induced pluripotent stem cells are formed between two posts, and the force generated by the tissues can be monitored in real time and in parallel by monitoring the change in field of a magnet embedded in a flexible post. Through these three aims, new information about the nature of mechano-biological systems can be understood by either gathering information that was unknown before, or by enabling an easier method for monitoring the condition of cells. This work demonstrates the use of these three devices and has impact on future directions for understanding of the role of platelets in clot elasticity, and for measuring cardiotoxicity in drug screening platforms.

TABLE OF CONTENTS

LIST OF FIGURES

LIST OF TABLES

ACKNOWLEDGMENTS

I would like to thank my committee: Dr. Nathan J. Sniadecki, Dr. Santosh Devasia, Dr. Nathan J. White, and Dr. Lilo D. Pozzo. I would also like to thank all of the members of the Cell Biomechanics Lab who have been instrumental in my ability to accoplish the tasks described in this thesis. I would like to thank Dr. Andrea Leonard and Shiv Bhandari for their help in differentiating and cultruing myocardial tissues and making devices described and used in Chapter 6, Nikita Taparia and Kimsey Platten for their help with running experiments described in Chapter 4, and Jasdip Singh for help in manufacturing devices used in Chapter 4. The rest of the Cell Biomechanics Lab has helped focus and generate ideas described through the thesis, as well as providing motivation to complete the work: Dr. Lucas Ting, Annie Smith, Kevin Beussman, Dr. Zeinab Al-Rekabi, Dr. Ari Karchin, Dr. Shirin Feghhi, Dr. Marita Rodriguez, Dr. Sangyoon Han, and Wes Tooley. I would also like to thank several people for helpful conversations about this work, including Prof. Kannan M. Krishnan for useful discussions on magnetic sensing, Prof. Joseph Garbini for helpful talks on system analysis, Prof. Leslie Rosenberg for more discussions on magnetic sensing, and Prof. Chuck Murry for help on cardiomycyte development. I would also like to thank my parents and family for their support and encouragement as I have been working on my thesis. Furthermore, I would like to thank my friends and biking group in Seattle and abroad who have encouraged, supported, and distracted me from my thesis and helped to make it a fufilling experience. There are countless many more people not mentioned here that are also deserving of acknowledgment as well.

Chapter 1

INTRODUCTION

The advent of microfabrication has enabled new tools to study mechanical characteristics of cells and biological substances at a microscopic level [26, 94, 2, 23, 105, 132]. These tools have often made use of soft polymeric materials [117, 29, 52, 72, 94, 51], such as polydimethylsiloxane (PDMS) . Additionally, PDMS has been enhanced with the use of magnetic materials in order to produce forces on the material of interest [113, 4, 10, 93, 20, 122]. In order to translate knowledge about mechanics of cells to clinical settings, new tools need to be developed to produce real-time data, novel configurations, *in situ* measurements, and smaller devices. This thesis will seek to identify areas of need for new magnetic microdevices, present new devices, and show the usefulness of the new tools used to study cell mechanics and biological materials.

1.1 Basics of Magnetism

Devices using magnets have been used for over a thousand years from compasses to computer hard drives [25]. Magnetic interactions are from the spin of electrons, and Maxwell derived equations to describe the close interactions between electric fields and magnetic forces. This section will describe some of the basics about magnetic fields and magnetic forces.

1.1.1 Magnetic Dipoles

Magnetic fields can be found in permanent magnets or they can be generated using current traveling in a coil. The most basic way to represent magnetic fields is through the use of a

point dipole, which produces a field at a point (x, y, z) away from the magnet described by

$$\boldsymbol{B} = \frac{\mu_0 m}{4\pi r^5}\left(3xz\boldsymbol{e_x} + 3yz\boldsymbol{e_y} + \left(3z^2 - r^2\right)\boldsymbol{e_z}\right) \tag{1.1}$$

where $\boldsymbol{B}$ is the magnetic flux density, r is the distance to the point, and μ_0 is the permeability of free space ($4\pi{\cdot}10^{-7}$). The magnetic field from a point dipole is often a good way to describe magnetic fields for magnets that are much smaller than the distance away from the magnet. In general the $\frac{1}{r^3}$ relationship is important to understanding how magnetic fields dissipate from the origin of the field. As one can expect, this can become a limiting factor when either attempting to apply forces to objects containing magnetic material or when measuring the field generated by small magnets.

1.1.2 Permeability and Susceptibility

The ability of a material to become magnetized or create a magnetic field is known as the permeability, μ. In air, the permeability is a constant, known as the permeability of free space, $\mu_0 = 4\pi{\cdot}10^{-7}$. Often, the parameter used is the relative permeability, μ_r defined by the relationship $\mu_r = \frac{\mu}{\mu_0}$. The susceptibility, χ is related the permeability by the relationship $\chi = \mu_r - 1$. The permeability of a material determines how much magnetic field can be induced into a material. Similarly, the susceptibility determines how the material will be magnetized. There are three main parameters to keep constant when discussing magnetic fields, and these are the field, $\boldsymbol{H}$, the induction, $\boldsymbol{B}$, and the magnetization, $\boldsymbol{M}$. The permeability is defined by $\mu = \frac{B}{H}$, and the susceptibility is $\chi = \frac{M}{H}$ [61]. Furthermore, each material will have some level of saturation magnetization, and remnant magnetization that determine how it can behave in a magnetic field. The ability to demagnetize the material is known as the coercive force, H_C. The permeability, saturation magnetization, and remnant magnetization of a material will affect choices as to what material to use a device that uses magnetic fields. Some common materials are displayed in Table 1.1. As one can see, iron can be a good choice for materials that is relatively cheap, easy to handle, and can be integrated into a variety of devices. Iron and nickel particles are both readily available in diameters on the

Table 1.1: Magnetic properties of some common materials [18, 61]

Material	$M_{Sat} \cdot 10^6$ (Am^{-1})	H_C (Am^{-1})	μ_r
Iron	1.71	80	5000
Cobalt	1.42	795	250
Nickel	0.48	55	600

order of a few micrometers, and iron and nickel nanowires are both easy to fabricate in most laboratories [16, 13]. Permanent magnets are typically made out of rare earth materials with a composition of Nd-Fe-B [24], as they have remnant magnetizations on orders much larger than iron.

1.2 Magnetic Nanowires and Particles

When building microdevices, the geometry and goals of the device will determine if the developer uses magnetic nanowires or particles. Magnetic particles are typically readily available from a variety of producers, while smaller particles and nanowires must be made in the laboratory [142, 39].

1.2.1 Magnetic nanowires

Magnetic nanowires have been developed for a variety of purposes, and using a large number of materials. One of the most prevalent methods for manufacturing magnetic nanowires is through the use of electrodeposition in templates [16, 63, 66, 13]. There are also other methods for depositing nanowires, such as electroless deposition [64, 110], and several others [136]. Different fabrication methods and techniques can alter the crystal structure of the magnetic nanowires, which can then alter the properties of the materials. For basic metals, such as nickel, primitive methods may be used to produce adequate results for most applications [13].

Magnetic nanowires offer a distinct advantage for actuation and sensing applications as

they can be embedded remotely into biocompatible materials. There is no need to run wires through a material or invasively provide actuation from an external tweezer. This advantage is ideal for biological applications where it may be challenging to physically manipulate cells, or the introduction of foreign objects may produce unexpected results. Some of the devices and applications for actuation of devices made out of nanowires and particles include nanowires embedded into polymeric posts for manipulation of cells [113], assembly of cells using wires [119], and sensors for measuring the microrheology of biological substances [20].

Additionally, magnetic nanowires may be used as sensors when placed close enough to a magnetic sensor. Typically, large numbers of wires must move in aggregate in order to produce enough field to affect remote sensors, although some studies have shown the ability to magnetically sense single nanowires or nanoparticles [21, 82]. Other sensors have made use of bulk motions of nanowires for use in sensing acoustics or flows [55, 80]. These sensors make use of a rotating magnetic dipole, which has a field given by 1.1, and rotates the direction of $\boldsymbol{B}$, thus changing the magnetic field observed at the sensor. Magnetic nanowires produce magnetic field changes on the order of nanotesla, which are much smaller than the magnetic fields observed due to the Earth's magnetic poles, so significant engineering is required for the sensors to function properly.

1.2.2 Magnetic Particles

Magnetic nanowires are a useful tool for many applications, but, as discussed above, they typically require small batch fabrication in a laboratory. There are few suppliers of nanowires, and it can be burdensome to purchase or make enough for large scale applications. An alternative to wires are particles on the order of nanometers to several micrometers in diameter. Magnetic particles have been used in slightly larger structures to perform sensing or actuation.

One common example of magnetic particles is to create artificial cilia by creating composites of magnetic particles and a soft polymer [80, 126, 9].These devices incorporate magnetic particles into thin strips of PDMS or another soft polymer to produce either sensors or ac-

tuators for a variety of purposes. Typically, iron particles are used as they are capable of reaching a high level of magnetization before saturating, Table 1.1.

Additionally, custom magnetic particles are often used for a variety of biomedical purposes. Some applications include imaging, drug delivery, and magnetic separation [47, 111]. Typically, manufacturing of custom magnetic particles involves reactions under pressure and a variety of chemical synthesis methods depending on the tolerance, size, and material [74, 75].

1.3 Magnetic Sensing

In addition to using magnetic microdevices for actuating forces, there are also a wide variety of devices that measure stray magnetic fields to determine the location or count of particles or wires. Magnetic sensors used in these devices are either commercially available, or custom fabricated in clean rooms, and they can use a variety of sensing techniques.

1.3.1 Giant Magnetoresistance

One of the great challenges of creating devices for magnetic sensing is the challenge posed by turning a magnetic field change into a measurable voltage change. Several devices have been created over the years, and one of the largest breakthroughs for magnetic sensing was the discovery of giant magnetoresistance (GMR) [7, 39]. The giant magnetoresistive effect is found in layers of magnetic and anti-magnetic metals. Change in magnetism affects the spin coupling of the electrons and causes a change in the resistance of the material. The giant magnetoresistance effect has been used in computer hard disk drive read heads to reduce the area and read time of the drive [92]. The discoverers of the GMR effect won the nobel prize for their discovery and advancement in the field.

Further developments of GMR effects have led to resistance changes of 15% through the use of devices known as spin valves [42]. Spin valves also use the GMR effect; however, they have a precise array of materials in order to achieve higher resistance changes. The spin valve is characterized by a "pinned" layer of magnetic material, and a "free" layer of magnetic

material with a non-magnetic conductive layer in between. The non-magnetic conductive layer is often Cu, while the sandwiching layers are CoFe. The pinning material is an anti-magnetic layer, often MnIr, and the free layer is coupled to NiFe, Figure 1.1. The base and

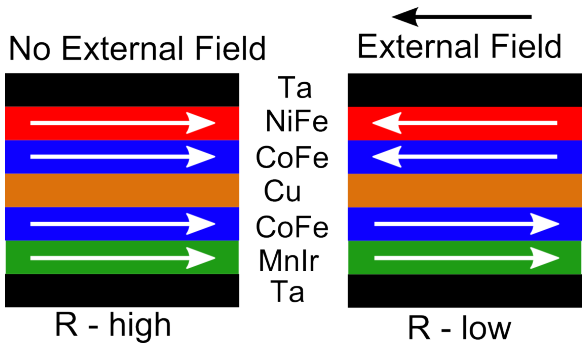

Figure 1.1: GMR devices work by altering the resistance of a thin layer of copper sandwiched in between a magnetically active layer and a magnetically pinned layer.

cap of the structure sets the crystal and is often Ta. This structure is used in a variety of devices, and has strong magnetoresistance. One of the drawbacks of devices that use GMR is that the saturation magnetism is often very small. Devices using GMR have to be used in a narrow range in order to be sensitive to the devices. Alternatively, GMR devices are often high-frequency devices that can be filtered to remove the inherent drift due to magnetic noise found throughout devices, the Earth, and local gradients [38].

1.3.2 Magnetic Devices

Several devices have been built that incorporate magnetic nanowires, magnetic beads, or larger permanent magnets. As described above, one major area of work for magnetic devices is to pull on biological materials from a distance to measure material properties, such as stiffness, or to actuate forces. I will describe a few devices here, and some are shown in Figure 1.2. One of the earliest applications to pull on cells was a seminal work performed by Bausch, et al. [10] that used magnetic beads adhered to a cell's surface to measure the

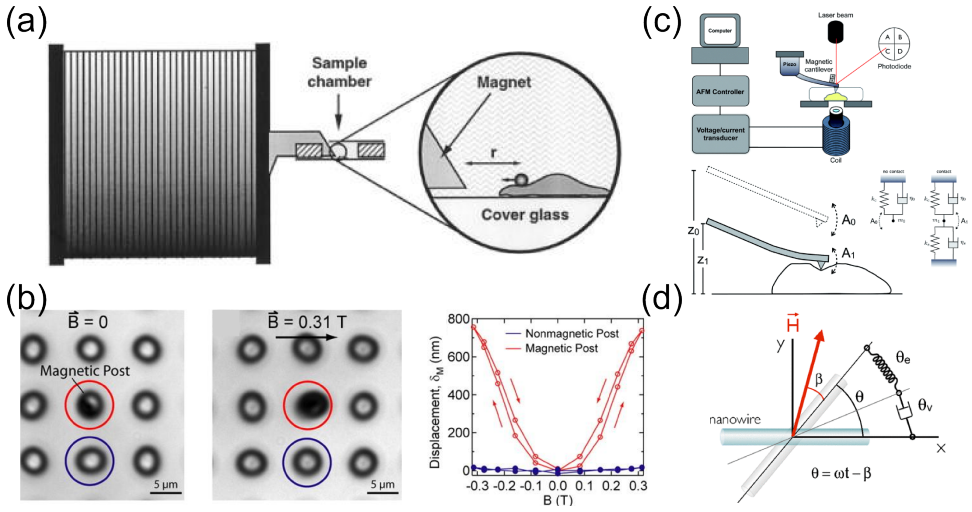

Figure 1.2: Many magnetic devices have been developed to study biological materials. (a) Bausch, et al. [11] used magnetic beads, (b) Sniadecki, et al. [113] used nanowires embedded into microposts, (c) Rebelo, et al. [93] used a magnetically active AFM tip, and (d) Chevry, et al. [20] used individual nanowires for microrheology.

viscoelastic properties of cells. Actuation was performed using an electromagnet, and the author's were able to model the cell at different locations based on how the bead returned to a neutral position. Beads were coated to adhere to the cell's surface. More recently, magnetic nanowires were embedded into microposts by Sniadecki, et al. [113] to pull on individual cells to measure how an external force would affect the rest of the tugging forces of the cells. Posts were actuated, and the force generated at a distance was measured through the use of microposts. Rebelo, et al. [93] attached magnets to an atomic force microscope (AFM) tip in order to have stronger control over the position of the tip for performing microrheology experiments across the surface of cells. There are many methods for using beads as a tool for microrheology, but Chevry, et al. [20] used the rotation of magnetic nanowires to describe the microrheology of materials.

Magnetic nanowires and magnetic beads offer great platforms for a wide variety of tools for studying biomaterials on the microscale level. Devices with magnetic nanowires and

beads can be used to either produce force, or measure some aspect of the system in question. The purpose of this thesis is to propose new devices made out of magnetic materials and to demonstrate their use to investigate questions about the nature of biological materials and test hypotheses about viscoelasticity and force production of several systems.

Chapter 2

AIM 1: FABRICATE AND CHARACTERIZE A MICROFLUIDIC DEVICE TO MEASURE VISCOELASTICITY

The first aim of my thesis is to fabricate and characterize a device for measuring viscoelasticity. The goal of this aim is to gain an understanding of how a large-scale version will work in viscous and viscoelastic fluids so that knowledge can be used on a micro-scale device. The secondary goal of this aim is to create a novel disposable system to study viscoelastic fluids with small volumes, novel configurations, and new tools.

2.1 Basics of Rheology and Microrheology

Rheology is the study of the mechanics of fluids and gels that seeks to understand the time-dependent nature of the materials. In order to study the rheology of fluids, a fluid is sheared by moving two components of the system in relation to each other. One example of this is a cone and plate rheometer that rotates a cone to shear a fluid [77]. This rheological tool uses the geometry of the cone and plate to determine the shear forces acting on the fluid. The frequency of the cone is varied, and that results in a frequency-dependent understanding of the viscoelastic properties of the fluid undergoing study. This tool performs measurements on bulk fluid and has been used to reveal information about the dynamics of fluids since its creation. There are several manufacturers of cone and plate rheometers, and it is one of the standards for measuring viscoelasticity of fluids. Although the cone and plate rheometer is the workhorse of rheology, several tools have been developed to study fluids in novel ways and on a microscale level.

2.1.1 Microrheology

Microrheology can be divided into passive and force-driven rheology techniques [128]. Passive techniques involve tracking micro-scale objects, such as microbeads as they are moved around the cell [122]. Force-driven techniques apply external forces to a particle and measure the response. The particles are often driven by magnetic forces, and have involved rotating magnetic wires[20], moving magnetic beads [10], or pulling on a magnet attached to an atomic force microscope (AFM) [93]. One popular method of studying local viscoelastic properties of fluids is through the use of magnetic beads [127]. This technique has been used extensively to study the motion of cells, and has provided a greater insight to the local mechanics of regions of the cell wall. One feature all of the techniques have in common is how the technique is analyzed to generate data about the system.

In order to determine the properties of the fluid, one must understand the characteristic equations of the system in question. For magnetic beads moving through a fluid, the drag on the bead is well understood, and any changes from the expected drag must be explained with the mechanics of the system. Similarly, equations were developed for understanding the motion of nanowires and AFM tips through a fluid. After understanding the expected transfer function, an understanding of the expected reaction of the system must also be identified and fit to the results.

There are a variety of methods to explain the mechanics of fluids, and I will describe three of the methods in this paper. They are the most common systems and explain the vast majority of systems. The three systems in question are known as a Maxwell system, a Kelvin-Voigt system, and a Zener system (also known as a standard linear model) [71]. The easiest way to understand these three systems is through the use of complementary spring and dashpot systems.

2.1.2 Maxwell Model

A Maxwell system is the most basic system and can be modeled as a spring in series with a damping element. The spring determines the storage modulus, and the damping element describes the viscosity of the fluid, as seen in Figure 2.1. The Maxwell model responds to an applied step stress with a rapid change in strain due to the modulus of the fluid and a continued creep over time due to the viscosity of the fluid, Figure 2.1.

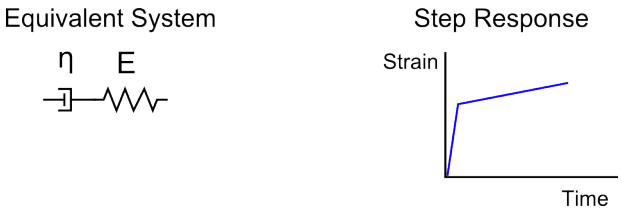

Figure 2.1: Maxwell model of a system is modeled by a spring and damper system

2.1.3 Kelvin-Voigt Model

Another simplified model for describing the behavior of a viscoelastic fluid is the Kelvin-Voigt model. It is similar to the Maxwell model; however, it uses a spring and damping element in parallel. This model describes the system as having a slower time to react due to an applied step stress, but the material eventually approaches the strain predicted by the Young's modulus, Figure 2.2.

2.1.4 Zener Model (Standard Linear Solid)

The final basic model for viscoelastic fluids is the Zener model. The Zener model is also known as the standard linear solid, and it can be extended to describe the highly dynamic behavior of some materials. The model consists of a spring and damper element in series, and that system is in parallel with another spring, Figure 2.3. The response of the system is a quick elastic response, followed by a secondary regime that has a slower elastic response,

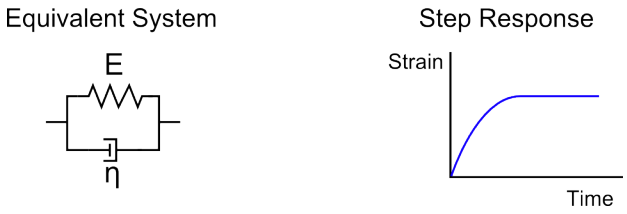

Figure 2.2: Kelvin-Voigt model of a viscoelastic system is equivalent to spring and damper in parallel.

and then a hold that approaches the final equivalent stiffness. The Zener system is a popular

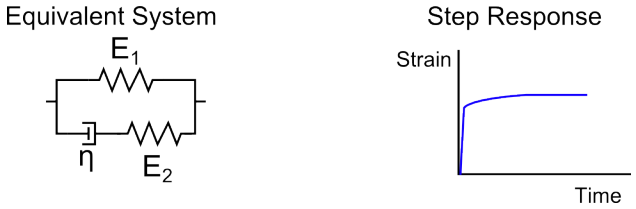

Figure 2.3: Zener model of a viscoelastic system is equivalent to a system of two springs and a damping element.

tool for a wide variety of viscoelastic materials. In particular, modifications of the Zener model have been used to model biological systems, such as the viscoelasticity of cell surfaces [10].

2.1.5 Future Devices

Although there are a variety of tools and studies that have been performed on viscoelastic materials, there is still a need for more devices that can be used for fluids that are corrosive, and for devices tailored to specific *in situ* applications. Although magnetic beads are a useful tool for studying the rheology of a large number of substances and devices, they introduce foreign objects into cells that could potentially affect the response of the cell. Using new tools to eliminate this can be useful.

2.2 Device Overview

The novel tool I developed for measuring viscoelasticity is a polymer post embedded with magnetic microparticles that is oscillated in a fluid using an externally-applied magnetic field, Figure 2.4. The first iteration of the device is controlled using an electromagnet, and the

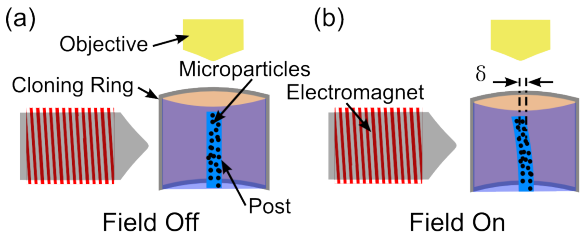

Figure 2.4: Overview of the post with the magnetic field (a) off and (b) on. A PDMS post with embedded magnetic particles is adhered to the bottom of a well and deflects under the presence of a magnetic field. The deflection of the top of the post, δ, is measured with an optical microscope. ©2016 IEEE

motion of the post is observed using an optical microscopic. The motion was characterized using mixtures of glycerol and water to vary viscosity, and collagen gels as viscoelastic fluids. This chapter will discuss an overview of the initial device and characterization ©2016 IEEE [15].

2.3 Fabrication Overview

In order to fabricate this device, a mold was fabricated at the Physics Machine Shop at the University of Washington. The mold is made out of aluminum, and through holes were used to aid in creating posts that were the entire height. The holes were 250 μm in diameter and 3.8 mm in length. Through holes were used to prevent bubbles and not fully formed posts. Previous efforts by the author showed complications in creating posts without through holes.

The mold was used to create posts out of PDMS (Dow Corning, Sylgard 184) mixed with iron microparticles (Sigma-Aldrich, 44890). PDMS was mixed in a 10:1 ratio of base

to crosslinker, as per standard instructions. The composite used in the posts was made from a ratio of 2:1 PDMS to iron particles by weight, which is equivalent to 6% volume of iron particles. PDMS and iron particles were mixed for at least five minutes, and then degassed until there were no visible bubbles. The mixture was then pushed through the mold, Figure 2.5, and excess PDMS was removed. A small amount of PDMS was used to

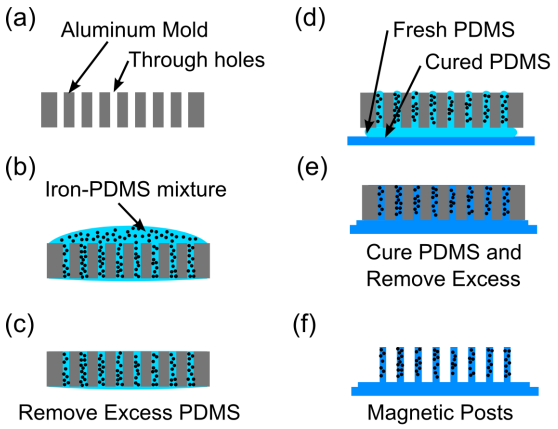

Figure 2.5: Fabrication process for embedding particles in a microdevice. (a) Aluminum molds with through-holes are (b) filled with magnetically-doped PDMS. (c) Excess doped PDMS is removed, and (d) non-doped PDMS is used to affix it to a backing layer. (e) Posts are cured, and (f) the final posts are made with a length of 3.8 mm and diameter of 250 μm. ©2016 IEEE

help affix the post layer to the a pre-cured PDMS base, Figure 2.5(d). The purpose for using a pre-cured PDMS layer was to keep the base of the post transparent, and to prevent the whole tissue culture dish from moving when a magnetic field was applied. The posts were cured for 20 minutes at 110 °C. Any small amount of excess PDMS that was pushed out of the tops of the posts during step (d) was removed, and posts were separated from each other. After that, posts were affixed to P-35 petri dishes with another small amount of PDMS, and placed withing a cloning ring (Fisher, 14-512-79). Finally, the dish was placed within a custom-fabricated holder to hold the electromagnet and post in place under the microscope, Figure 2.6

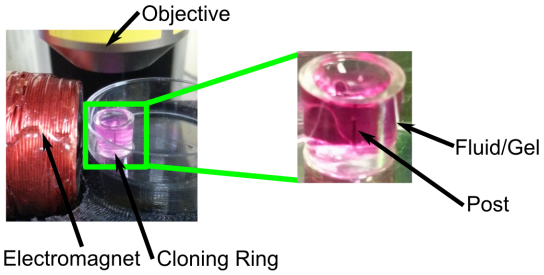

Figure 2.6: Picture of the post filled with collagen gel under the microscope. A custom holder was manufactured to hold a petri dish and electromagnet in place. The entire structure was positioned on a microscope stage. Gels and fluids are contained in a cloning ring affixed to the petri dish. ©2016 IEEE

2.4 Theoretical Characterization

Initial characterization of the motion of the post through viscoelastic fluids was performed using a custom electromagnet. Future experiments could make use of an oscillating permanent magnet in order to make use of stronger magnetic fields without the need for large currents.

The custom magnetic coil produced maximum fields of 25 mT at the location of the magnetic post, as measured with a Hall effect probe (Lakeshore, 7300). The magnetic field varied 10% over the length of the post. In order to simplify the analysis, the force on the post was assumed to be sufficiently uniform for beam equations. The force on the post is determined by the magnetic field, which is determined by the current in the system and the magnetization of the particles, which is given by

$$F = BMV = (\mu_0 i)\,(\mu i)\,V \tag{2.1}$$

where F is the force on the post due to the magnetic field, B is the magnetic field generated by the coil, M is the induced magnetism of the iron particles, V is the volume of magnetic material in the post, μ_0 is the permeability of free space, μ is the permeability of iron, and i is the current in the coil [61]. This shows that the force is dependent on the square of the

current.

The system was assumed to be a first order system, due to the relatively slow speeds of the post and the small mass in the system. This resulted in a relationship between the force on the post and the displacement of the top of the post given by

$$F(t) = (k_p + k_f)\,\delta(t) + (b_f)\,\dot{\delta}(t) \tag{2.2}$$

where $F(t)$ is the total distributed load on the post, $\delta(t)$ is the deflection of the top of the post, k_f is an experimentally determined coefficient relating to the elasticity of the fluid, and b_f is an experimentally determined coefficient relating to the damping in the system.

The system described in Equation 2.2 can be viewed in light of the free body diagram in Figure 2.7. The forces on the post are due to the magnetic force, the restoring force of the

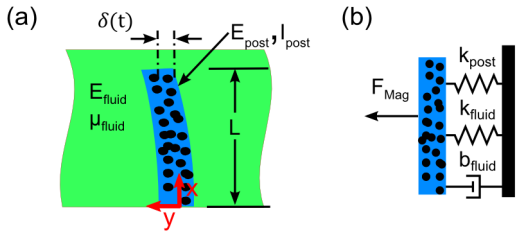

Figure 2.7: (a) Interactions of the post with the fluid or gel result in a (b) free body diagram of the relevant parameters from a first order approximation of the system. ©2016 IEEE

post as a cantilever, and the resistance on the post due to the fluid. The magnetic force is assumed to be sufficiently uniform throughout the post, and cross-sectional views confirmed a consistent distribution of particles throughout the post. In the system, the resistance of the fluid can be due to the viscosity of the fluid, or the viscoelasticity of the gels. The position of the top of the post is tracked with a camera (Hammamatsu, C11440-10C), and the following sections will describe the relationship between the motion of the top of the post and the viscoelastic properties of the post-fluid system.

2.4.1 Drag Forces

The drag forces on the post as it moves through a fluid can either be due to the viscosity of viscous fluids or due to the viscous component of a viscoelastic gel. In either case, the motion of the post is well into the laminar flow regime, based on a peak Reynold's number of much less than one. The Reynold's number, Re, indicates the relationship between viscous forces and inertial forces, so when it is much less than one, viscous forces dominate the system.

One famous use of highly viscous flows around objects is the flow around a sphere, which is used when determining how magnetic beads move through liquids at low velocities [10]. Similarly, there is approximation for the highly viscous flows around a cylinder, and it is the Oseen approximation [49] given by

$$\frac{F_{drag}}{L} = \frac{4\pi\mu}{\frac{1}{2} - \gamma - \ln\frac{Re}{4}} \frac{\partial y(t)}{\partial t} \tag{2.3}$$

where L is the length of the cylinder, μ is the viscosity of the fluid, $\frac{\partial y(t)}{\partial t}$ is the velocity of the cylinder, γ is Euler's constant, and Re is the Reynold's number. From the frame of reference of the post, the fluid is moving around the post, although the post is not strictly a cylinder in this case, and there needs to be a relationship for the post as a cantilevered beam.

A cantilevered beam will not have a constant velocity along the post; however, each segment of the post can be treated as a cylinder and integrated over the length of the post. Integrating over the length of the post gives an integral of

$$F_{drag} = \int_0^L \frac{4\pi\mu}{\frac{1}{2} - \gamma - \ln\left(\frac{Re}{4}\right)} \frac{\partial y\left(x,t\right)}{\partial t} dx \tag{2.4}$$

where L is the the length of the post. The Reynold's number and viscosity can be approximated as constants with respect to x, so the only parameter dependent on x is the velocity of the fluid, $\frac{\partial y(t)}{\partial t}$, which gives

$$F_{drag} = \frac{4\pi\mu}{\frac{1}{2} - \gamma - \ln\left(\frac{Re}{4}\right)} \int_0^L \frac{\partial y\left(x,t\right)}{\partial t} dx. \tag{2.5}$$

In order to solve the integral in Equation 2.5, I will assume that the elastic forces of the post and the post-gel interactions dominate the determination of the shape of the post. Due to

the small velocities in the system, this is an appropriate approximation, and results in the shape of a post being determined by that of a cantilevered beam with a uniform load. After this assumption, the deflection of any point on the post can be determined by the deflection of the top of the post by

$$y(x,t) = \delta(t)\,\frac{x^4 - 4x^3L + 6x^2L^2}{3L^4} \tag{2.6}$$

where $\delta(t)$ is the deflection of the top of the post, and x is a position along the length of the post.

After combining Equation 2.4 with Equation 2.6, we can determine a drag coefficient based on the first order system in Equation 2.2 given by

$$b_f = \frac{4\pi\mu}{\frac{1}{2} - \gamma - \ln\left(\frac{Re}{4}\right)}\frac{6}{15}L. \tag{2.7}$$

2.4.2 Elastic Forces

As previously mentioned, the elastic forces on the post, $k_f + k_p$ are due to both the restoring force of the cantilevered PDMS beam and to the elasticity of a viscoelastic fluid. Based on the geometry of the system, we can approximate the spring constant based on a model system of a cantilevered beam with a uniformly distributed load supported on a Winkler foundation [56], where the gel in the well is the Winkler foundation material, Figure 2.8. The

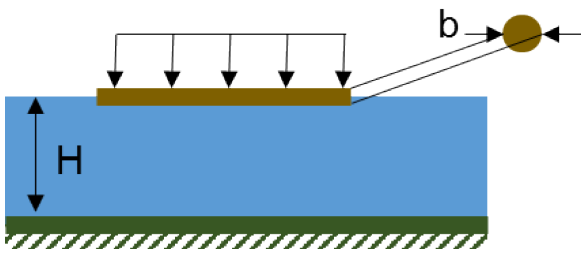

Figure 2.8: Winkler foundations are used to model civil engineering structures. The Young's modulus, E of a material can be determined after calculating the foundation modulus, k of a material with the dimensions of the beam and distance to the foundation.

Winkler foundation is an infinite elastic half-space that is commonly used to model loads on foundations in engineered structures. There are exact solutions to numerous interactions between loading configurations and Winkler foundations. In particular, there is a solution for an elastic beam that has a uniformly distributed load given by

$$k_f + k_p = kL\left(1 - \frac{2\cosh(\lambda L)\cos(\lambda L)}{\cosh^2(\lambda L) + \cos^2(\lambda L)}\right) \tag{2.8}$$

where λ is given by $\lambda = (E_p/4kI)^{1/4}$, E_p is the Young's modulus of the PDMS post, k is the foundation modulus of the gel in the system, and I is the second moment of area of the post cross-section.

The foundation modulus, k can be related to the Young's modulus of the gel, E_f, by assuming that the PDMS beam is relatively stiff compared with the gel, and that the gel interacts with a much stiffer base [22, 69]

$$E_f = \frac{(1+\nu_f)(1-2\nu_f)}{(1-\nu_f)}\frac{H}{b}k \tag{2.9}$$

where ν_f is the Poisson's ratio of the gel, H is the depth of the gel, and b is the width of the beam. For many biological gels, the Poisson's ratio must be assumed or determined from literature. Often, including for collagen, there are several reported values, but a value of 0.25 is sufficient for many applications [67]. Slight variations in the Poisson's ratio will affect results of the final stiffness calculations; however, the results will still be within the same order of magnitude. In this system, the modulus of PDMS and polystyrene are typically several orders of magnitude greater than the modulus of the gels, so the assumption in Equation 2.9 is appropriate.

In this system, if the fluid in the ring is purely viscous, the portion of the spring constant due to the fluid will approach zero, and the material will behave as a Timoshenko beam [12]

$$EI\frac{\partial^4 y(x,t)}{\partial x^4} + m\frac{\partial^2 y(x,t)}{\partial t^2} = p(x,t) \tag{2.10}$$

where $y(x,t)$ is the total deflection of any point on the post, and it is determined based on the specific mass of the post, m the Young's modulus, E, the second moment of area, I,

and the external loading on the post, $p(x,t)$. As mentioned above, I have chosen to assume that the magnetic forces on the beam are uniformly distributed accross the length of the post, and that the forces due to the mass of the beam are much smaller than those due to the elasticity of the beam. These two assumptions lead to the use of Castigliano's method [54] to solve Equation 2.10. Castigliano's method relates the displacement of each point on the elastic structure to the strain energy in the structure. For a cantilevered beam with a circular cross-section, and a uniformly distributed load the solution is

$$k_p = \frac{E_p \pi d^4}{8L^3} \tag{2.11}$$

where d is the diameter of the post, and L is the height of the post. This result is obtained as the modulus of the fluid, E_f in Equation 2.8, approaches zero.

2.4.3 Governing Equation and Material Properties

As previously discussed, I have assumed that the post-gel system is a first-order system, described by Equation 2.2. The constants in Equation 2.2 are determined by the elastic forces, Equation 2.8, and the viscous forces, Equation 2.7. Combining the equations results in a relationship between the applied magnetic force and the known and unknown parameters of the system described by

$$F_{mag}(t) = kL\left(1 - \frac{2\cosh(\lambda L)\cos(\lambda L)}{\cosh^2(\lambda L) + \cos^2(\lambda L)}\right)\delta(t) + \left(\frac{4\pi\mu}{\frac{1}{2} - \gamma - \ln\left(\frac{Re}{4}\right)}\right)\frac{6}{15}L\dot{\delta}(t). \tag{2.12}$$

There is a direct relationship between the experimentally determined damping coefficient, b_f, and the viscosity, μ, and it is given by

$$\frac{b_f}{\mu} = \frac{4\pi}{\frac{1}{2} - \gamma - \ln\left(\frac{Re}{4}\right)}\frac{6L}{15}. \tag{2.13}$$

The relationship between the spring constant and the modulus of the gel is indirect, but it can be calculated by solving Equation 2.8 for k, and then using Equation 2.9 for E_f. These two equations can be used with model fits for a first order system to gain insight into the material properties of gels measured with this system.

2.4.4 Modulus of PDMS with Iron Particles

The choice of value for the modulus of PDMS should not be taken lightly. There are several studies that have determined values of the modulus, and found that it is dependent on a large number of factors [125, 43]. Some of the factors that affect the modulus of PDMS include the mixing ratio, baking time, baking temperature, storage time, and addition of any microparticles, and the density of mixing of microparticles. In general, the modulus of PDMS has been found to be 0.5-3.5 MPa. In order to gain an understanding of the modulus of PDMS in my experiments, I ran a tensile test of specimens of plain PDMS, and PDMS mixed with iron particles. The volume percentage of iron particles is 5.7%. I found that the tensile strength of PDMS with iron microparticles was approximately 20-30% higher than that of plain PDMS.

The posts used in my experiments were cured for 20 minutes, which results in a siffness of 1.3 MPa. Posts cured for 24 hours had a stiffness of 3.1 MPa. The posts used throughout these experiments sat for several months before use, which has been shown to increase the stiffness [43]. The exact stiffness of the PDMS posts used in these experiments is not known; however, 2.5 MPa is a typical value used for PDMS posts, and this is what I used throughout the analysis. The final results scale linearly with any errors in choice of the modulus of PDMS.

2.5 Experimental Procedures

The experiments for aim 1 are primarily directed towards characterizing the system and verifying the analysis described above. Experiments were run with mixtures of glycerol (J.T. Baker, 2136-001) and water to provide purely viscous materials. The properties of glycerol when mixed with water are a non-linearly increasing viscosity [106]. The viscosity can be controlled by the volume percentage of water in the mixture, and can be controlled up to 1.4 Pa·s. For this characterization, I made mixtures of glycerol and water with a volume ratio of 90%, 96.5%, and 100% glycerol.

2.5.1 Collagen Gel Protocols

In order to characterize the viscoelastic measurements and analysis, I observed the gelling of collagen over time and three different concentrations. I used gels with concentrations of 0.1 mg/mL, 1 mg/mL, and 3 mg/mL of collagen per standard protocols [1]. Stock rat tail collagen I with a concentration of 4.1 m/mL (BD Bioscience, 354236) was diluted to form 1 mL of gel by using 10% volume of Medium 199 (Life Technologies, 11825-015). Additionally, 1 N NaOH (Fisher, SS255-1) was added to the solution until it reached a pH of 7.1, which was indicated by a color change of the fluid from yellow to pink. Finally, water was added to the solution to make up the remaining 1 mL volume. The solution was mixed thoroughly and pipetted into the wells. There were some experiments that had gels with trapped bubbles near the post, and these were removed from analysis.

Initially, collagen gels were formed at 37 °C, but the post was observed to move around while the solution underwent gelation, Figure 2.9. Posts in a well with collagen gels formed

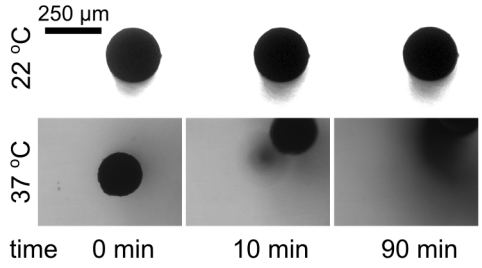

Figure 2.9: Posts moved in collagen gels formed at 37 °C often had significant motion from the neutral position, while posts formed at 22 °C remained vertical. Experiments for testing viscoelasticity of collagen gels were performed at 22 °C. ©2016 IEEE

at 37 °C moved while gelling, which may have been due to inconsistent pipetting or mixing, or non-symmetry in small bubbles in the gels in the well. At room temperature (22 °C), the posts did not move over the course of 90 minutes, while the posts at 37 °C generally moved significantly, as seen in Figure 2.9. Due to the motion of the post, gels were formed at 22 °C for the characterization experiments.

2.5.2 Data Collection Methods

Experiments for collagen gels were performed at 22 °C, and run at 0, 30, 60, and 90 minutes. The custom holder seen in Figure 2.6 was used to hold the gel and apply magnetic field at each time point. A chirp signal was used to actuate the post, and a camera (Nikon, Eclipse NV100) was used with a 10x objective to view the motion of the post. The custom magnetic coil was actuated and observed with a custom LabView program combined with a data acquisition system (National Instruments, USB-6002). At each time point, 5 second runs of actuation were performed while collecting 200 images.

Initially, posts were calibrated in viscous fluids and the force-magnetic field relationship was determined using quasi-static runs of 0.25 Hz sine waves. The amplitude of the current squared was compared with the amplitude of the post motion to determine the force generated on the post. The relationship for each post was then used in experiments with collagen gels. Data used for analysis was a chirp signal varying from 0.25 to 20 Hz.

2.5.3 Image Analysis

Images were processed using a circular Hough fitting program in Matlab [89]. The centroid movement was tracked throughout the video, and converted to displacement from the neutral position. Typical images of the top of the post, as well as the cross-sectional views of the post can be see in Figure 2.10. The Hough fitting algorithm was useful for posts contained within gels that could not easily be converted to binary images to track the centroid of the post. Additionally, this method will be generally useful for fluids and gels that are not as optically transparent.

After analyzing videos, the voltage output to the coil was converted to current based on the resistance of the coil used in the experiment. The applied force was determined based on the knowledge that the force is related to the square of the current (Equation 2.1), and the relationship determined during the quasistatic experiments. Each post was found to have slight differences in force due to magnetic fields due to changes in the final volume

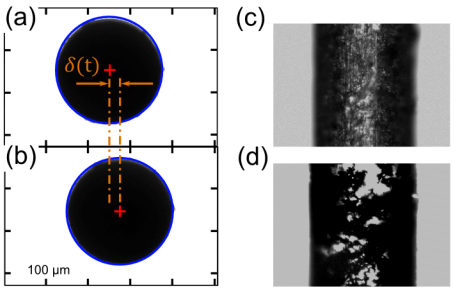

Figure 2.10: Posts moved from an (a) actuated to an (b) unactuated position when the magnetic field is removed. A circular Hough fitting algorithm is used to determine the center of the posts in each image. Side views of magnetic posts with (c) reflective and (d) bright field show the density of microparticles. ©2016 IEEE

and orientation of magnetic material in the post. Raw data of the position and input forces for different fluids can be seen in Figure 2.11 The final parameters used in the experiments were determined using the System Identification Toolbox^{TM} in Matlab. As described above, a first-order system was fit to the data from the chirp signal and used to determine the constants in the system.

2.6 Viscous Fluid Results

Viscous fluids were primarily used to characterize the system for known fluids. The viscosities of mixtures of glycerol and water were determined from published results in literature [106]. The first-order system fit was used to determine both the stiffness coefficient, and the drag coefficient as seen in Figure 2.12. As seen in Figure 2.12, the stiffness coefficient remained close to the expected spring constant determined by Equation 2.11 for all viscosities. The drag coefficient tracked well with the viscosity of the fluid in the well, which also agreed with the expected result of 0.0045 $(\text{Pa}\cdot\text{s})^{-1}$ calculated from Equation 2.13.

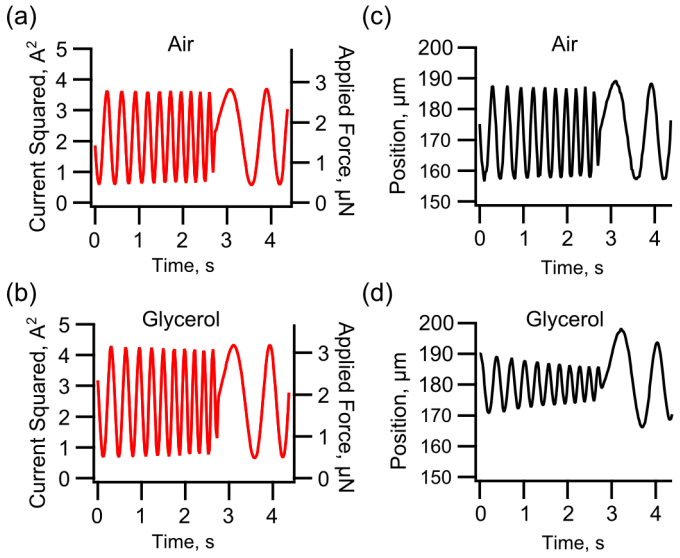

Figure 2.11: Raw data traces of the (a) applied current and force compared with the resulting (b) position of the top of the post for air. The (c) applied force was the same for glycerol, while the (d) position response was reduced. ©2016 IEEE

2.7 Viscoelastic Fluid Results

As expected, collagen gels stiffened over time, and had an increase in velocity. Furthermore, gels with higher concentrations of collagen ultimately had a high stiffness and viscosity, as seen in Figure 2.13.

Collagen gels have a much broader range of published values for the viscosity and modulus, and it is dependent on the type of collagen used, the gelling temperature, the pH of the gel, the strain rate, and the concentration of collagen. There are numerous studies on the modulus of collagen gels, including studies on the shear modulus [139], studies modeling gels to determine the Young's modulus [115, 97], and studies on mixtures of gels with cells [36] or gluteraldehyde [109]. The study with the closest methods to fabricating gels was from Roeder, et al. [97], and gave a thorough analysis of how the pH, strain rate, and collagen concentration affects the modulus. A comparison of the values determined from my

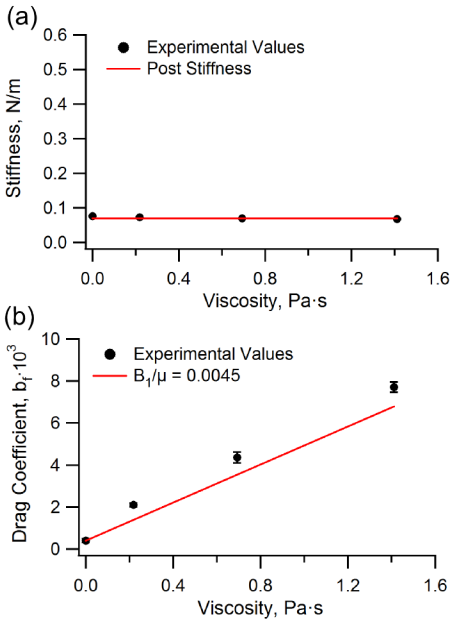

Figure 2.12: Experimental results of the post response in glycerol mixtures. The (a) stiffness is equal to the post stiffness determined by Equation 2.11, while the (b) relationship between drag and viscosity matches closely with the expected result from Equation 2.13. ©2016 IEEE

Table 2.1: Experimental values for collagen gel stiffness compared to previous work ©2016 IEEE

Concentration	Results (kPa)	Roder, et al. (kPa)
0.1 mg/mL	0.384 ± 0.2	
0.3 mg/mL		1.54 ± 0.507
1.0 mg/mL	3.792 ± 0.1	10.7 ± 1.93
3.0 mg/mL	9.360 ± 2.4	24.3 ± 4.16

experiments and values published by Roeder, et al., can be seen in Table 2.1. The values I found were generally lower than those of the Roeder study, and this may be due to a shorter

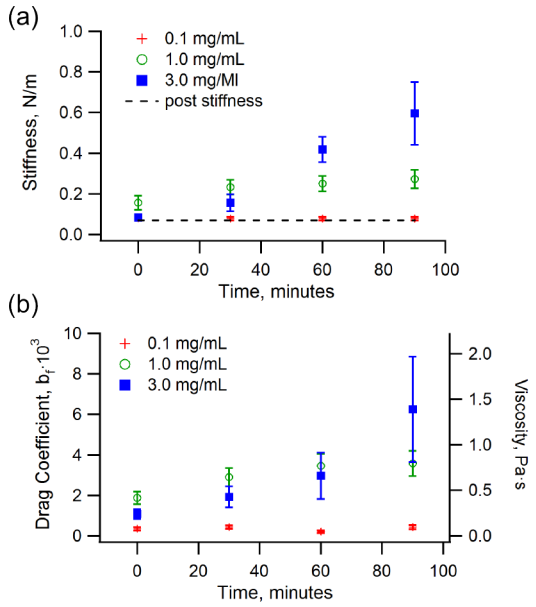

Figure 2.13: Experimental results of the post response with different concentrations of collagen gels, showing the (a) stiffness coefficient and the (b) drag coefficient determined from the first order system. Experiments were run every 30 minutes during the gel formation. ©2016 IEEE

gelation time, different gelling temperatures, or slight changes in pH. Variations in the values determined from my analysis and previously published values may also be due to some of the assumptions discussed above, although the results are in the correct order of magnitude and appear to confirm the analysis.

2.8 Discussion

This aim was to build a novel viscoelastic testing device that be used to perform *in situ* testing of fluids and gels. I have successfully built this device, described its function, and ran experiments to confirm the analysis. Collagen gels and viscous mixtures of glycerol and water were used to characterize the device. This device may be used to test fluids over time without causing destructive behavior to the fluids. The device may also find applications in biology, where continuous monitoring of cell cultures over time can give an insight into the

mechanical responses of tissues.

Some of the limitations of the device are that it can only be used in its current state for relatively weak gels and fluids. The resolution of the position of the post does not enable measurements of viscoelasticity in regimes where the elasticity of the gel is high. This may be modified by applying a higher force to the post or increasing the amount of magnetic material in each post. Additionally, gels and fluids must be optically transparent or translucent in order to use this system.

One advantage of this device over current technologies is that it only requires small volumes of material in order to produce measurements of the bulk properties. In its current configuration, samples are 200 μL, and the volume can be further reduced by changing the size of the ring used to contain the fluid. This is particularly useful for situations where reagents are expensive.

The small size and biocompatibility of the device created in this aim can be useful for future studies with live cells or tissues *in situ* [90, 41]. The entire system can be placed in an incubator for long-term culture of cells or assessing cells on a continual basis. The device may also be modified to perform parallel studies of many groups of cells that are undergoing different treatment options for rapid testing.

Chapter 3

AIM 2: MINIATURIZE THE MAGNETIC DEVICE FOR USE IN A SHEAR FLOW DEVICE TO MEASURE PLATELET VISCOELASTICITY

The second aim of my thesis is to miniaturize the microfluidic tool for use in a microfluidic channel. The goal of this aim is to determine if the stiffness of a platelet clot developed under shear flow follows the same trends as the force generated by the clot. My hypothesis is that I will be able to measure clot stiffness and that the stiffness is at least partially driven by myosin II activity.

3.1 Platelet Biology and Rheology

After a tearing of the endothelium, platelets are the first cells to enter and start the repair process of a wound site [28]. The entire repair process is known as hemostasis. The first stage of hemostasis, titled primary hemostasis [19], happens when activated platelets are attracted to a wound site and bind to the point of the wound to form a soft platelet plug. The second stage of coagulation, known as secondary hemostasis [73], involves the recruitment of fibrinogen to the site of the wound to convert it to fibrin to form a clot. The entire process has been studied extensively for over 1000 years [73], and there are still more aspects of hemostasis yet to be understood [60].

3.1.1 Primary Hemostasis

Primary hemostasis is the process by which platelets, which are always flowing with the bloodstream, become activated and adhere to a damaged portion of the endothelium [19]. This process has been studied extensively, and it involves several mechanical changes to

the system. Platelets undergo shape changes after becoming activated, and platelets begin to adhere to each other. One of the key factors involved in primary hemostasis is the effect of shear stress on the platelets and how they aggregate to form a platelet plug [85]. The two main factors involved in platelet adhesion, aggregation, and force development are glycoprotein (GP) Ib, and the integrin $\alpha_{IIb}\beta_3$ [62].

3.1.2 Secondary Hemostasis

During secondary hemostasis, short molecules known as fibrinogen are converted to longer molecules known as fibrin, and these molecules form networks to produce enough force to stop clots [83]. It is thought that one of the key factors in controlling the synthesis of fibrin is thrombin. The density and methods of activating fibrinogen to form into fibrin can control many of the mechanical properties of the clot, and how it undergoes fibrinolysis [129, 130]. In addition to the function of platelets, thrombin, and fibrinogen, there is an extensive intrinsic and extrinsic pathway containing over 13 tissue factors that control and mediate the formation and lysis of clots during hemostasis [28].

3.1.3 Testing Under Shear Flow

One of the most important aspects of clotting that has been the cause of a great number of studies is the mechanical effects of shear flow on platelets and the entire coagulation cascade [60, 40].

3.2 Platelet Functional Testing

Many tools that have been developed for macro-scale and microfluidic studies of platelet clotting forces [37]. These tools seek answers to questions about what factors affect the mechanical integrity of clots and have been used both for research purposes and clinical use. Two of the most prevalent devices are thromboelastography (TEG) and rotational thromboelastometry (ROTEM). Along with TEG and ROTEM, there are a number of studies

of the forces, clot size, clot stiffness and creep over time and under the presence of different antagonists and inhibitors to determine how platelets function to form platelet plugs, coagulation, and eventually undergo fibrinolysis throughout the wound healing process.

3.2.1 Thromboelastography

There are two primary methods for measuring shear-induced platelet forces - thromboelastography (TEG®), and rotational thromboelastometry (ROTEM®) [27]. Both TEG and ROTEM use whole blood pipetted into a small cup and measure the response of a slender pin. In TEG, the cup is rotated while blood clots and induces motion of the pin; in ROTEM, the pin is rotated, and the reduction in oscillation of the pin is measured [76]. Although the two techniques are similar, there is an ongoing debate over which is more accurate and easier to use [59, 102, 27, 30].

Some of the key insights that TEG and ROTEM can provide are the effects of fibrin and platelet-fibrin interactions on clots [129], and that these effects are clinically relevant, especially in trauma situations [130]. TEG and ROTEM have provided extensive data about the nature of clots, and the contribution of different components; however, they do not act physiologically, and suffer from a lack of ability to gather additional data points including a visualization of the clot, the effects of significant shear, and the effects of platelets without performing additional processing steps.

3.2.2 Clot Retraction

Another key device for studying platelet functions is the clot retraction assay [98]. The basic function of the device is to determine the area of platelet clots over time. As platelets pull on each other to produce more force, the overall clot area will decrease as the myosin chains pull the actin filaments closer together.

3.2.3 Shear Flow Devices

One key study of the function of platelets during clot formation is through the use of devices that can provide shear forces. These devices are able to better provide physiological conditions to understand the factors that go into hemostasis *in situ*.

Several studies used cone and plate rheometers [48, 107], and these studies vary the speed of the system to produce shear forces on platelets. This technique has provided significant insight into the effects of shear forces, but many other groups have chosen to produce flows that look more like flows throughout the body. Flows in the body are through small cylindrical blood vessels, so groups have developed similar looking devices to create shear flows [101, 6]. There are several other methods, and microfluidic methods to study the mechanics of platelets as they encounter shear forces and aid in the wound healing process.

3.2.4 Other Devices and Findings

In addition to the specialized equipment described above, several standard rheological tools and methods have been used to characterize the viscoelastic properties of clots during wound healing.

One method used to investigate the creep recovery of clots prepared under thrombin or ancrod [8]. The device used for this study was essentially a parallel-plate rheometer, and the study investigated the effects of coarse, intermediate, and fine clots prepared with different concentrations of fibrinogen, and higher concentrations of fibrinogen produced finer clots. Additionally, the authors found that creep increased with decreasing clot coarseness. One drawback of the device is that independent measurements had to be made for studying the structure of the clot and the clotting time of the clot.

Another device is similar to a cone and plate rheometer [86]. The device can be used to produce shear forces on platelets in a variety of configurations. The group did studies and was able to produce a range of waveforms on platelets in order to build a model of platelet function. Another study with the device [108] investigated how platelets would be effected

by cardiovascular devices that can produce additional shear forces than typical conditions [99].

3.3 Device Overview

Previously, a shear flow device was developed to measure the forces of platelet clots as they formed on posts [121], Figure 3.1. Whole blood flows through a microfluidic channel where it

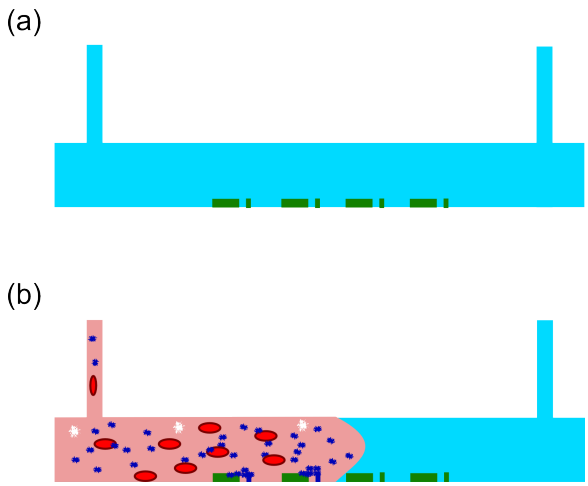

Figure 3.1: (a) A microfluidic device is built with rigid and flexible structures on the base, and the entire structure is made out of PDMS. (b) Whole blood flows through the channels, and platelets (in pink) adhere to the collagen-fuctionalized features. After some time, platelets produce force, bending the post towards the rigid block.

encounters small features designed to create shear gradients that cause platelets to activate and form platelet clots between a rigid block and a micropost. The force of the clot is determined by the motion of the tip of the micropost and can be determined by assuming that the entire clot is forming between the post and the block given by

$$F_{clot} = \frac{E\pi d^4}{8L^3}\delta \tag{3.1}$$

where F_{clot} is the force of the clot, E is the modulus of the post material, d is the diameter of the post, and L is the height of the post. Previous results have shown that the clot force

increases over time, and that different antagonists can affect the forces.

The aim of this section is to develop a new microfluidic channel system that has magnetic material embedded into the posts in order to apply forces to the platelet plugs to determine the viscoelastic properties to the clots over time. I first set out on building this device with nanowires embedded into microposts, Figure 3.2, then modified the design for larger posts to be used with nanowires. Ultimately, I found that using magnetic particles embedded in

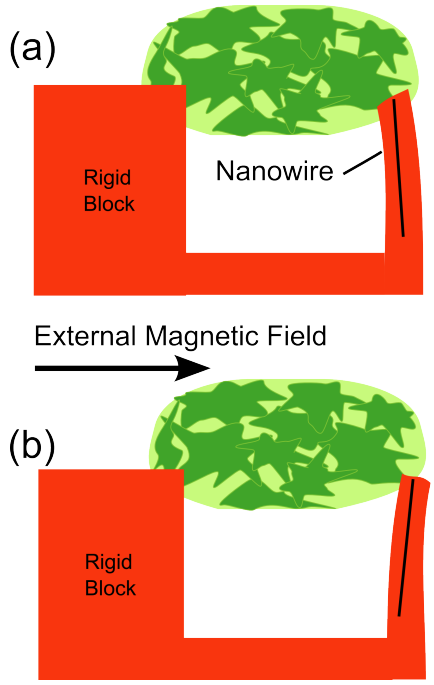

Figure 3.2: Conceptual design of testing setup. Nanowires are used to apply forces to clot formed on a microfluidic shear device.

the posts was most advantageous for providing consist deflections of posts. I will detail my attempts at manufacturing posts with embedded nanowires, then explain the final iteration of my device that used magnetic particles. As clots form on the device, an external magnetic field applies an opposing force to the clot, and the elastic properties can be determined using a similar technique to the methods described during Aim 1. The goal of this method is to determine the elastic properties of the platelet clots formed due to high shear rates.

In this section, I will detail the designs and fabrication methods of early devices, then conclude with the final design and fabrication method of the device used for experiments in this section. Early designs were built with integrated microfluidic channels and embedded nanowires. Later designs used different fabrication methods, had separate channels, and eventually moved to magnetic particles mixed in with PDMS.

3.3.1 First Designs: Integrated Channels and Nanowires

My initial device designs used integrated microchannels, and embedded nanowires. Although some of these devices showed promise for use, the fabrication was not robust enough to warrant use in a final design.

Integrated Channel Fabrication with SU-8

All of the devices built in this section make use of a double replica molding process for building the magnetic posts. Devices used in previous work by Ting, et al. [121] used microposts with a diameter of 3-6 μm and a height of 10-20 μm. In order to increase the magnitude of the force on the posts, I determined that the size of the posts needed to be increased to have a diameter of diameter of approximately 20 μm and a height of 50-100 μm. The larger post diameter and height allows for more magnet material to be embedded in each post which increases the potential force on each post. The effective stiffness of the small and large posts are close to the same so that force could still be measured with the larger posts. The posts were fabricated using a two-step soft lithography process, as detailed below.

Microposts are fabricated using soft lithography [135], Figure 3.3. Initially, a base layer of SU-8 2005 (Microchem) is spun at 3000 rpm onto a dehydrated silicon wafter to aid in adhesion to the wafer.

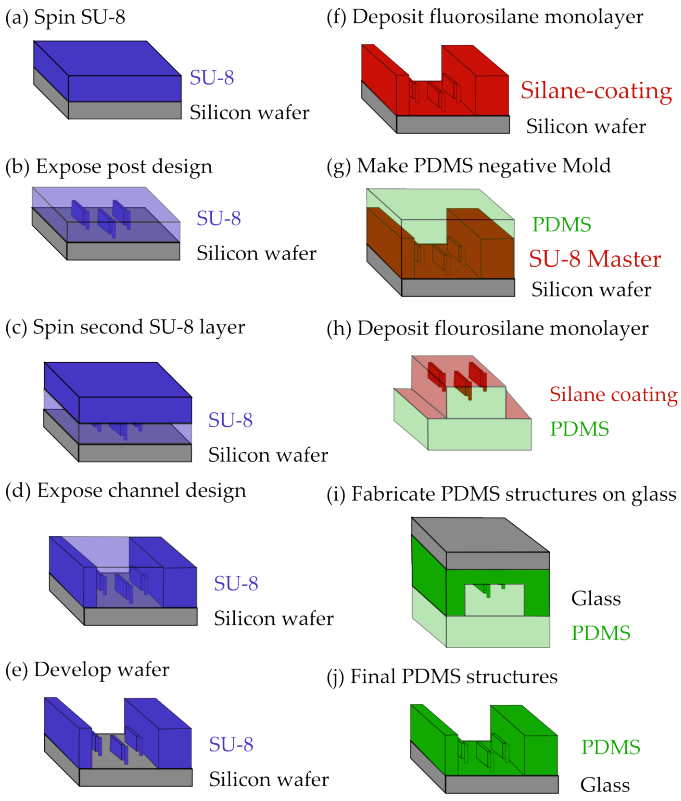

Figure 3.3: Microstructures can be fabricated using standard soft lithography techniques. First, (a) SU-8 is spun onto a wafer, then (b) exposed to UV light for the post design on the base layer. (c) Another layer of SU-8 is spun onto the wafer, and (d) exposed to a design to make channels. The wafer is (e) developed, resulting in a master that is (f) coated with fluorosilane. (g) PDMS negative molds are made, (h) coated with fluorosilane, and (i) used to manufacture the microstructures that result in (j) a final structures with blocks and post integrated into microchannels. The channels are ultimately formed by bonding a flat block of PDMS onto the top of the structure. (Figure adapted from Bielawski, et al. [14]).

The wafer is baked at 95 °C for three minutes, exposed to ultraviolet light using a contact aligner (ABM-USA, San Jose), and baked again. After a brief cooling, SU-8 2100 is spun onto the wafer at 2000 rpm for 45s to form a thick layer of SU-8. The wafer is baked at 65 °C for 10 minutes, then 95 °C for 30-40 minutes, exposed with custom patterned masks made on a MicroPG-101 (Heidelberg Instruments, Heidelberg, Germany), and baked again. At this step, the wafer can be developed to create posts, but another step of spinning SU-8 is required for manufacturing integrated channels. Another layer of SU-8 2050 is spun onto the wafer at 2000 rpm for 45s, resulting in a total thickness of 100-150 μm. After another process of baking at 65 °C for 10 minutes, then 95 °C for 30-45 minutes, the wafer is exposed to the design for the integrated channels, then baked again. Next, the wafer is developed in SU-8 Developer (Microchem, Westborough, MA) for 15 minutes, and agitated during the development. Finally, the wafer is rinsed in SU-8 Developer then IPA, and the master mold for the posts is produced, Figure 3.4. The master mold of SU-8 is hard-baked at 150 °C for at least two hours, then, after cooling, it is prepped in a plasma prep II chamber (SPI Supplies, West Chester, PA), and then placed under vacuum with a small droplet of (tridecafluoro-1,1,2,2-tetrahydrooctyl)-1-trichlorosilane (T2492-KG, United Chemical Technologies) for 12 hours. The silanized master is then used to fabricate negative molds out of PDMS by pouring PDMS over the mold and baking for ten minutes at 110 °C. Negative molds are prepped in a plasma prep chamber and placed under vacuum with a drop of silane to coat them for mold removal. Glass slides are prepped in a plasma prep chamber, then a small drop of PDMS is placed on the slides, and the negative mold is placed on top of the PDMS. After baking for 24 hours at 110 °C, the negative mold is removed, and the PDMS features are ready for experiments, Figure 3.5.

In order to make channels, a mold of PDMS with openings for inlets and outlets to a straight channel is placed on top of the structure with the features inside of the channel. The two segments of PDMS are bonded by prepping each half in a plasma prep chamber for 15 seconds under vacuum.

This initial fabrication process had several drawbacks. One of the main drawbacks was

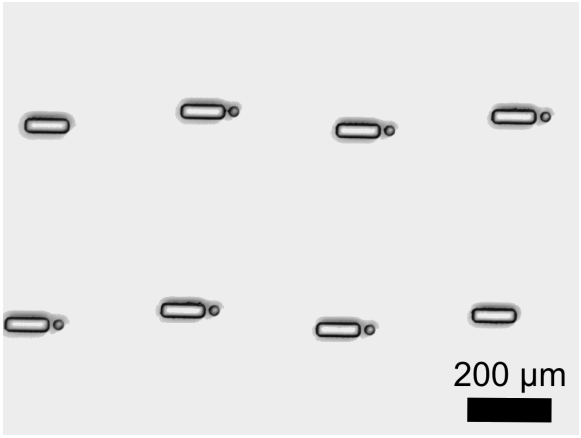

Figure 3.4: Images of the features made on a silicon wafter using SU-8 for a master mold for initial large block and post structures.

that the large surface area of cured SU-8 on the wafer caused significant stress in the film, resulting in delamination. Several structures created in the clean room ultimately failed during the final plasma treating, or initial castings, Figure 3.6. Some devices were successful in creating integrated posts and channels; however, the channels created an additional manufacturing difficulty. The deposition of magnetic material into the posts is a challenging process that is described in more detail below, and the raised channels only perpetuated the problems. The goal of using integrated channels can help aid the final fabrication and similarity of devices, but the issues with fabrication ultimately led me to investigate other fabrication options. The first step was fabricating posts that were not integrated into channels. The channels were to be fabricated separately and placed over the channels. I will describe this in detail in the final device fabrication section.

Nanowire Fabrication

The initial plan for creating magnetic actuation was to use magnetic nanowires and embed them into microposts. Magnetic nanowires have advantages over magnetic particles as they can be used in smaller posts, and can be actuated with a uniform magnetic field. Magnetic

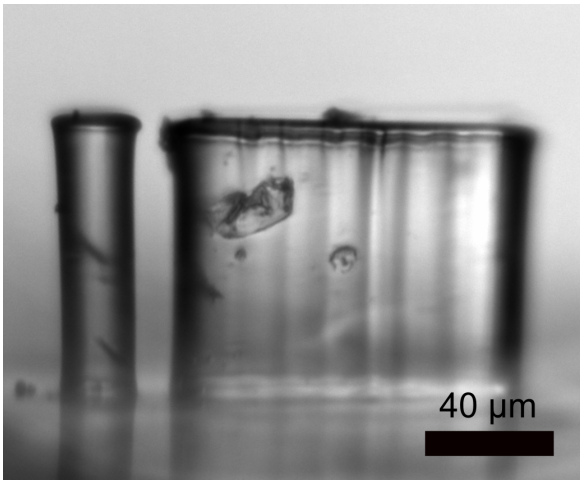

Figure 3.5: Side view of an initial design for posts and blocks fabricated using an SU-8 lithography process. Posts have diameters of 22.9 μm, and a height of 94.6μm, resulting in a stiffness of 120 nN/μm.

nanowires can be made in a variety of materials [16], and I have made nanowires out of nickel and iron. Several methods have been used to fabricate nanowires, including many that directly control the rate of deposition through the use of a potentiostat [16] using template deposition. Although a potentiostat can help control the deposition and properties of magnetic nanowires, the main requirements for creating nanowires is a template, a voltage potential, and proper metal ions in solution. Based on previous work, I created nanowires out of nickel and iron using a battery [13], Figure 3.7. In order to fabricate nanowires, an alumina oxide filter is used as a template and has pores of approximate 200 nm, and it is coated with a eutectic metal, in this case GaIn, and placed in direct contact with a copper backing. The copper plate is screwed into a custom chamber with a seal to hold the plating liquid. A plating mixture is poured into the chamber and is dependent on the desired metal. For nickel nanowires, Watt's plating solution is used, which is composed of 300 g/L of $NiSO_4 \cdot 6H_2O$, 45 g/L of H_3BO_3, and 45 g/L of $NiCl_2 \cdot 6H_2O$. Iron nanowires have several plating solutions [16, 63, 137, 50], and I successfully used a solution of 120 g/L

Figure 3.6: Thick layers of SU-8 caused significant film stress, resulting in delamination from the wafer during plasma treatment or during the hard bake step.

$FeSO_4 \cdot 7H_2O$, 45 g/L of H_3BO_3, and 3.5 g/L of Ascorbic Acid ($C_6H_8O_6$). The deposition of nanowires is started by applying the negative electrode of a AA battery to the copper plate, and the postive end to a nickel or iron wire placed into the plating solution, depending on the desired nanowire composition. Nanowires deposit at a rate of approximately 1 μm/min, and I typically let nanowires deposit for 20-40 minutes. After removing the voltage potential, the GaIn backing can be removed with 1M nitric acid. The template can then be immersed into a bath of 1M NaOH for at least one hour, or until the template has dissolved into solution. After the template is dissolved, the wires can be rinsed and suspended in ethanol for use. Finished nanowires were 200 nm in diameter and 5-20 μm in length, Figure 3.8

Posts with Nanowires Fabrication

Posts are embedded with magnetic nanowires by depositing a solution of nanowires onto the negative molds and placing a magnet underneath the mold, Figure 3.9. A small solution (about 20 μL) of nanowires suspended in ethanol is deposited onto the mold, and moved around the holes for the posts using a pipette. I tried several methods for depositing nanowires into the holes of negative molds and found that moving the solution around while the nanowires were suspended was the most effective. For molds with large arrays of microposts, I found that a maximum of 20-30% of posts were filled with nanowires regardless of

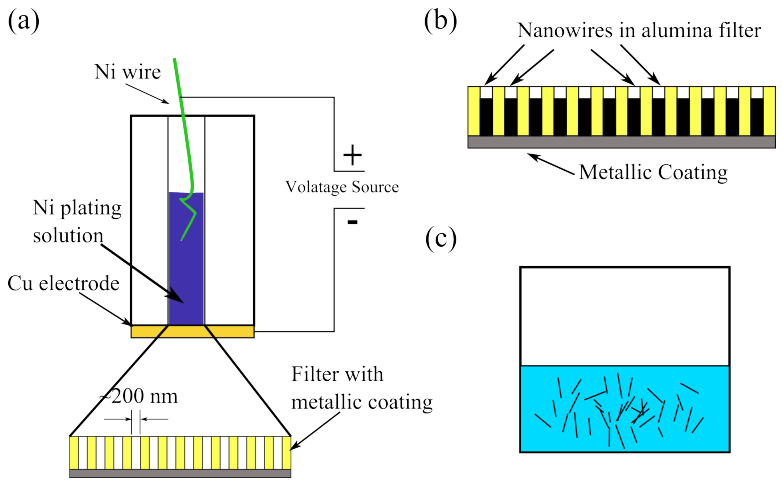

Figure 3.7: Nanowires are fabricated using deposition in templates. (a) A voltage potential is applied between a metal wire and a copper plate containing the template (inset). (b) Nanowires form inside the template, and (c) are released in solution.

the method used or the size or number of droplets used to deposit wires. Furthermore, additional methods of spinning wires into place, using a more uniform field, or coating nanowires with surfactants were not effective. In general, I found that wires did not move off of PDMS once stuck, and that the surface tension of the evaporating droplet was stronger than the magnetic force in moving the wires. Moving the wires in solution helped them to be pulled down into holes where they might stick. After depositing nanowires and allowing the drop of ethanol to fully evaporate, posts were fabricated using PDMS as described above. The nanowires fill into the posts and are fully embedded into the microposts, Figure 3.10.

Although magnetic nanowires have advantages over magnetic particles, they also typically resulted in a low number of upright posts that moved under magnetic fields. I worked extensively to improve the seeding density of magnetic nanowires into the posts, but was unsuccessful in improving the yield of magnetic posts beyond 40%, Table 3.1. My initial attempts to increase the seeding density were to simply increase the density of wires in the solution used, however the yield never moved beyond 20%. Adding more droplets of solution also did not improve the yield.

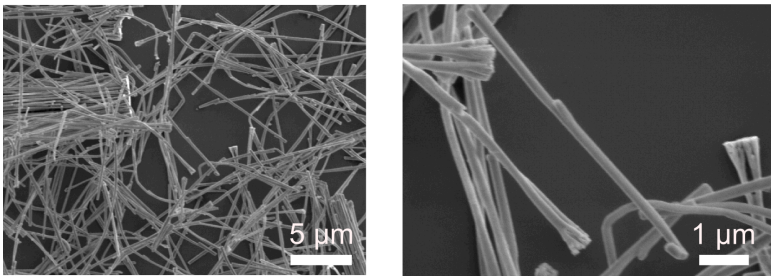

Figure 3.8: Scanning electron microscope (SEM) images of nickel nanowires fabricated using electrodeposition in templates.

Beyond merely dispersing droplets of ethanol on the molds, I also attempted many other embedding techniques. I investigated mixing nanowires into PDMS, but that resulted in a low seeding density. The wires did not appear to move through the PDMS due to the high viscosity. I attempted to centrifuge wires into the posts, but was left with a maximum of 5% yield. Some of the problem of a low yield was attributed to the alignment of the negative mold and moving it after centrifuging. I also built magnetic coils to alter the magnetic fields to be uniform or to alternative the field experienced by the wires. Neither magnetic field approach yielded more wires than using a magnet. The nanowires were typically in solutions of ethanol, and I attempted to increased the yield by immersing a negative mold into the solution of nanowires so the maximum number could hit the mold. Ultimately, this still resulted in a yield of 20%. The most promising method of embedding nanowires was to wait for the ethanol solution to dry, then move a pipette along the surface of the mold to increase the chances of a wire landing in a post. This method did increase the yield to approximately 40%, but the posts that did not have wires were typically deformed.

3.3.2 Final Design: DRIE Master with Separate DRIE Channel and Magnetic Particles

The final design that I developed to increase the number of magnetic posts and the force on the magnetic posts was to manufacture a master using deep reactive ion etching (DRIE), then create a second channel using a longer DRIE time, then manually align the channel

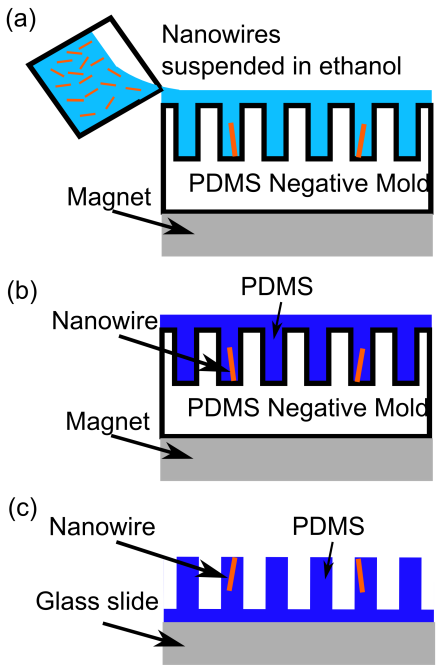

Figure 3.9: Magnetic microposts are fabricated by (a) depositing a small droplet of nanowires suspended in ethanol on a negative mold, (b) allowing the ethanol to dry, then depositing PDMS on the mold, and (c) curing the PDMS under a magnetic field to keep the nanowires in the holes until peeling.

and posts. I will detail the final fabrication procedures in this section.

Deep Reactive Ion Etching of Posts and Channels

Deep reactive ion etching (DRIE) is a microfabrication process that can be used to manufacture tall, vertical structures. DRIE alternates gases to etch (SF_6), and polymerize (C_5F_8) the surface of a silicon wafer. The result is a high aspect ratio structure made out of silicon etched into the wafer [133].

In order to create posts using a DRIE process, a patterned wafer was used with a negative resist, etched, then silanized to create a master, Figure 3.11. First, wafers were activated for resist coating with hexamethyldisilazane (HMDS) in a vacuum oven. After HMDS treatment,

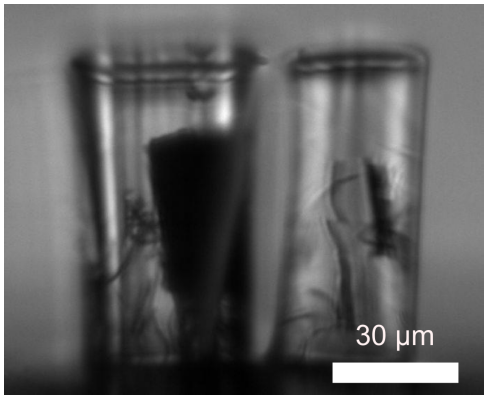

Figure 3.10: Multiple nanowires are embedded into each post, thus increasing the potential magnetic force on each micropost.

Table 3.1: Overview of nanowire fabrication methods and yields

Seeding Method	Percent of Upright Posts	Comments
Ethanol Dispersion	20	Best result
PDMS Mixing	5	Did not move through PDMS
Centrifuge	5	Alignment did not work consistently
Uniform Field	20	Same as a normal magnet
Immersion	20	Significant agglomeration of wires
Dry Embedding	40	Resulted in fewer formed posts

NR-9 (NR-9, Futurrex, Franklin, NJ) was spin-coated onto the wafer. The coating was applied for 5 s at 500 rpm, then 45 s at 4000 rpm to form a thin layer. Immediately after spin coating, the wafer was pre-exposure baked at 100 °C for 60 s. The wafer was then exposed with a mask for 15 s with the post design, then developed in RD6 (Futurrex) for 30 s. After development, the resist was baked at 100 °C for 60 s, and was ready for DRIE. DRIE

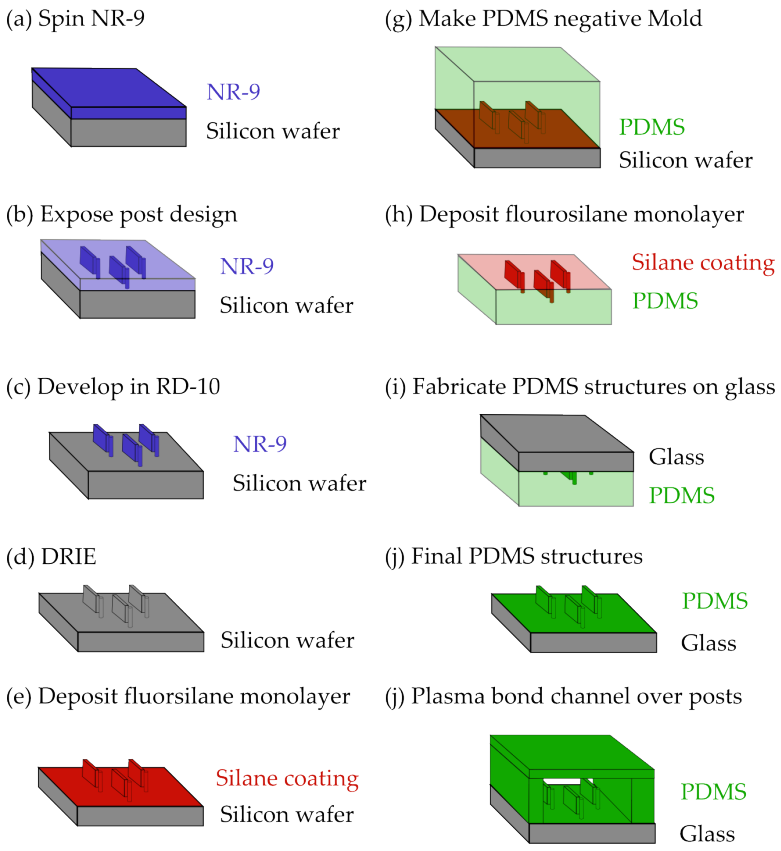

Figure 3.11: Deep reactive ion etching (DRIE) was used to create posts and channels. (a) NR-9 resist was spun onto a wafer, and (b) exposed, then (c) developed. (d) DRIE was performed for 250 cycles, and (e) the wafer was coated with silane to be used as a (g) mold. (h) Negative molds were coated with silane and used to (i,j) form magnetic post structures. Finally, channels made using steps (a-g) were placed over the magnetic PDMS structures.

was performed for 250 cycles on an inductively coupled plasma etch (Oxford Instruments, Abingdom, United Kingdom) and likely hit the limit of the aspect ratio for NR-9 on the machine. The wafer was then silanized overnight and was ready for creating negative molds of posts.

Channels were fabricated in a similar method as the posts. A wafer was spun with AZ 9620 (Merck, Darmstadt, Germany) using an initial spin of 500 rpm for 5 s, then a 45 s spin at 3000 rpm. The wafer was baked at 100 °C for 120 s. The wafer was then exposed with the channel pattern for 25 s and developed in AZ400 (Merck). The wafer did not have a hard bake before DRIE. DRIE was again used to etch the wafer with 250 cycles. The result was a wafer with raised sections representing a negative mold for the channels. The channels had a height of 115 μm.

Magnetic Post Fabrication

The master described above was used to create negative molds out of PDMS by baking 10:1 PDMS at 110 °C for 10 minutes. The negatives were silanized overnight, then were ready for fabrication. As described in Chapter 2, PDMS was mixed with iron microparticles in a 2:1 PDMS to iron ratio by weight. Four grams of PDMS mixed with two grams of iron was typically enough to make at least eight slides worth of magnetic posts. The PDMS-iron mixture was poured onto the negative mold while a magnet was placed beneath the mold. The mixture was allowed to sit for 10 minutes, then it was either scraped off with a gentle touch on a razor blade away from the magnet or scraped off with a glass slide while sitting on the magnet. The strength of the contact from the razor to the mold helped determine how full of particles the posts would be. Pushing too softly would result in significant iron in the base of the slide, causing distortion of the entire slide. Pushing too hard would result in relatively empty posts that did not create as much motion. After scraping the PDMS mixed with iron particles off the base, a small amount of PDMS was added to the negative mold, and the system was bonded to glass slides that had been prepped for 15 s in a plasma preparation chamber. The molds sat in a 110 °C oven overnight, and were peeled and trimmed of excess

PDMS. The result was posts filled with iron particles with heights of 77 μm and diameters of 19 μm, Figure 3.12.

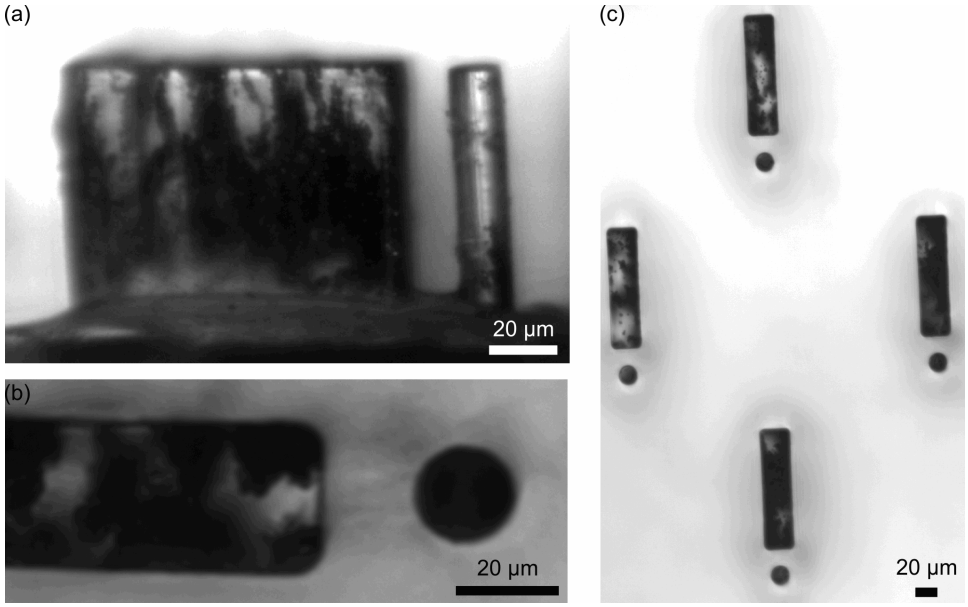

Figure 3.12: Magnetic posts were sucessfully fabricated, and (a) had a distribution of iron microparticles, (b) were vertical and able to be imaged for position, and (c) arranged offset from each other to form platelet clots.

Final Device Assembly

The last step in fabricating the devices was to assemble the channels and connect them to the magnetic substrates described above. The master silicon mold of the channels was used to create PDMS channels by pouring PDMS over the master with a thickness of 2-5 mm, and curing for 10 minutes at 110 °C. Inlet and outlet ports were then cut into the channels with a leather punch. Blocks of PDMS were used to aid in creating inlet and outlet ports. Holes were punched into flat PDMS, then tubing was placed into the holes, affixed with PDMS, then baked for 10 minutes at 110 °C. Small sections containing one tube were cut out, then affixed with PDMS to the channels. The channels and the slide containing the PDMS posts

were then treated with plasma for 15 s and bonded together to create a permanent seal. The channels were manually aligned with the post regions resulting in five channels on each glass slide, Figure 3.13. Some features were knocked down, but the channel still typically

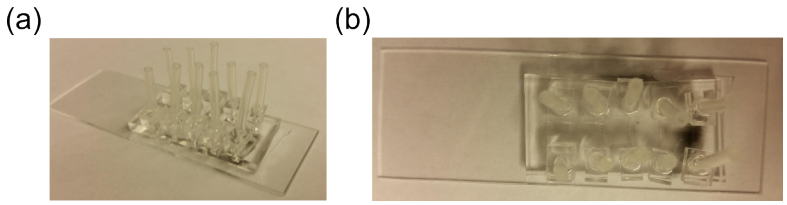

Figure 3.13: PDMS channels were manually aligned and placed on top of arrays of PDMS posts.

provided a sufficient seal. Each channel had 28-35 block structures, and 20-30 upright posts with magnetic material.

3.3.3 Applying Magnetic Forces

The final remaining challenge to pulling on clots developed by shear flow is to apply magnetic forces to the clots. In Chapter 2, I described the use of an electromagnet that produced a maximum field of 25 mT at the micropost, but with a permanent magnet, fields of well over 100 mT can easily be produced at the location of the posts. In general, I found that using a close-proximity permanent magnet produced consistent and repeatable forces to the posts, although controlling the position for dynamic measurements proved to be a challenge. In this section, I will detail my initial attempts to apply magnetic forces to the posts with external magnets in a dynamic fashion, then I will describe the final device used for studies described in this thesis.

Dynamic Permanent Magnet Force Control

My first plan to dynamically control the motion of the posts using a permanent magnet was to position a magnet to the side of the channels. I will describe my progress of this method

in detail; however, this approach could not be feasibly implemented due to the channel geometry. I was able to move posts when the slide was trimmed and the magnet was less than five millimeters from the posts, but as the distance increased, the force on the posts was drastically reduced to the point where it could not produce enough motion to track.

In order to use a permanent magnet for dynamic mechanical analysis using sine waves as the input force, I first needed to determine how the magnetic field changes with distance to the posts, as the magnetic field is not directly proportional to the position of the magnet. Fundamental theory described in Chapter 1 shows that we expect the magnetic field to decrease with the third order of the position, and the force to decrease with the forth order of the position. In reality, the permanent magnet does not act as a magnetic dipole, so the force and field vary differently as well.

I experimentally determined the field of the permanent magnet used in this experiment, and fit a curve that is defined by $B = 6 \cdot 10^{-6} x^{-2.3984}$, Figure 3.14. Iron is a material that has

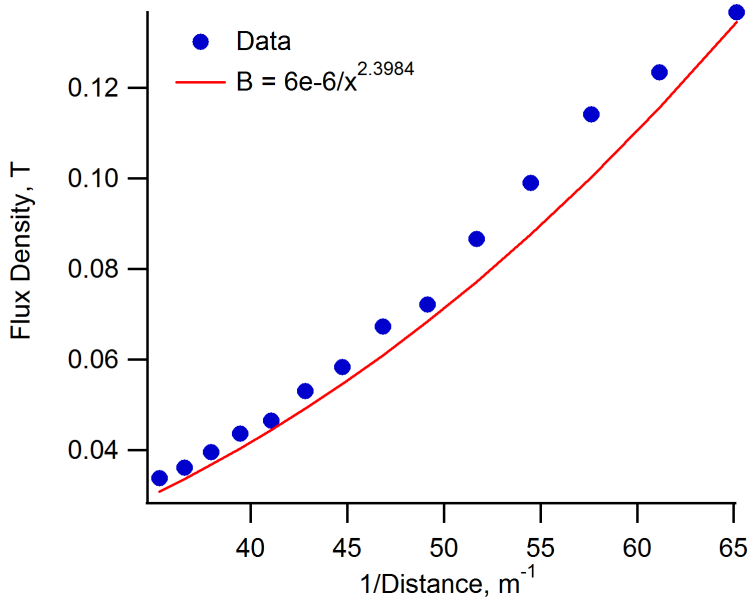

Figure 3.14: The magnetic field of the permanent magnets used in preliminary designs was experimentally determined and fit using a power relationship.

a strong coercivity [61], so I can assume that, although the strength of the magnetization increases, it is slight compared with the magnetic force. I designed a cam-slider system that can move the magnet with a desired profile, Figure 3.15. In order to create the cam for

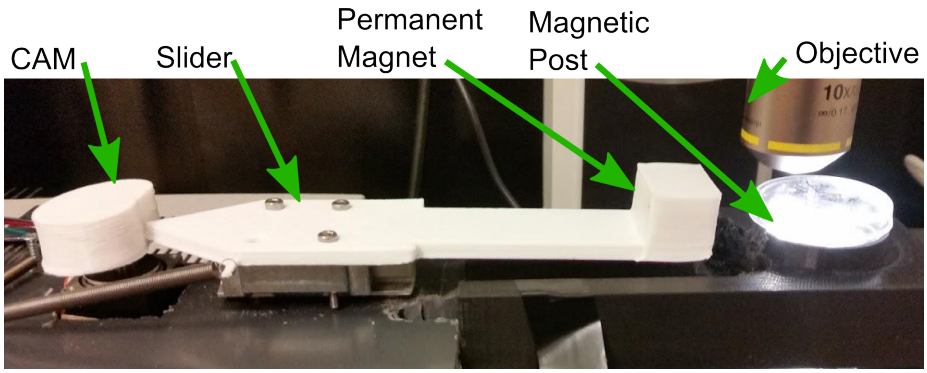

Figure 3.15: The magnetic field of the permanent magnets used in preliminary designs was experimentally determined and fit using a power relationship.

use in the cam-slider setup, I used a series of equations starting with the force on the post compared with the position of the magnet given by

$$F = \frac{A}{x^{3.3984}} \tag{3.2}$$

where F is the force on the post, A is a constant, and x is the position of the magnet. The radius at any point is then determined by

$$r(\theta) = r_0 - x \tag{3.3}$$

where r_0 is the distance from the midpoint of the cam to the post, and r is the radius of the cam at that point, and θ is the angle of rotation of the cam. In order to more accurately perform dynamic studies of the system, I would like to apply a sinusoidal force to the post so that changes in amplitude and phase lag can be directly determined from the motion of the post. In order to accomplish this, I will produce a complete sine wave of force through one revolution, resulting in a force defined by

$$F = B\left(\cos\left(\theta\right) + C\right) \tag{3.4}$$

where B and C are constants greater than one to control the final desired force and position. By combining Equations 3.2, 3.3, and 3.4, the radius of the cam at any position θ can be determined by

$$r(\theta) = r_0 - \frac{A}{B\left(\cos\left(\theta\right) + C\right)^{\frac{1}{3.3984}}}. \tag{3.5}$$

The constants A, B, and C can be modified to provide the desired force, position of the magnetic, and radius of the cam.

Using additive printing (MakerGear), I created a custom cam profile and placed it onto a stepper motor (1205, Pololu) to actuate the custom-made slider. Several prototypes for the cam were created using additive printing during the development of the prototype system. The entire system was controlled using LabView. The top of the post was imaged over the duration of each experiment using an Orca-Flash 2.8 camera (C11440-10C, Hammamatsu), and the stepper motor was controlled using an LM555 timing circuit with varying resistors to control the frequency, Figure 3.16. At the start of each experiment, the motor was triggered

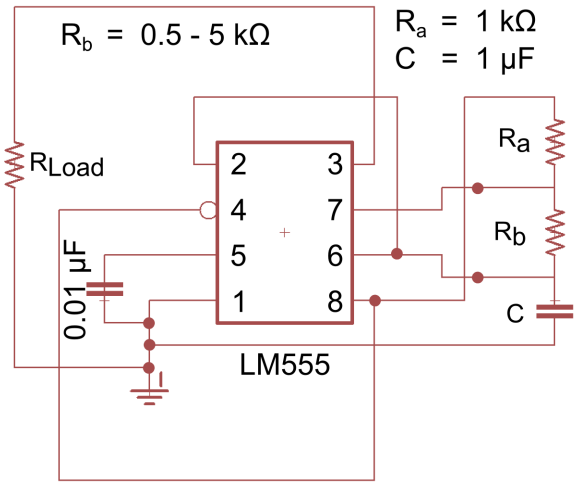

Figure 3.16: An LM555 can be used to control the frequency of the stepper motor without the need for additional timing controls. The frequency is set by changing the value of R_b.

to start using the timing mechanism of the motor control board (1182, Pololu), and each step

of the motor was read into LabView. Furthermore, the position of the cam at the lowest and highest magnet position was read using a photointeruptor circuit to ensure that the motor was not skipping any steps.

I implemented the dynamic permanent magnetic motor drive on the large post described in Chapter 2, as well as on the 20 μm diameter microposts with nanowires that are described above. Using the cam in air, a sinusoidally varying position of the post is produced, Figure 3.17. As expected, the posts move in a sinusoidal motion as determined by the force from

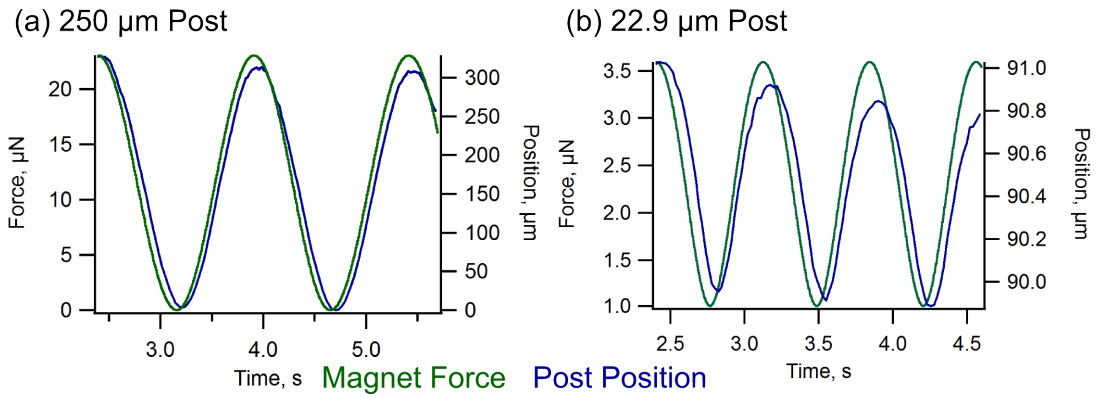

Figure 3.17: Sinusoidally varying forces produce sinusoidally varying positions for (a) a 250 μm diameter post and (b) a 20 μm diameter post.

the magnet described in Equation 3.2. The force of the post determined using a uniformly distributed load also correlates with the force on the post expected from the measured magnetic gradient and the volume of material in the post. The volume of iron in each post is $4.3{\cdot}10^{-11}$ m^3. The susceptibility of iron is between 500-5000, and the gradient of the field is defined by the relationship shown in Figure 3.14. This results in an estimated magnetic moment of $6.42{\cdot}10^{-8}$ Am^2. This has some error due to the exact volume of material in the post, and any errors in the exact position of the magnet. The actual force is within an order of magnitude of this number, and can be altered as before by knowing the motion of the post in air.

Final Permanent Magnet Design

The original intention of this aim was to dynamically control the force on the magnetic posts so that the viscoelasticity of shear-developed platelet clots could be investigated *in situ*. Ultimately, I modified the experiment to provide a static permanent force so that more clots could be investigated in each experiment, and to increase the magnitude of the force applied to the posts.

One of the main challenges of the method described above for dynamically creating magnetic forces is that the magnetic force must come from the side of the device. Additionally, it requires significant space that can be vital during experiments. The space on a microscope stage within a climate-controlled box to keep conditions at 37 °C is limited. Due to the lack of space and challenge with bringing in a magnet from the side, I chose to use a metallurgical microscope (LV-100, Nikon) so that a magnet could be used from below the microscope slide. By positioning the magnet below the microscope slide, the minimum distance to the posts could be lowered from 10 mm to less than 3 mm. As described above, the magnetic field follows a power law decrease from the source of the field. Shortening the distance to the permanent magnetic caused a significant increase in magnetic force.

I built a custom holder for the microscope slide so that a space below the slide could be open for a permanent magnet, Figure 3.18. The custom holder was built with additive printing, and a slider for the permanent magnet was built for applying forces. The post motion with this setup caused typical deflections of 1-6 μm, Figure 3.19 The total force on the post can be described using the description of the magnetic force from Chapter 2, Equation 2.11, again assuming that the magnetic force acts uniformly along the length of the post. This results in a stiffness of 86 nN$\cdot\mu$m^{-1} for a post with a diameter of 19 μm and a height of 77 μm. Using this method, the typical force applied to the posts ranged from 150 to 2500 nN.

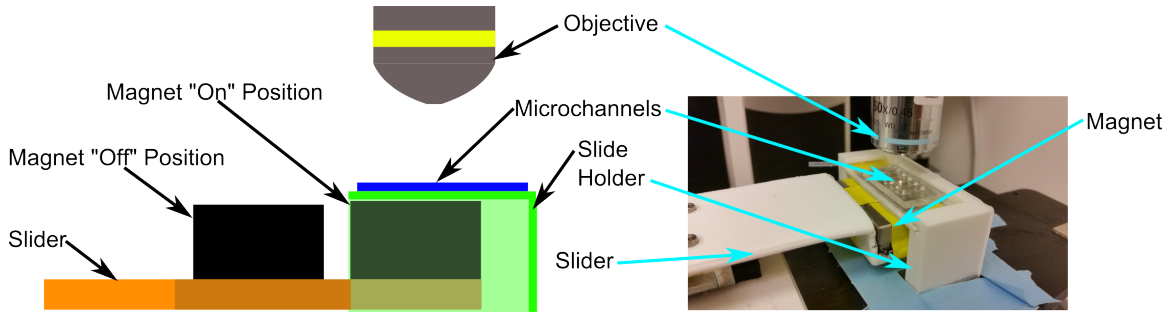

Figure 3.18: A custom holder and slider system was built to hold a microscope slide to facilitate a permanent magnet moved beneath the microchannels with magnetically active posts.

3.4 Experimental Overview

The use of the device described above consisted of characterizing the post motion and measurement error, following by ensuring that the post was sufficient to measure platelet clot stiffness, and then was used to determine the stiffness of clots with no treatment, and clots treated with blebbistatin.

3.4.1 Image Analysis

Image analysis was performed with Matlab, and consisted of both automated and manual analysis. Initially, I developed an automatic analysis program that used image correlation to determine the location of the block and post in each image. The program was somewhat dependent on the choice of rectangle for the block and post regions, and it did not track the post for large deflections. Due to the issues with tracking the post, automatic image correlation was used to track the edge of the block in each image, and manual positioning of a square was used to track the post, Figure 3.20. A cropped and zoomed in region of the post was used to reduce measurement bias. The displacement was determined by the difference in distance of the actuated compared with the unactuated post. Due to the approximately 0.5 μm precision of placing the center of the posts in an image, posts with initial deflections

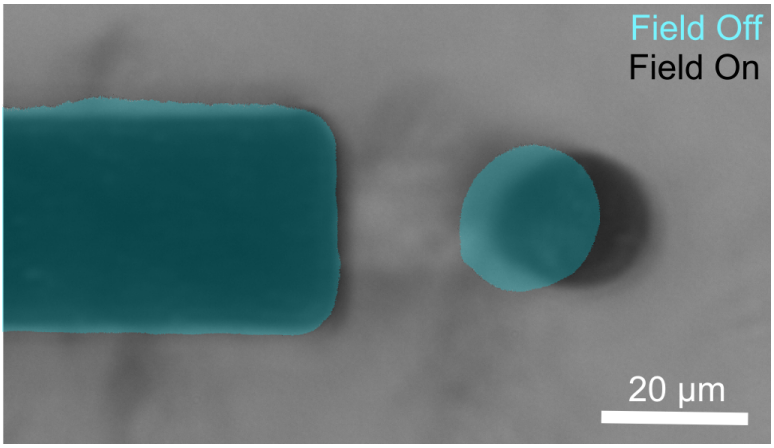

Figure 3.19: Microposts were forced to move under the presence of a magnetic field, resulting in typical deflections of 2-30 μm

of less than 1 μm were removed from analysis. Additionally, posts with a final deflection of less than 0 μm were excluded from analysis, as the stiffness may be greater than indicated by the experiment.

3.4.2 Measurement Error Characterization

Devices with posts inside channels were prepared as described above. Tyrode's buffer was flowed into the channel to simulate optical conditions of posts used in experiments. Images of each post were taken with a 50x objective on a metallurgical microscope (LV-100, Nikon). Posts in five channels on a microscope slide were imaged, then a magnet was positioned below the posts using the setup shown in Figure 3.18, and images of each post in each channel were taken again. After taking "before" images of all of the posts, the posts were removed from the slide holder, and more Tyrode's buffer was flowed into the microchannels. The slide was again placed on the slide holder, and "after" images of each post were taken in the same manner without a magnetic field, then the magnet was moved under the posts, and images were taken of each post again.

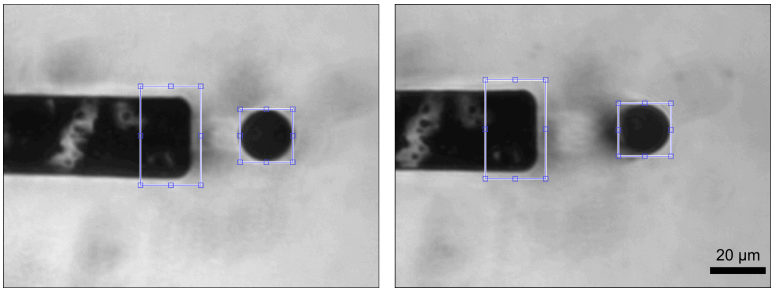

Figure 3.20: The position of the block in each image was determined using image correlation of a portion of the original block while the post was manually positioned. Manual positioning of the post was required due to large deflections and platelet aggregation.

3.4.3 Calculation of Modulus

The calculation of the modulus of the clots or collagen gels used in this section can be determined in a similar manner to methods used in Chapter 2. The methods vary, as this method directly pulls on the clot to apply strain. The Winkler foundation method is no longer valid, and the stiffness contribution of the clot or biomaterial can be determined by

$$k_c = \frac{\delta_i k_p}{\delta_f} - k_p \tag{3.6}$$

where k_c is the stiffness of the clot or gel, δ_i is the initial motion of the post, k_p is the stiffness of the post based on the dimensions and modulus, and δ_f is the final displacement of the post after a gel or clot has formed in the microchannel.

The modulus can then be calculated from k_c by relating the assuming that the clot only adheres between the post and block and adheres over the full length of the post. For a post undergoing rigid body motion the result is

$$E_c = k_c \frac{L_0}{dh} \tag{3.7}$$

where E_c is the modulus of the clot or gel, k_c is the stiffness from Equation 3.6, L_0 is the distance from the block to the post, d is the diameter of the post, and h is the height of the post [69]. In this system, the entire post does not translate, but, as shown in Chapter

2, it can be assumed that the shape follows a uniformly loaded beam and the length can be integrated along the shape of the post described in Equation 2.6. The result then leads to

$$E_c = k_c \frac{L_0}{d} \frac{15}{6h} \tag{3.8}$$

where the factor of $\frac{15}{6}$ is due to the shape of the post described above.

3.4.4 Characterization with Collagen Gels

The devices were further characterized with collagen gels to determine the effectiveness of the devices and the use of Equation 3.8 to determine the Young's modulus. Collagen was chosen as previous data had been generated, as shown in Chapter 2, that could be referenced. Collagen gels were prepared in 3 mg/mL concentrations as per the methods described in Chapter 2. Images of the posts were taken after Tyrode's buffer was flowed in the channels, then collagen was deposited into the posts, the inlet and outlet ports were mechanically removed, and the posts were imaged again. Collagen gels were allowed to sit for 90 minutes at room temperature before imaging began. Two different gels were characterized in a total of five channels with 33 posts reaching the threshold required for inclusion into analysis described above.

3.4.5 Shear Activated Blood Flow

Microchannels were prepared for use by flowing reagents in several steps. First, a 60 μg/mL solution of DiI (D282, Molecular Probes, Eugene, OR) in water was flowed into the channels. Initial testing revealed that DiI did not leave a uniform stain in the microchannels for tracking the posts, so it was only used in subsequent experiments to help verify the seal of each channel. DiI remained in the channel for several minutes, then was removed using a back-flow of ethanol, followed by a forward-flow of calcium-free Tyrode's buffer solution. The channels were then coated with a 200 μg/mL solution of rat-tail collagen type I (354249, BD Biosciences, Bedford, MA) in 0.1 M acetic acid by back-flowing the collagen solution and incubating the devices in a 20 °C refrigerator for 60 minutes. The final preparation step was

to remove the collagen mixture with another flow of calcium-free Tyrode's buffer. Channels were left in petri dishes with an additional petri dish containing a small amount of DI water to reduce evaporation of the buffer solution. Before running the experiment, channels were allowed to sit in a 37 °C environment to aid in platelet plug formation.

Experiments were performed using IRB-approved procedures for collecting blood. Blood was collected in citrate lined tubes and transported from the medical facility to the Cell Biomechanics Lab with a final volume of 25-35 mL. Blood used for all experiments was used 90-120 minutes after drawing blood. After collection, all of the blood was pooled and deposited into 50 mL tubes, except for the first collected citrate tube. Blood was drawn into a syringe, then connected to tubing to a three-way valve.

Under an inverted microscope at 37 °C, tubing from the blood and tubing from calcium-free Tyrode's buffer were connected to a three way valve with the outlet connected to the inlet of the microchannel with a blunt fill needle. The outlet of the microchannel was connected with a blunt fill needle to a 50 mL tube for collection of excess blood and buffer. Blood was flowed into the channels at a rate of 12 mL/min to produce shear rates in the channels of approximately 16,000 s^{-1}. The rate of 12 mL/min was held for 45 s, then reduced to 0.5 mL/min and stopped. The valve was switched to stop the flow of blood and allow buffer to flow through the channels. Buffer was flowed at a rate of 0.5 mL/min until the channel appeared clear for further imaging, which typically used 2 mL of buffer.

The initial channel of each experiment was run at the high shear rates for only 15 s, and the results were excluded from analysis. The volume of blood used was 5 mL, and that resulted in a total use of 30 mL of blood per experiment, the maximum allowed. Early experiments showed increased platelet aggregation in the second and third channels run each day. Increased aggregation resulted in more posts with visible platelet plugs that could be analyzed.

Immediately after flowing blood through all of the channels, inlet and outlet ports were removed from the substrate, and the substrate was transferred to the magnetic actuation device. Each post was imaged with the magnetic field off, then the magnet was moved under

the slide, and each post was imaged again. The magnetic actuation device was operated at room temperature.

3.4.6 Treatments with Blebbistatin

Experiments were also performed with blood incubated with blebbistatin, a drug used to inhibit myosin II activity. Blebbistatin (856925-71-8, Sigma-Aldrich, St. Louis, MO) was initially at a concentration of 17 mM in dimethyl sulfoxide (DMSO) and added to the blood to form a final concentration of 15 μM. DMSO was added to the control blood in the same volume as blood with blebbistatin. Flow of blood through the channels was the same as described above. Calcium-free Tyrode's buffer with the same concentration of blebbistatin was used to ensure that the effects of blebbistatin were not washed out in the channels when performing stiffness measurements.

In general, each experiment compared one channel with blood with DMSO and one channel containing blood treated with blebbistatin. Approximately 20-30 posts could be imaged per channel, although several were often previously non-vertical and removed from analysis.

3.5 Results

The device was characterized to test the measurement errors as well as the response of the post-block system to viscoelastic biomaterials. Furthermore, the device was demonstrated for the measurement of platelet clot stiffness for control blood and blood incubated with blebbistatin. This section will detail the results of the characterization and experiments.

3.5.1 Measurement Error Characterization

In the simulated characterization experiment for measurement error, an initial post deflection was measured, followed by removing the channels from the magnetic actuation device, running buffer through the channels, then returning the substrate to the magnetic actuation device to measure a second deflection, Figure 3.21. The result of my characterization

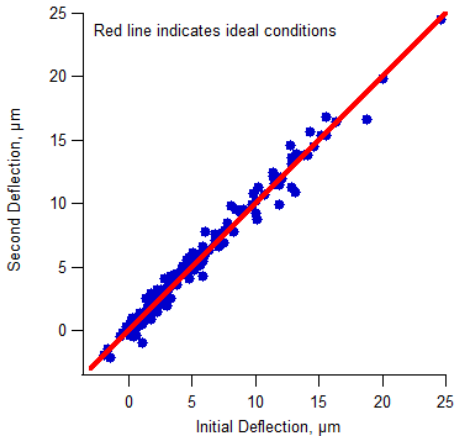

Figure 3.21: Deflections were consistent after moving the substrate away from the magnetic actuation device and simulating experimental conditions with buffer before measuring the deflections again.

showed that the force was consistent, even after the slide had been removed and replaced. This meant the post-by-post comparisons of the position could be used to measure the force applied to the clots, and the final displacement was due to the stiffness of the clot.

3.5.2 Characterization with Collagen Gels

Collagen gels resisted the motion of the post and the modulus of the collagen gels was two orders of magnitude greater than that calculated for air, Figure 3.22. Furthermore, results indicated a Young's modulus on the same order of magnitude as previously described in this thesis, Table 2.1. The slight offset from zero for the modulus of air can be attributed to measurement error. These results indicate that the device is capable of measuring material stiffnesses with sufficient accuracy for understanding biomaterials.

3.5.3 Shear Activated Platelet Blood Flow

Platelet-clots were formed on many posts under shear flow through the microfluidic channel. Plugs either formed between the block and post, or solely around the post. Plugs that formed

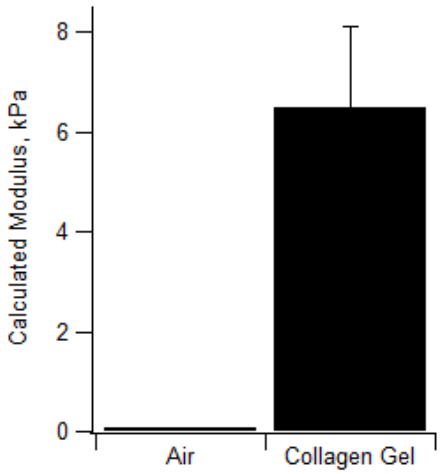

Figure 3.22: The calculated modulus of collagen was on the same order of magnitude as previous results discussed in this thesis and elsewhere. The modulus was significantly more than the modulus calculated for posts in air that was attributed to measurement error. (n=33 posts, N=2 gels)

between the block and post resisted magnetic forces, Figure 3.23

During the flow through the channels, the posts were observed to bend backward. This result was replicated by flowing water through the channels at the same flow rate of 12 mL/min. The flow of water indicates that the effect is not likely due to blood, but is due to the drag on the post of the fluids. Due to the significant backwards bend of the posts and a limited viewing window, forces on the clots over time were not tracked in these experiments.

After transferring the substrate to the magnetic actuation system, each post and block was imaged before and after applying a static magnetic field. There were three typical conditions of platelet plugs that had formed around the block and post. In the first condition, platelets adhered to the surface of the block and post but did not attach between the two structures. The second condition had a larger plug that nearly reached the block, but may not have fully adhered. The final condition was one that had plugs that fully formed between the block and post. In order to be included as a calculation of stiffness, the initial post

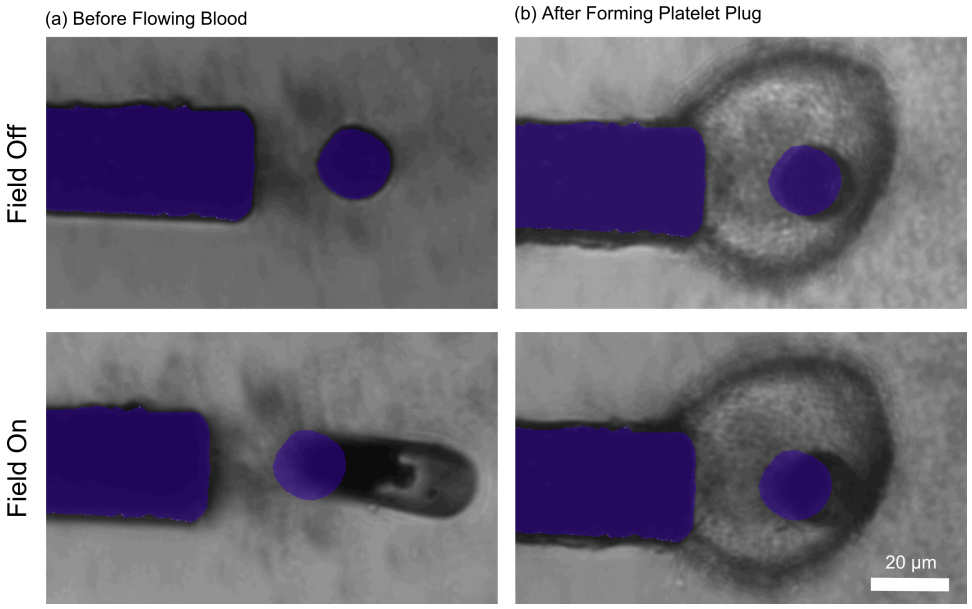

Figure 3.23: Platelet plugs formed on the posts under shear flow resisted the motion of magnetic forces compared with the initial displacement of the post.

deflection had to be greater than 1 μm and the final deflection had to be greater than 0 μm. There were typically 2-5 posts in each channel that had clots between the posts and blocks and met the post motion conditions. There was not a clear indication as to why clots formed on some block and posts and not others. There may be other defects causing clots to form, and there is room to investigate this further.

Clots produced stiffness that was measured with the system and found to be 13 $\pm$ 3 kPa. As shown in Figure 3.24, posts had conditions where full plugs formed and where plugs did not reach the block. In order to demonstrate that the measurement of stiffness was not due solely to changes in the applied magnetic force, Figure 3.25 shows the comparison of stiffness calculated for posts that did not have full plugs and posts that had visible plugs between the post and block. These results indicate that this tool can be used to measure clot stiffness and understand the effects of different inhibitors to measure clot stiffness.

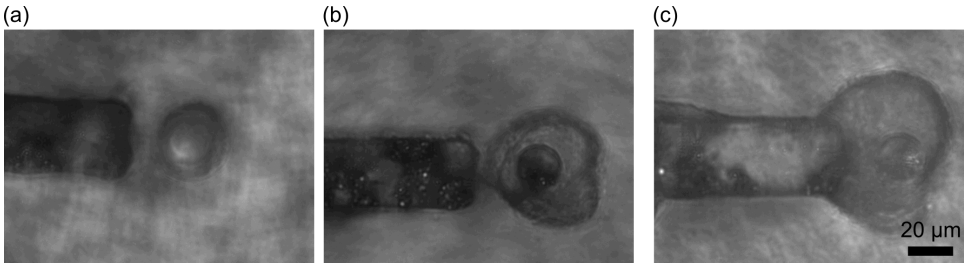

Figure 3.24: Three types of platelet plugs formed between on the magnetic posts, and the images are three different posts. (a) Platelets formed a small layer around the post causing it to appear slightly larger than normal. (b) Platelets formed a larger plug around the post, nearly reaching the block but not adhering. (c) Full plugs formed between the post and block, and this condition was used to analyze the stiffness of the plugs.

3.5.4 Treatment with Blebbistatin

Platelet plugs formed on the posts with blebbistatin, and initial results indicate that there may be a difference in stiffness between blood treated with blebbistatin and control. The results are not yet conclusive, and several modifications to this experimental conditions could be made to ensure that there are not other underlying effects of the system that would affect the stiffness of plugs formed by platelets that had been treated with blebbistatin.

3.6 Discussion

I have successfully demonstrated the use of magnetic microposts to measure the elasticity of shear-developed platelet clots *in situ*. The device that I presented was characterized and showed measurement errors much lower than the differences due to clots and gels. I further characterized the device to show that it could be used to accurately predict the modulus of collagen. Furthermore, I measured the stiffness of shear-developed platelet clots, and shear-developed platelet clots that were treated with blebbistatin.

Several groups have investigated the stiffness of blood clots under a variety of conditions, and there are a wide range of results from 0.5-83 kPa [112]. Part of the reason for the wide range of results is that the thrombi were derived using different methods. Typically,

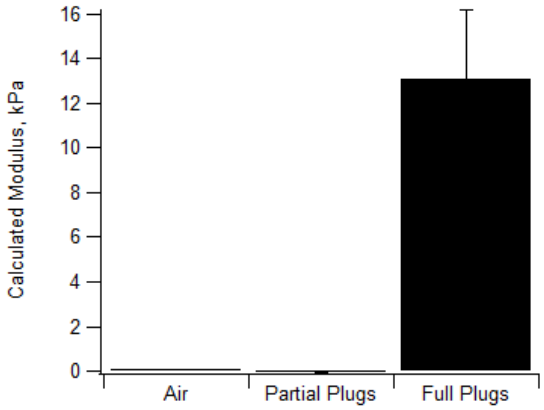

Figure 3.25: After pulling on fully formed clots with magnetic posts, the stiffness of the clots could be measured. The stiffness was far greater than any differences in applied magnetic fields.

clots are formed using plasma or blood combined with calcium or other clotting factors. In some cases, clots were surgically removed and tested. In this paper, I have shown an *in-situ* method for measuring clot modulus, and found it to be within the range of moduli reported by previous groups.

The device developed in this section can be further extended to directly compare force generation and viscoelastic properties of platelet clots formed on microposts. Current methods only describe viscoelastic properties or force generated [27], and this technique can enable the ability to investigate both simultaneously.

This work demonstrates a new tool for measuring clot elasticity and the method can be further enhanced by performing more experiments to understand the effects of different antagonists on clot elasticity.

Chapter 4

MAGNETIC SENSING AND FABRICATION OF HOMEMADE SENSORS

One of my initial goals for my thesis was to measure the magnetic field change of the bending microposts. My goal was to modify version of the system developed in Chapter 3 to magnetically measure the deflections of posts. In this chapter, I will detail some of my work towards that goal and the complications that arose while attempting to measure the magnetic field changes. Ultimately, I did develop a magnetic sensing system that I will describe in Chapter 5, although due to the physical limitations of the system, it is used to measure twitch forces of engineered heart tissues.

4.1 Device Overview

My initial plan was to seed nanowires into the PDMS posts. Nanowires are advantageous for this application as they retain a magnetic dipole along the axis of the wire even after an external magnetic field has been removed. Posts have been showed to deflect as a platelet clot compresses between the block and post, and my plan was to place a sensor below the post to measure the field change of the rotating dipole, Figure4.1. After using four different technologies for commercially available magnetic sensors, I then attempted to create my own giant magnetoresistive (GMR) sensors, or spin valves, in the Washington Nanotechnology Facility at the University of Washington. The goal of creating custom GMR sensors is to position the post as close as possible to the sensor. I was unable to reach the sensitivity required for this application, but the work could be continued in the future.

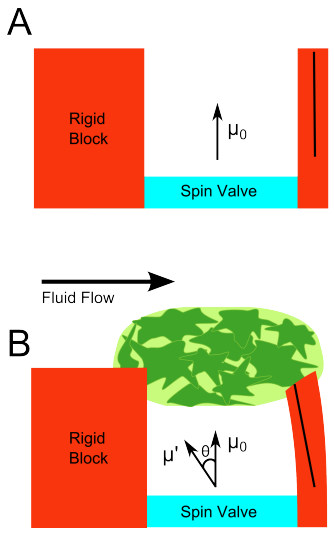

Figure 4.1: Overview of device plan for measuring the magnetic field change of a post with an embedded nanowire. In an (a) undeflected state, the dipole is oriented vertically. After flowing blood and forming a platelet plug, the post (b) bends toward the block resulting in a change in the projection of the magnetic field on the sensor located below the post.

4.2 Magnetic sensor Modeling

In order to determine the feasibility of magnetic sensing with the nanowires. I developed a simple dipole model of the nanowires to determine the expected magnetic field change. This model helped to inform the signal to noise ratio that would be required for the sensing system. I approximated the wire as a dipole, with a strength determined by its volume and remnant magnetization,

$$\boldsymbol{B} = \frac{2\mu_0 MV}{4\pi \boldsymbol{r}^3} \tag{4.1}$$

where M is the remnant magnetization for the wire, V is the volume of the wire, μ_0 is the permeability of free space, and r is the distance from the embedded nanowires to the magnetic sensor. I modeled a system for single nanowires to determine the how the size of the sensor might affect the ability to measure the magnetic field, and to see how sensitive a device may need to be for measuring post deflections, Figure 4.2.

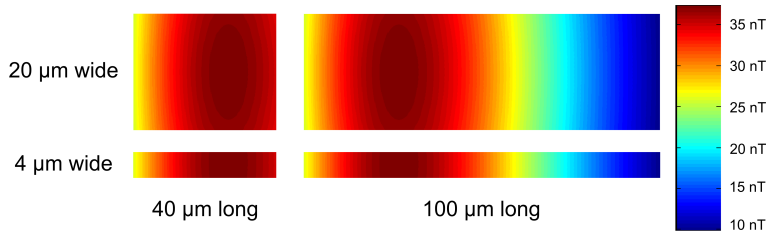

Figure 4.2: Smaller magnetic sensors located 20 μm ahead of the nanowires is the optimum location for magnetic sensors. Wires rotating 30 degrees can produce field changes of up to 35 nT.

Although understanding the field generation of single nanowires can help inform sensor types and sizes, the device used to measure platelet forces are ultimately sensor arrays. I extended the model in Equation 5.1 to model multiple nanowires in an array. The configuration is as shown in Figure 4.3, and the model continues to assume that the wires are dipoles,

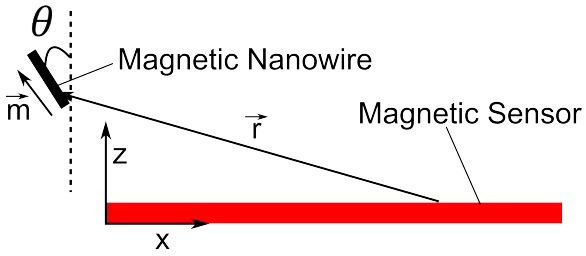

Figure 4.3: Model for magnetic nanowire rotation. Wires are treated as dipoles, and the magnetic sensor is located on a plane below the nanowires.

resulting in Equation 4.2,

$$B_{xrot} = \sum_{i=1}^{n} \frac{\mu_0 |\boldsymbol{m}|}{4\pi} \int\int \frac{3\left(z\cos\theta - (x-p)\sin\theta\right)(x-p) - |\boldsymbol{r}_i|^2 \sin\theta}{|\boldsymbol{r}_i|^5} dxdy \qquad (4.2)$$

where B_{xrot} is the final magnetic field of the sensor, $\boldsymbol{m}$ is the magnetic moment of an individual nanowire, θ is the rotation of the nanowire due to the platelet clot, x is the position on the sensor, p is the offset of the nanowire from the origin, and n are the number

of nanowires. The result of this model is a way to measure the magnetic field of an array of nanowires as they simultaneously bend due to platelet clot contractions. I found that the field produced by nanowires rotating three degrees ranges from 10-150 nT based on the distance to the sensors, and the orientation of the sensor.

4.3 Commercial Magnetic Sensors

I started towards the goal of creating a magnetic sensing system by using commercially available magnetic sensors. I used several technologies and experimental designs to test the sensors and attempt to generate stable signals with enough signal to noise. I used sensors that used different effects, such as anisotropic magnetoresistance (AMR) (HMC1001, Honeywell, Morristown, NJ), giant magnetoresistance (GMR) (AAH002-02, NVE, Eden Prarie, MN), fluxgate sensors (FLC 100, Stefan Mayer Instruments, Dinslaken, Germany), magneto-inductive sensors (MI) (MicroMag3, PNI Corporation, Santa Rosa, CA), and Hall effect sensors (Model 410, Lakeshore, Westerville, OH). Ultimately, the most promising sensor technologies were the fluxgate sensors and the giant magnetoresistive sensors. Fluxgate technology showed promise as a stable senosr; however, the expected signal was not observed experimentally when bending nanowires. I ultimately performed the remaining experiments with commercial sensors using GMR technology.

4.3.1 Bare Die Sensors

As described above, one way to improve the signal from the rotating nanowire is to locate the nanowire closer to the magnetic sensor. After determining that the GMR sensors had the highest potential for sensing, I attempted to reduce the dimension from the nanowire to the sensor. Standard dies for surface mount components are approximately 1.5 mm thick. The sensing elements are mounted in the middle of the die, resulting in a distance of at least 0.5 mm from the sensing elements to the nanowire, and an additional 0.1 mm for the smallest coverslip dimensions. To alleviate some of the issues with distance, I mounted bare die sensors (AAH002-02, NVE) onto custom PCB boards, Figure 4.4. Connections from the

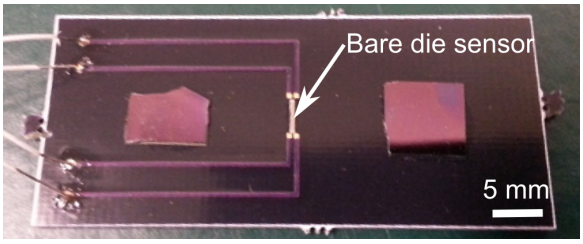

Figure 4.4: Bare die sensors were used to reduce the distance from the nanowires to the sensing element (r in Equation 4.2).

die to the PCB was performed using a ball-wedge gold bonder with 25 μm wire diameter at a power of 350 mW for 45 s, and it was performed with the plate at 100 °C and the tool at level 6.0 with high force. This did help to increase the signal, but the noise was still significantly more than the signal.

4.3.2 Filtering and Lock-in Amplification

The expected signal from the rotating wire was a slowly increasing change as the post bent due to platelet forces. This proved to be difficult to sense as the signal was similar to drift in signals and low frequency noise could not easily be removed from the system. The signal had a frequency on the order of 0.01 Hz, so a sufficiently steady signal needed to be generated for several minutes at a time to find the signal. I attempted to use multiple sensors to capture drift, but observed that the sensors did not have a direct relationship to ambient noise. There are likely slight differences in the manufacturing of the sensors as they are stacks of metal that result in a 100 nm tall structure. Heating, cooling, and stray magnetic fields contributed to the drift, and I used magnetic shielding to reduce the effects of magnetic noise, but I still found other drift due to heating and electrical noise.

I attempted to reduce electrical noise through the use of a lock-in amplifier. The goal was to produce current through the sensor at a frequency, and then determine the magnitude at the output with the same frequency. Although the lock-in amplifier showed promise towards

generating a strong signal, the result was that the signal still drifted due to other noise in the system.

4.3.3 Experimental Results with Commercial Sensors

I used the model described in Equation 4.2 along with sensor data sheets to determine the expected voltage change for 10 wires rotating 30 degrees over a sensor, and experimentally observed the drift of the sensors over time. I found in multiple cases with different filtering and sensing techniques that the drift was more than the expected change, and that the drift was not consistent between sensors, so it could not be eliminated through the use of multiple adjacent sensors, Figure 4.5. In addition to drift, another challenge of magnetic sensing was

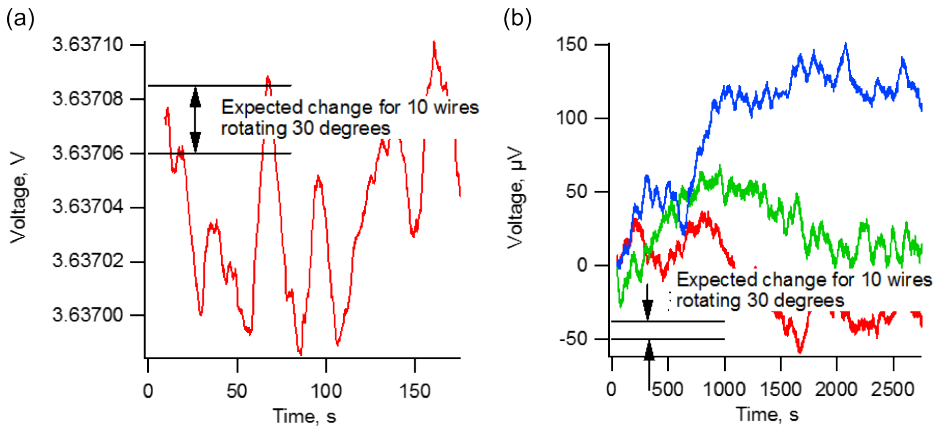

Figure 4.5: The (a) drift of magnetic sensors was significantly larger than the expected signal. Furthermore, (b) the drift was not consistent between sensors.

the relative location of the sensors to the microposts with embedded magnetic nanowires.

4.4 Homemade Magnetic Sensors

Commercial sensors proved to not be sufficiently sensitive for measuring the magnetic field of nanowires rotating, but proper design of magnetic sensors could improve the signal generation by maximizing the location where the signal is the strongest. I will detail how I

successfully fabricated magnetic sensors; however, the magnetoresistive effect of the sensors that I developed was much smaller compared with commercial sensors.

Giant magnetoresistive sensors are stacks of thin layers of metal that interact differently depending on the external magnetic field and the spin of electrons in layers adjacent to a conducting layer. Several different designs have been proposed for the combination of metals in the stack, and I chose to attempt to use the one used by Martins, et al.[78]: Ta 20Å/MnIr 80Å/CoFe 20 Å/Cu 22Å/CoFe 24 Å/NiFe 30Å/Ta 20Å.

4.4.1 Fabrication Overview

The fabrication of the magnetic sensors used standard clean room processes, Figure 4.6. First, an oxide layer was grown on the entire spin valve to reduce the resistance of the wafer.

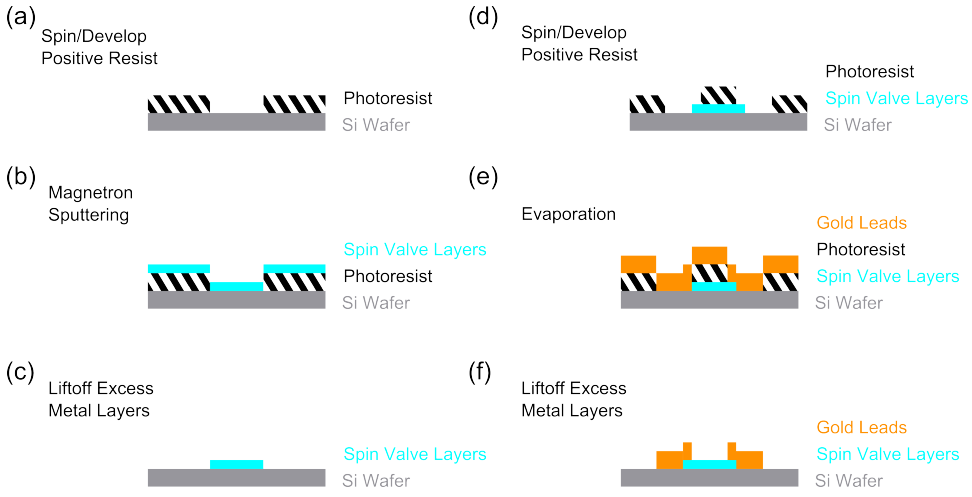

Figure 4.6: Magnetic Sensors were fabricated using standard clean room processes. First, (a) AZ1512 was spun onto silicon wafers and developed, then (b) sputtering was used to deposit GMR sensor materials and (c) then the excess material was removed in acetone. (d) The wafer was again patterned with photoresist, then (e) evaporation was used to deposit leads, and (f) excess material was removed in acetone.

The first design I used omitted the oxide layer, and did not produce a GMR effect. The oxide layer was grown in a wet oxidation furnace for 20 minutes at 1050 °C. After growing an oxide

layer, spin valves were patterned using positive photoresist (AZ1512) and exposing the wafer to UV light (ABM Aligner), then developing the resist in AZ340. Patterned wafers were sputtered using magnetron sputtering (LAB 18, Kurt J. Lesker Company, Jefferson Hills, PA) to achieve the desired design. The pattern was removed using lift-off of the sensors, then the wafer was patterned for electrical leads using positive photoresist. Either gold or aluminum leads were evaporated onto the wafer at a thickness of 1 μm, then lift off in acetone to form the final structures, Figure 4.7.

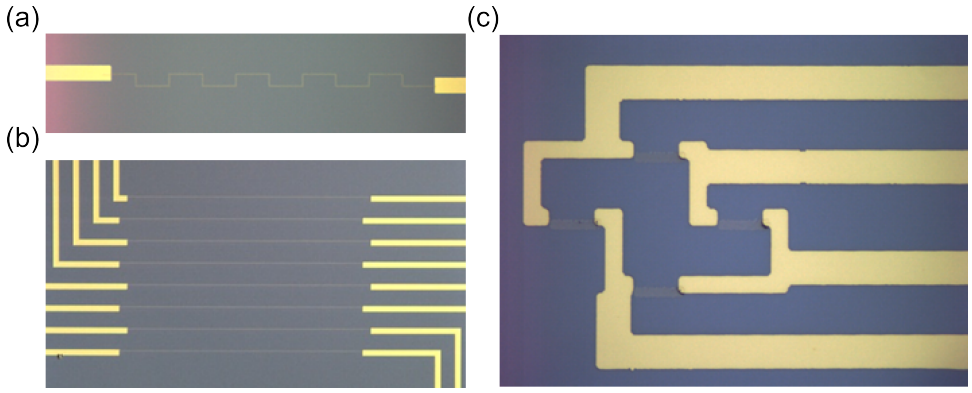

Figure 4.7: Several different patterns of magnetic sensors were used and connected with either gold or aluminum leads to larger pads for connections to external electronics.

The main parameters to change in the system were related to the sputtering of the spin valve layers. I varied the power and chamber pressure of the system to try to achieve the best layers and determined the sputtering rates for the system at 100 W and chamber pressure of 20 mTorr, Table 4.1. I characterized the thicknesses by using a profilometer and sputtering each metal for 600 s. Ultimately, I think the rates overpredicted the final sputtering rate. Wafers with a reduced sputtering rate at a reduced chamber pressure (5 mTorr) produced the best results. The layer with the tightest tolerance is the copper layer, and I extensively studied how the power and pressure affects the sputtering rates of copper.

Table 4.1: Experimental sputtering rates 100 W and 20 mTorr

Metal	Deposition Rate (Å/s)	Required Thickness (Å)	Expected Time (s)
Ta	0.67	20	30
MnIr	0.83	80	96
CoFe	0.67	20	30
Cu	0.83	22	26
CoFe	0.67	24	36
NiFe	0.83	30	36
Ta	0.67	20	30

4.4.2 Experimental Results

I did find a slight magnetoresistive effect from some of the sensors that I fabricated on using magnetron sputtering system. The GMR ratio was only 0.2%, Figure 4.8. Typical GMR ratios range from 5-10 % for commercial sensors as well as senors created by other research groups [78]. Eventually, I decided to go in a different direction with magnetic sensing for this and other projects.

4.5 Potential Future Directions

Although magnetic sensing of nanowire deflection in microposts proved to be unsuccessful for me, I think that there are some potential opportunities for future work in this area. One limitation of our group was using a shared magnetron sputtering system. A potential opportunity to revisit custom magnetic sensors would be the use of an ion beam deposition system [120]. Spin valves require significant fabrication knowledge and technique understanding, and partnering with groups who have previous experience in spin valves could potentially

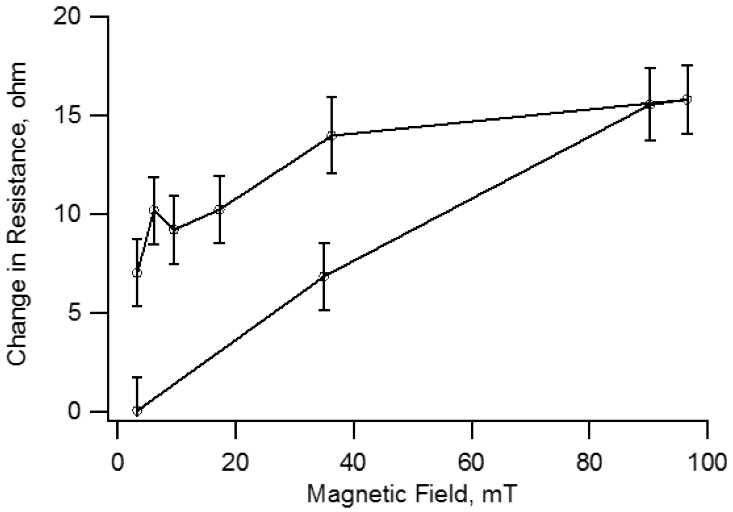

Figure 4.8: Homemade spin valves had a GMR ratio close to 0.2%, much lower than commercial spin valves and devices created by other groups.

improve the work.

Another challenge in magnetic sensing was the low frequency drift of all of the different sensors. Low frequency drift is generally difficult to eliminate, especially when the expected signal is also moving at a low frequency. Designs that use higher frequency motion of the post or that use a different monitoring or filtering scheme could also potentially help improve the signal to noise ratio.

A final drawback to the system was the seeding density of magnetic nanowires. I described a new device in Chapter 3 that uses larger posts with iron microparticles. I have not investigated the ability to sense positions with the magnetic posts, but the larger posts combined with a higher density of magnetic material could also improve the magnetic field changes due to post motion. It must be determined whether or not there is enough remnant field or if external magnetic fields must be used to cause the post to create a stray field.

Although this work ultimately was unsuccessful in developing a system for measuring the signal of nanowires embedded in microposts, it did inform and aided in production of

the sensing system described in Chapter 5 that was ultimately successful in measuring the twitch force of engineered heart tissues.

Chapter 5

AIM 3: CREATE A MAGNETIC SENSOR FOR MEASURING CARDIOMYOCYTE TWITCH FORCE AND FREQUENCY IN REAL TIME

The third aim of my thesis is to develop a system for measuring cardiomyocyte tissue forces in real time, without the need for a microscope. The goal of this aim is to increase understanding of cardiovascular force, provide a way to determine if there are any day-to-day fluctuations, and create an easy-to-use method to monitor tissues in a easily scalable method. Typically, tissues are measured at discrete time points, as it takes time to set up the microscope and measure the tissue forces. Previously, a device was developed with permanent magnets embedded on the end of posts to apply forces to small cardiomyocyte tissue. I have expanded on this device to use the changing magnetic field at a point below the posts to determine the post tip position, which determines the force of the tissue.

5.1 Cardiovascular Background

The heart is essentially a positive displacement pump that expands and contracts to push the flow of blood through the body. Contractions occur with a frequency of approximately 1 Hz, and abnormal forces can be indicative of diseases [131]. Several methods for creating cardiomyocyte tissues have been developed to better investigate the forces and biology of the tissues [58]. These models are key to forming replacement tissues, as the heart does not have great ability to repair itself after infarctions [44]. Engineered tissues are the key to repairing the myocardium, and monitoring progress of cells and tissues for their force generating capabilities can be one sign of maturity and enhance the likelyhood of a successful repair.

In addition to cardiac repair, cardiotoxicity is a vital aspect of drug screen, and current

methods still allow the occasional unsuitable drug to enter the market, even after rigorous preclinical screening [124]. Drugs can have unpredicted adverse effects on cardiac function, including arrhythmias and reduced or increased contraction [88]. Typical screening methods monitor the response of single cells, but several groups have proposed engineered heart tissues derived from stem cells as a way to enhance screening methods [31].

5.1.1 Engineered Cardiomyocyte Tissues

Several devices and methods have been developed to look at cardiomyocytes and the forces they generate. One method is through the use of single cardiomyocytes that have been affixed to microposts [95]. Monitoring the force response of single cardiomyocytes can provide information about the effects of a variety of reagents and treatments to cells, but these methods require significant efforts to monitor the force generation of cells and are likely limited to the laboratory.

Engineered heart tissues provide a three dimensional environment for cardiac cells that can improve the maturity and similarity to adult tissues for the cells. Two of the primary markers for cardiac tissue maturity and viability are the beating frequency and twitch force. Several devices have been developed to grow engineered heart tissues and measure either beating frequency, or both beating frequency and twitch force [143]. Frequency-only systems include devices that measure beating rates of tissues in microfluidic channels [79] or devices that use microelectrode arrays [84]. There are also several devices that can measure tissue twitch forces, including sheets of cells on flexible flaps [3], sheets of cells on force transducers [140], tissues on polyacrylamide gels [53, 5], and tissues suspended between load transducers [123, 100] or polymeric posts [33, 17]. Of particular note for this thesis are new methods that use tissues made out of cardiomyocytes attached between flexible posts [34, 68, 45]. There are several variations of this method, but the main premise is that cardiomyoctyes are seeded within a fiber matrix that typically consists of collagen, fibrin, or Matrigel. The tissues are able to bend the flexible posts and the force generated by the tissue can be determined by how much the post is bending.

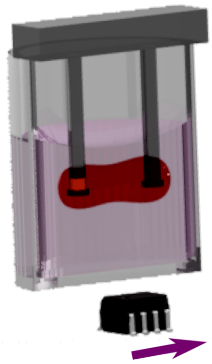

Figure 5.1: Diagram of the device generated for this aim. A tissue is suspended between a flexible post with an embedded magnet and a rigid post. A magnetic sensor is placed below the tissue culture dish.

One challenge of current methods of seeding and monitoring forces from engineered heart tissues is that complicated systems are typically used. In one case, sophisticated image analysis was used to perform monitoring of the motion of two flexible posts over time [116]. The authors were able to measure the force generated by the posts, but it requires a dedicated microscope and a highly complex system for evaluating forces over time. Expansion beyond a single 24 well plate would require additional microscopes, or likely significant setup and tear down for each point of force measurement. It is not likely an acceptable system for expansion to massively parallel studies. Other proposed methods of monitoring the force development of cardiomyocyte tissues either require destructive methods [140], or merely monitor the electrophysiology and not the actual force generation [118, 141, 31].

5.2 Device Overview

The device used for this aim consists of a pair of posts, one of which has an embedded magnet at the tip of the post, and the other post is made rigid through the use of a glass capillary tube. Tissues are suspended between the posts, Figure 5.1, and the flexible post with an embedded magnet moves due to tissue contractions. A magnetic sensor is placed below the

tissue culture dish, and it is capable of detecting the rotation of the magnet embedded in the flexible post, Figure 5.2(e,f). The posts are made in an array to cover a row of a six-well dish, Figure 5.2(b,c,d). Posts are fabricated out of PDMS, and magnets are held in place using another magnet during fabrication. Tissues are grown in wells of a 24 well plate using collagen or fibrin as a matrix, and the cells attach to the end of the posts. After several days, the cells start to beat spontaneously which causes the post with an embedded magnet to bend towards the rigid post. Sensors are placed below the post and read to a computer using a LabView data acquisition system. The sampling rate is 5000 Hz, and can be filtered to produce better results.

5.2.1 Post Array Fabrication

The posts used in this aim were fabricated using PDMS in a custom four-part mold. All baking steps for the posts were performed at 65 °C due to the mold being fabricated out of plastic. Higher temperatures would warp the mold and cause it to deform. In order to create the posts, a small amount of PDMS was poured into the top of the mold to form caps which helped to form the posts without ripping the magnets out of the post. The caps also promoted tissues to form around the tops of the posts. After caps were formed, 1 mm cubic magnets (MyMagnetMan, Largo, FL) were placed into the flexible post side of the mold, and 1.1 mm diameter glass capillary tubes (Drummond Scientific Co., Broomall, PA) were placed into the rigid side of the mold. PDMS was then poured into the entire mold and cured overnight. Large external magnets were used to keep the small magnets in place during curing. The external magnets were held in place with plastic handheld clamps. Metal clamps caused the magnets to move away from the ends of the posts during the curing process. After the posts were removed from the mold, excess PDMS was trimmed away to result in posts that were 12.5 mm tall, 1.5 mm diameter, and spaced 8 mm apart. The effective stiffness of the posts was 0.98 μN/μm, calculated by assuming a Young's modulus of 2.5 MPa for PDMS and that the net tissue force acts at 12 mm.

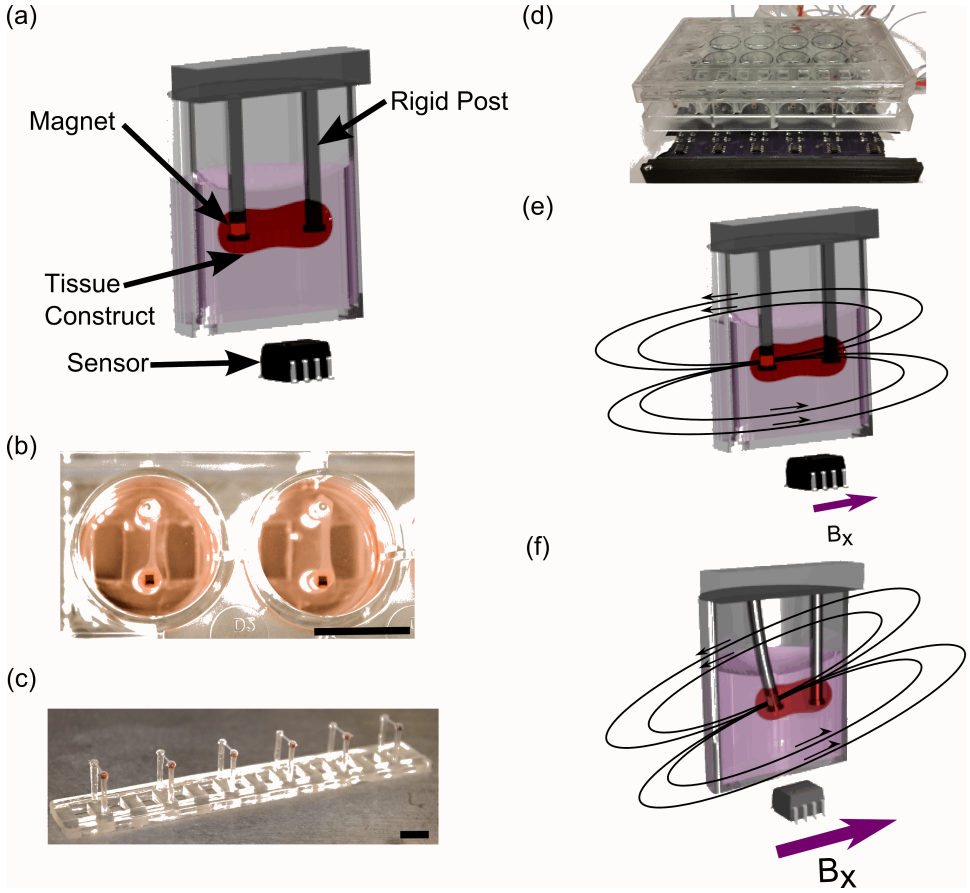

Figure 5.2: Engineered heart tissue between suspended posts produce twitch forces measured by the new system. (a) Tissues are suspended between two posts with a magnetic sensor located below a 24-well plate dish. (b) Tissues normally sit in media and contract, and (c) are in groups of six designed for a (d) 24-well plate system. The magnet in the flexible post moves from (e) its resting state to (f) its contracted state due, and that changes the magnetic field located at the sensor below the 24-well plate.

5.2.2 Magnetic Sensor Array Fabrication

This experiment was limited to using the first row of a 24-well plate, however, simulations indicated that all 24 wells could be measured without interference from adjacent tissues. Magnetic sensors (AAH002-02, NVE, Eden Prairie, MN) were arranged on printed circuit boards (OSH Park, Lake Oswego, OR), 5.3. The magnetic sensors are a GMR configuration

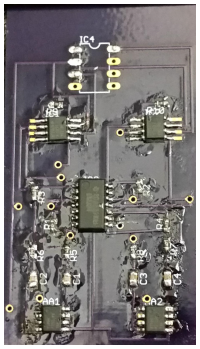

Figure 5.3: Circuit boards were custom fabricated to hold two sensors in line with wells of a 24-well plate. Three circuit boards were used to measure six tissues at a time.

that have a Wheatstone bridge configuration that resulted in a decrease in voltage when the magnetic field increased due to the movement of the flexible post. This results in a voltage changes on the order of several microvolts, which requires filtering and amplification to measure with standard data acquisition systems. Each measurement leg from the Wheatstone bridge was routed through high pass filters using operational amplifiers (LM324, Texas Instruments, Dallas, TX), Figure 5.4. The signal was further amplified using instrumentation amplifiers (INA 118, Texas Instruments). Signals from the circuit board were routed to a data acquisition system (USB6002, National Instruments, Austin, TX). Custom software for voltage acquisition during all experiments was writing using LabView. Separate programs were used for calibration experiments and biological experiments as a camera was unnecessary during biological experiments.

The high pass filter was designed with a cutoff frequency of 0.1 Hz. This eliminates

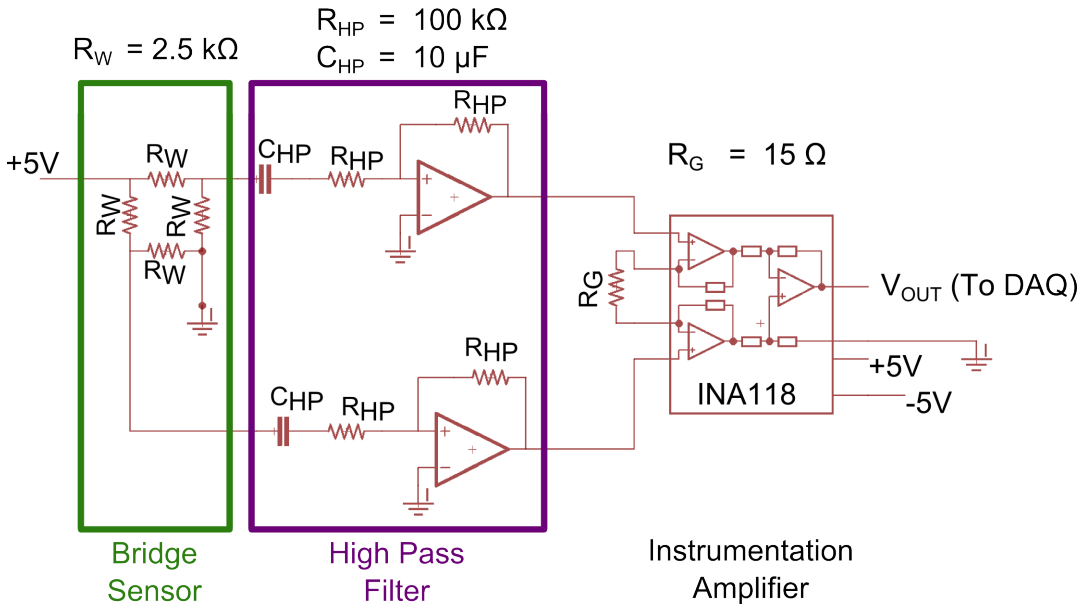

Figure 5.4: Signals from the Wheatstone bridge are filtered through a low pass filter, then a high pass filter before being amplified with an instrumentation amplifier and sent to a data acquisition system and read into LabView.

drift due to environmental conditions and allows the position to be easily read into a data acquisition program. Drift can come from magnetic field gradients in a room, or from other magnetic interferences. It is quite possible that the magnetic field will not be constant while this system is running, so calibrating the system effectively to eliminate effects due to drift is crucial.

5.2.3 Final Device Assembly

The printed circuit boards and a 24-well tissue culture plate were both held in place with a 3D printed holder to align the 24-well plates to the sensors for the optimum configuration, Figure 5.5. Additionally, a lid was fabricated to hold the tissues in position during experiments, and to keep them in close to the same location between each experiment. The lid was fabricated from a 3D printed mold. PDMS was poured into the mold and placed in

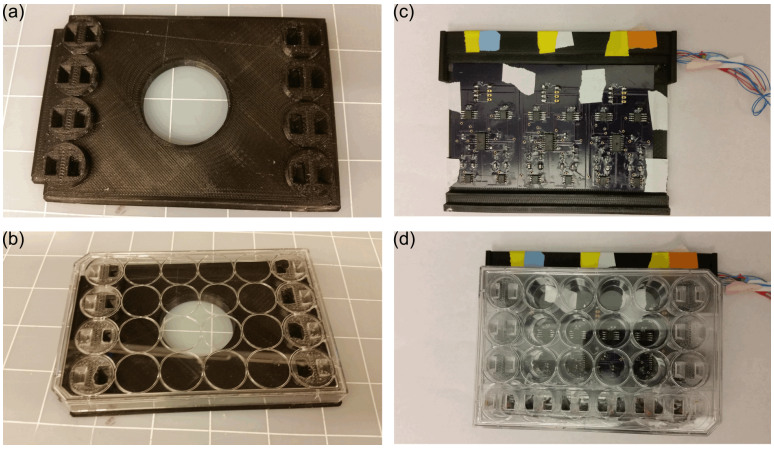

Figure 5.5: The final device assembly required all of the components to be held in place with precision. (a) A mold was 3D printed to form a lid by (b) adhering PDMS to a standard 24-well plate lid. The magnetic sensors were held in place with (c) a 3D printed structure, and (d) the 24-well plate fit over the sensors with the first row cut out for adding inhibitors to the tissues.

contact with a standard 24-well plate lid, and baked overnight at 40 °C, as higher temperatures caused warping of the 3D printed lid that was made out of PLA. The lid was further prepared for experiments by drilling through the first row to allow for the addition of drugs to the wells for real-time measurements. The final device had the magnetic posts held in place by a lid into a 24-well plate held in place above the sensors.

5.2.4 Magnetic Modeling and Optimization

The placement of the magnetic post will determine the change of magnetic field at the sensor. In order to determine the optimum placement of the sensor, both experimental and theoretical methods were used. Experimental methods showed that a location slightly behind the sensor produced the largest magnetic field changes, and were used to inform initial designs. I then created a model to better understand the effects of changing the relative position of the sensor and the post. This section will seek to determine tolerances necessary for accurate prediction of post deflection.

Due to the size of the magnet and the distance away from the sensor, the magnetic post can be modeled as a basic dipole. The magnet used in the posts has a strong magnetic field that is in the horizontal direction ($\boldsymbol{e_x}$), and weaker magnetic fields in the non-sensitive ($\boldsymbol{e_y}$) and vertical ($\boldsymbol{e_z}$) directions. This was verified experimentally, and determined to be $\boldsymbol{m} = 0.00075\boldsymbol{e_x} + 0.00015\boldsymbol{e_y} + 0.00015\boldsymbol{e_z}$ Am^2.

The expected motion of the post, as observed optically, is expected to have a maximum amplitude of 300 μm. I built a model to determine the magnetic field change as the magnet undergoes translation and rotation due to deflections up to 300 μm. This magnetic field change is determined by

$$\boldsymbol{B} = \frac{\mu_0}{4\pi}\left(3\frac{(\boldsymbol{m}\cdot\boldsymbol{r})\,\boldsymbol{r}}{r^5} - \frac{\boldsymbol{m}}{r^3}\right) \tag{5.1}$$

where $\boldsymbol{m}$ is the magnetic moment described above, and r is the distance from the current location of the magnet to the position in the plane of the sensor. The sensors was located 14 mm away from the post due to the physical constraints of the tissue culture dish. This, combined with the information above and resulted in an optimum position located a few millimeters ahead of the post (located at (0,0)), Figure 5.6(b). In addition to the model showing the optimum displacement, the model also showed that sensors would not have magnetic field changes due to posts in adjacent wells, Figure 5.6(a).

5.2.5 Magnetic Characterization

In order to test the model described in Equation 5.1 and Figure 5.6(b), I ran an experiment to show the variation in response due to locations of the magnetic post, Figure 5.7. As expected, an offset post produced increased magnetic field outputs (converted to voltages) compared with a post located directly above the sensor.

I precisely characterized the sensors used in the experiments using all of the equipment to be used in experiments. Five separate arrays of posts were used to characterize each sensor with 20-30 data points for each post. The magnet in the post was tracked using a metallurgical microscope (LV-100, Nikon), and camera. I used LabView software to acquire

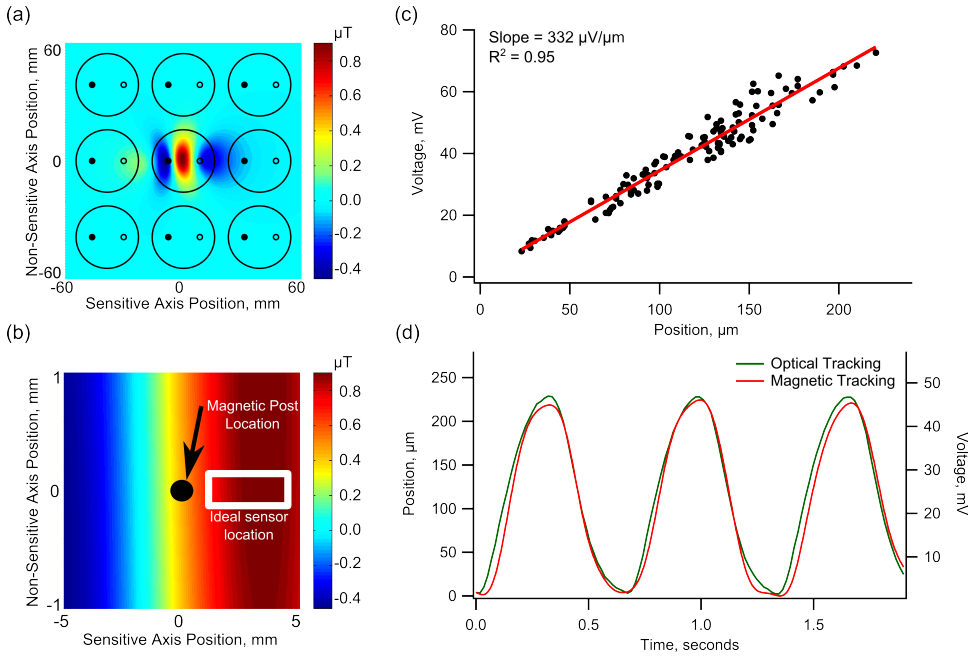

Figure 5.6: Magnetic modeling showed that (a) each post would not affect adjacent senors, and (b) the optimum location of the sensor is located 2-3 mm ahead of the post. Magnetic characterization showed (c) a linear trend of voltage to displacement, and (d) that the tissues had a similar waveform when paced at 1.5 Hz.

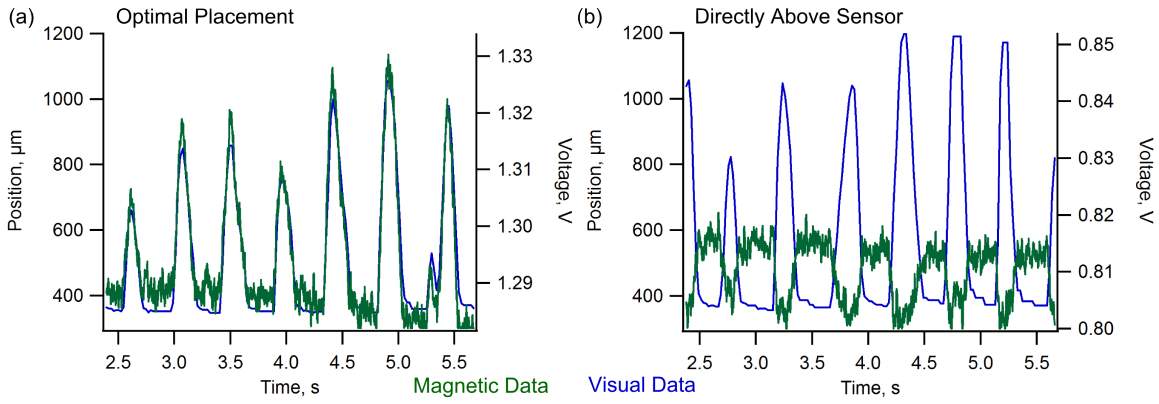

Figure 5.7: The location of the magnetic post determines the response of the sensor. (a) At a location slightly ahead of the sensor, the relationship between post and distance is 0.06 mV/μm. (b) At a location directly above the sensor, the response is reduced.

voltage data simultaneously with image data and observed a linear trend, Figure 5.6(c) and Figure 5.8. The sensors had varying calibration constants which is likely due to slight changes in the manufacturing of the sensors or position of the post relative to the sensors. Tissue forces were compared to baseline twitch forces in the experiments, and the trend for each sensor was linear ($R^2 > 0.9$). The linear trend allowed sensors to be used without additional modification.

In addition to variations between sensors, I observed that the sensitivity of the sensors was partially determined based on the orientation of the sensors relative to the Earth's magnetic field. The sensors had almost double the sensitivity when facing south compared with facing north. The baseline magnetic field is on the order of tens of microTeslas, which is also on the order of the Earth's magnetic field. I suspect that when aligned in a particular direction, the Earth's magnetic field is resulting in a net field close to zero, which is out of the linear range of the sensors. The experiments and characterizations performed in this thesis were all for sensors facing south.

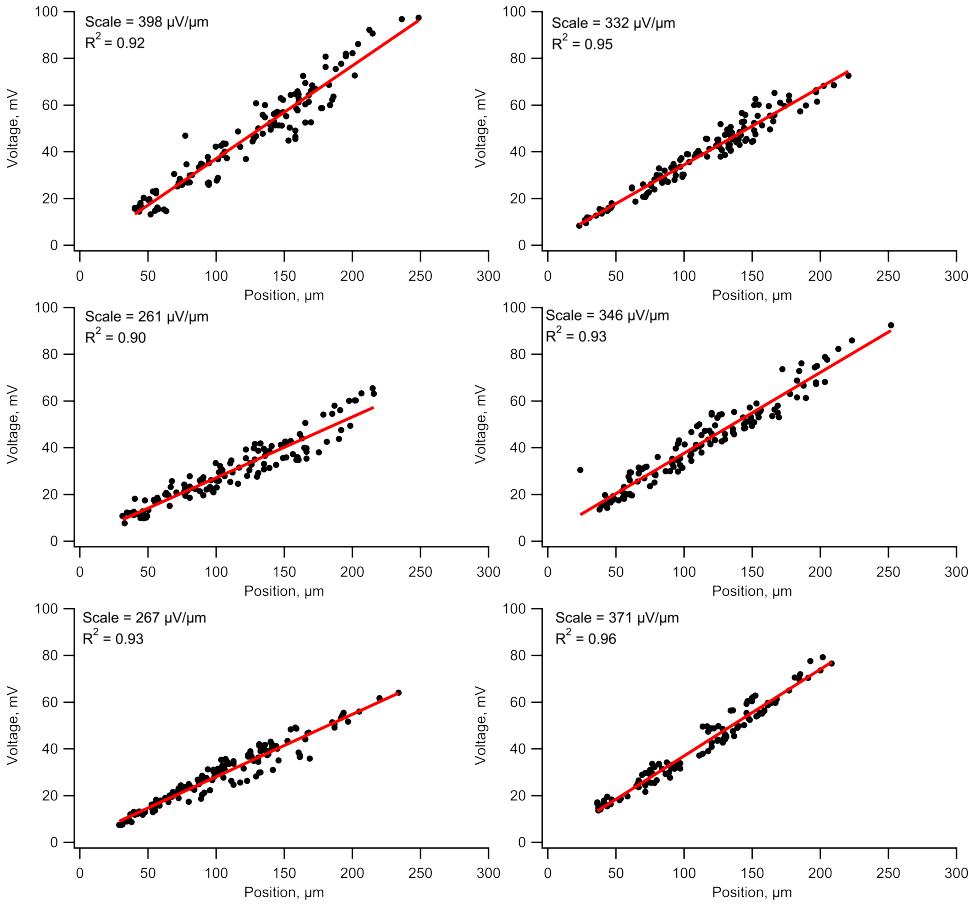

Figure 5.8: Magnetic sensors used in this experiment had slightly different calibration curves. The trend for all sensors was linear ($R^2 > 0.9$), and forces were compared to baseline for all tissues.

5.2.6 Engineered Heart Tissue Generation

Undifferentiated human induced pluripotent stem cells (hiPSCs) from the IMR90 line were maintained in mTeSR (Stemcell Technologies, Vancouver, BC, Canada) on tissue culture dishes coated with Matrigel (Corning, Corning, NY). An established protocol for directed differentiation was used to derive cardiomyocytes (CMs), as previously described [70]. Differentiation yielded greater than 80% cardiac troponin T^+ ($cTnT^+$) by flow cytometry. hiPSC-CMs were cast into EHTs on day 24 after induction of differentiation. EHTs were generated

following a similar protocol to Schaaf et al.[103], where each tissue was cast froma 100 μL fibrin gel solution containing $5{\cdot}10^5$ hiPSC-CMs and $5{\cdot}10^4$ supporting stromal cells (line HS-27a [96]). Agarose weells were formed by pouring a 2% agarose solution into a 24-well plate fitted with custom built spacers. A pair of posts was positioned into each agarose well, and the fibrin cell-gel solution was poured into the well to create an EHT bound onto the tips of each post. After 80 minutes of gelation the newly formed EHTs were transferred to a fresh 24-well plate. EHTS were maintained in a 24-well plate and were supplied with fresh RPMS media (11875-119, Invitrogen, Carlsbad, CA), supplemented with B-27 plus insulin (17504044, Life Technologies, Carlsbad, CA), and 5 mg/mL aminocaproic acid (A2504, Sigma-Aldrich, St. Louis, MO), three times per week. The EHTs were maintained in culture for two weeks before testing to allow for sufficient compaction and development of a stable beating pattern.

5.2.7 Pacing Experiments

In addition to characterizing the magnetic sensors by manually moving the posts with a linear micropositioner, the posts were also characterized by comparing the waveforms of engineered heart tissues paced under the gold standard of optical measurements, and with the new sensors. Pacing experiments were performed at 1.5 Hz and 2 Hz using both measurement platforms. Optical measurements were taken with an inverted microscope (Eclipse Ti, Nikon, Inc., Melville, NY) using a CCD camera (Clara, Andor, Belfast, Northern Ireland). Both optical and magnetic measurements were taken at 37 °C. Optical analysis provided the position of the post using custom Matlab image analysis software. In order to pace the tissues, carbon rods were used as electrodes and affixed with PDMS to the bottom of 24-well plate dishes. Platinum wire was wrapped around the electrodes and connected to a stimulator (S88X, Astro-Med, Inc., West Warwick, RI). Biphasic pacing was used with a pulse duration of 5 ms and amplitiude of 5 V for both conditions. The tissues were observed to follow the electrical stimulation and produced twitch forces with consistent amplitude during pacing. Pacing experiments were performed within a 10 minute window to ensure consistent response of the tissues. There was a strong correlation fo the pacing waveform,

Figure 5.6(d), and a linear relationship between forces produced at 1.5 Hz and 2 Hz.

5.3 Experimental Methods

The goal of the platform developed in this aim is to rapidly and easily measure engineered heart tissue forces. I have characterized the system extensively to show the linear response of the voltage with respect to the position of the post. The goal of the experiments are to investigate if the engineered heart tissues respond to pharmacological inhibitors in a similar fashion as adult tissues, and to demonstrate the potential of this device as a rapid drug screening tool.

5.3.1 Frequency and Force Analysis

Voltage outputs from the magnetic sensors were recorded using LabView and displayed on a screen in real-time during experiments. Further analysis was performed on all experiments to assess the frequency and magnitude of contractions over time. The data were filtered with a low-pass filter to remove measurement noise using an 8th order Butterworth filter with a cut-off frequency of 7 Hz. Only the peak-to-peak amplitudes were analyzed for force measurements, so low-frequency fluctuations in baseline readings were eliminated from the signal. In order to eliminate low-frequency baseline drifts, an exponential moving average filter with an exponent constant of 0.0001 was used.

After filtering the data, a custom peak finding program found the maxima and minima of the data with a minimum amplitude of 7 mV, or about 5-10% of the typical baseline motion. A cutoff of 7 mV was chosen based on the analysis of the signal produced by non-beating tissues. Below this threshold, there was an increased chance of registering a beat due to noise in the system. Furthermore, a tissue was determined to have stopped beating when the frequency of beats fell below 0.2 Hz.

Frequency was determined based on the time between maxima. The instantaneous magnitude was determined by subtracting the maximum from the adjacent minimum as long as the maximum and minimum were within two seconds of each other. In order to reduce errors

due to slight adjustment of the posts during fluid addition, a four-second window around each fluid addition time point was removed from the averages for both the frequency and magnitude measurements. This four-second window could be reduced in future experiments by using a non-magnetic pipette tip. Initial experiments were run with a metal pipette tip that caused significant alterations to the magnetic field observed by the sensors. The second round of experiments eliminated the magnetic tip; however, the analysis was kept the same for proper comparison of results. A combined ten-second moving average of the force and frequency was obtained for each of the four experiments.

5.3.2 Pharmacological Inhibitors

Two different inhibitors were chosen for demonstrating the utility of this device as a drug screening tool. The goal of choosing drugs was to choose one that would likely increase beating frequency and potentially beating force, and to chose another drug that would likely lower beating force and alter beating frequency.

In order to increase beating frequency, isoproterenol hydrochloride (CAS 5984-95-2, Sigma-Aldrich, St. Louis, MO) was used with three different concentrations, 50 nM, 500 nM, and 50 μM. Isoproterenol is a β-adrenergic agonist [32]. Isoproterenol has previously been shown to increase beating frequency and have a positive inotropic response in the adult heart, although it has been shown that the inotropic response is not present in young heart tissues.

In order to decrease tissue forces, verapamil hydrochloride (CAS 152-11-4, Tocris Bioscience, Bristol, UK) was used with three different concentrations, 500 nM, 5 μM, and 50 μM. Verapamil is a calcium channel blocker [114]. Verapamil has previously been shown to alter beating frequency, and to significantly decrease tissue forces in both adult and young tissues.

For all pharmacological inhibition experiments, a batch mixture of 2.5 mM of each drug in DI water was passed through a sterile filter and portioned into the appropriate dilution based on the final concentration. The media volume in each well during the experiment was

2.5 mL, and 50 μL of the drug solution was added to yield the desired final concentration of the drug in the complete media. The control case had no treatment added to the media during the experiment, and the sham control had 50 μL of sterile DI water added to the media. All experiments were performed at 37 °C. After the responses to the drugs were observed, the drugs were washed out with new media, and tissues were allowed to reset for two days before undergoing further treatments.

5.4 Experimental Results

The system was successfully tested as a drug screening tool, and was capable of measuring the twitch forces over time for six different tissues. Typically, force measurements of tissues is performed optically, and the experimenter can qualitatively understand the results of experiments for tissues; however, the this system allowed the experimenters to quantitatively watch in real time as the twitch forces and frequencies of tissues changed.

5.4.1 Simultaneous Measurements for Drug Screening

In addition to gathering simultaneous data and significantly reducing the amount of time required to run an experiment, this system also allowed for the generation of large sets of data without generating large files typically associated with image capture. File sizes for approximately seven minutes worth of data for six tissues was on the order of megabytes, while it would be on the order of gigabytes for typical image analysis systems. Capturing large amounts of data and reducing the time required by the researchers, allowed this system to observe forces continuously rather than at discrete time points, Figure 5.9. The large amount of data aided in understanding how the drugs affected the tissues and can help in future experiments to explore transient effects of drugs that may be missed with conventional tissues analysis methods.

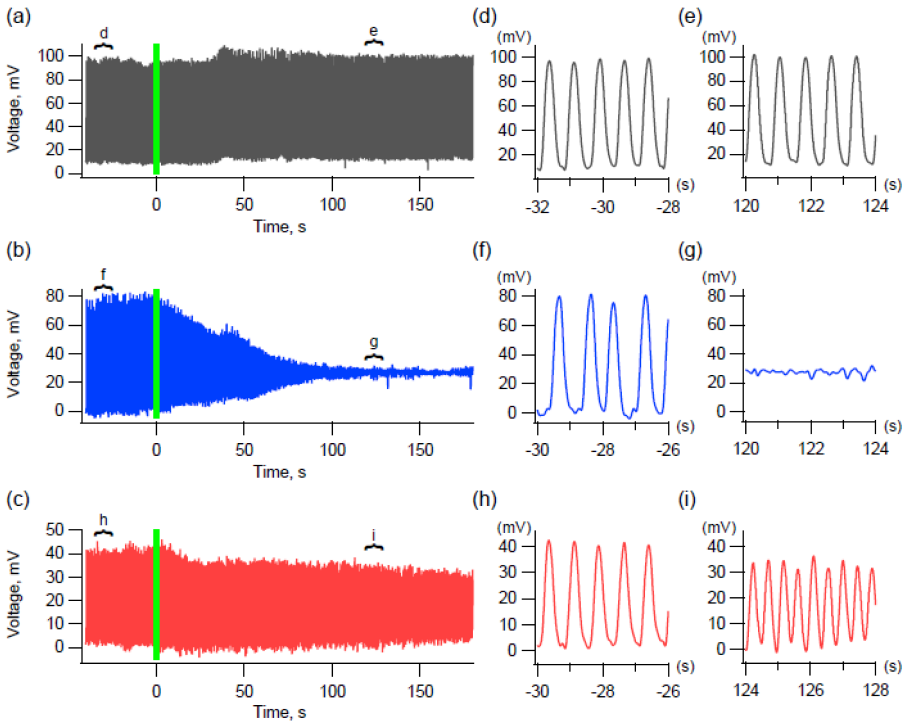

Figure 5.9: Real-time analysis of tissue forces in response to pharmacological compounds. (a) Sham control has a similar force and frequency profile over time. Tissues treated with (b) 5 μM of verapamil have a significantly reduced force over time, while tissues treated with (c) 500 nM of isoproterenol have a reduced force and significantly increased frequency over time. (e,f,h) Tissues have similar frequencies and twitch force magnitudes before adding pharmacological compounds. (e) Sham control continues at the same force and frequency, while tissues treated with (g) verapamil eventually stop beating, and tissues treated with (i) isoproterenol have nearly double the beating frequency and a slightly reduced force.

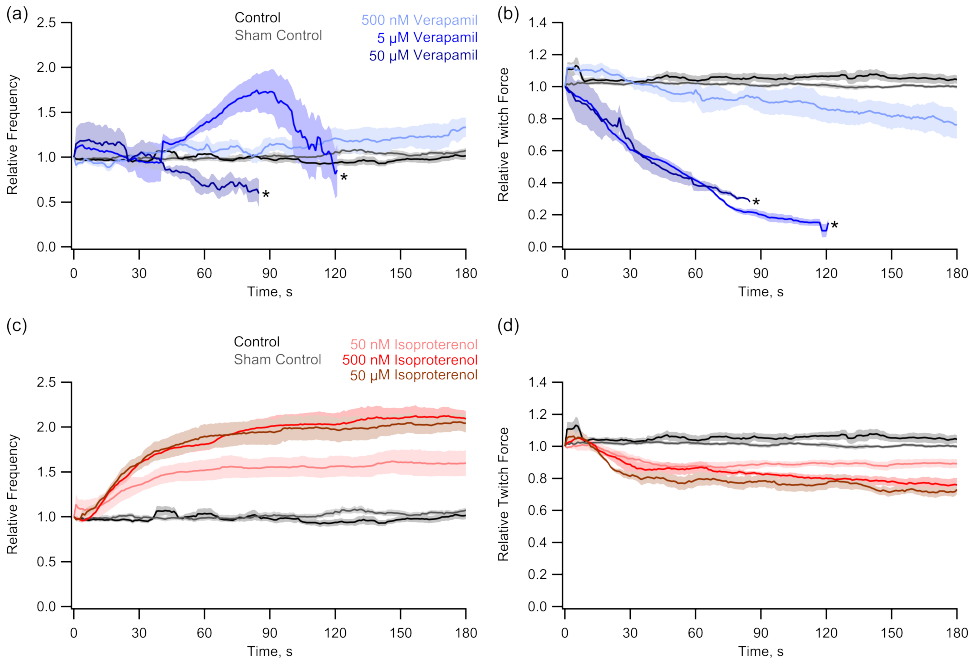

Figure 5.10: Combined data from multiple experiments with verapamil and isoproterenol. (a) Frequency of contractions increases with verapamil addition while (b) magnetide of twitch forces decreases (* indicate when the signal for more than half of the data feel below 7 mV and 0.2 Hz). Isoproterenol increases the (c) frequency of tissue contractions, and slightly lowers the (d) twitch forces of tissue conractions.

5.4.2 Pharmacological Inhibitors

In order to demonstrate the utility of this device for drug screening applications, three concentrations of each of verapamil and isoproterenol were used to manipulate tissue twitch force and beating frequency. All of the tissues were measured for one minute before adding drugs to the system, and the force and frequency of contractions was monitored for at least three minutes afer the addition of each drug. Each study generated complete waveforms of the tissue contractions over the course of three minutes. Two controls were used, one with no fluid additions, and one where water was added with no drugs (sham control). In both cases, the spontaneous beating of the tissues had little variation throughout the experiments, Figure 5.10.

Verapamil had a large effect on both the beating frequency and the force generation of the tissue constructs, Figure 5.10. Increasing concentrations of verapamil caused lower forces and lower frequencies. The effect of verapamil on force was nearly immediate, although there typically was an initial increase in beating frequency before the tissue ceased beating. A low dosage of verapamil caused a slight increase of the beating frequency from the baseline frequency. There were some fairly large variations in the verapamil beating frequency and force magnitude, some of which can be attributed to the choice of a 7 mV cut-off for the force generation. This was due to the amount of noise in the system.

As expected, isoproterenol increased the beating frequency as the concentration was increased. The increase in beating frequency started quickly, and appeared to level off within two minutes after adding the drug, Figure 5.10. A decrease in contractile force was observed with increasing concentrations of isoproterenol. The decrease in force is typical for immature myocardium, which has not yet expressed phospholamban, the Ca^{2+}-regulatory protein that is targeted by beta-adrenergic stimulation [104, 91, 138].

After completing the tests, tissues were returned to fresh media, and the force and frequency response returned to similar levels as before alterations with the drugs. Tissues that had been exposed to high concentrations of verapamil were found to beat faster and likely stronger than other tissues, and these tissues were not used in subsequent experiments.

These results show that this system is sufficiently sensitive to changes in twitch force and frequency to measure the effects of drugs and could be used in a drug screening assay.

5.5 Discussion

Efficient and parallel screening of pharmacological compounds in a model human engineered heart tissue system is desired for drug discovery. Such a platform would also be useful to monitor EHT force production for therapeutic applications. Several tools have been developed for monitoring the beating frequency and twitch force production of EHTs, but thus far, none have produced simple measurements to enable real-time contractile information. Previous devices have looked into electrical measurements of force using PDMS devices [87],

and other devices have embedded magnetic material into PDMS cantilever devices [35, 113]. Few devices have used magnetic field changes to measure forces [55], and I believe that this is the first device to measure tissue forces using embedded magnets in a PDMS device. This system is advantageous compared with previous systems as it is able to continuously monitor the forces of several tissue constructs throughout an experiment, and ease the burden of imaging for the researcher. Real-time monitoring can ensure that tissues are behaving properly, and it can aid in performing massively parallel experiments. I built a system that was limited to six simultaneous measurements, but as I showed in Figure 5.6(a), the system has the potential to be expanded to simultaneously monitor an entire 24-well plate. Even with only six simultaneous measurements, four arrays of posts were tested with two controls and four measurements in rapid succession without the need to position the posts or find the posts in a microscope objective. This rapid screening can be useful for high-throughput, low-cost drug screening applications.

In order to demonstrate the feasibility of my device, I tested two different drugs to alter the frequency and force of tissue contractions. I chose to use verapamil, a calcium channel blocker, with an expected result of lowering twitch force and frequency, and I chose to use isoproterenol, a β-adrenergic agonist, with the expected result of increasing beating frequency. I found that verapamil lowered twitch force, and it even temporarily stopped the tissue construct from beating. Furthermore, I found that the frequency of contractions increased before the contractions ceased to beat with enough forces for higher concentrations of verapamil. For a low concentration of verapamil, I found that the frequency increased while the twitch force magnitude had a slight decrease. The increased frequency and lowered force response of EHTs to verapamil has been seen before [81, 57, 46], and I have shown a way to measure it *in situ*.

Isoproterenol increased the frequency along the same order as what has previously been observed by other research groups [53, 65]. The response was a steady increase over the course of approximately 90 seconds. After 90 seconds, the response leveled off ot the new frequency and twitch forces. Somewhat surprisingly, the force of contractions decreased, however, it has

been shown that EHTs derived from induced pluripotent stem cells have different responses than that of native heart tissues [134]. The structure of induced pluripotent stem cells used in these experiments is likely much more immature than adult cardiomyocytes [138], and it has been shown that immature cardiomyocyte tissues do not produce an inotropic response to isoproterenol [91].

I used this system to simultaneously measure the response of six different tissues at a time, and four replicates were easily measured in the time it took the tissues to respond to the forces. Little adjustment or calibration was needed once hte device was built, and post-processing analysis could easily be integratedinto the data acquisition program to produce immediate results from experiments using this system. Furthermore, the tissue constructs and mult-well dishes are all disposable, while the sensors and electronics are free from contacting the biological media, and thus do not require sterilization between each use. This enables testing of devices over time for studies that have slower-acting drugs or to monitor the twitch forces of tissues in an incubator over time. This system can be used to either rapidly screen for a number of different drugs or to monitor the contractile forces of EHTs being developed for potential therapeutic replacements.

In order for the system to be expanded for use in drug screening systems, some aspects of the current device would need improvement. Currently, the system that I built is limited to measuring twitch forces, and it has some variance in the sensing capability of each sensor. A system could be designed to measure both passive and active forces of cardiomyocyte tissues, and that would result in a more complete understanding of the function of the tissues. In order to accomplish that goal, the system could be altered to change the filtering design, and placement of the sensors could be further improved to reduce variance between each sensor. These improvements can be engineered to provide more information about the EHTs and provide an inexpensive and autonomous drug screening platform.

5.6 Conclusions

I have successfully built and demonstrated the use of a magnetic sensing method for measuring forces of engineered heart tissues. The system had a linear response to tissue forces and was demonstrated with three doses of isoproterenol and verapamil. The device shows promise for use in rapid screening of drugs and can be used for a variety of different tissue configurations.

Chapter 6

FINAL CONCLUSIONS AND FUTURE DIRECTIONS

I have presented three devices and methods for studying the viscoelasticity of biomaterials and myocardial forces. The results of the experiments showed that the devices can be used in microenvironments for characterizing and understanding the materials. In this chapter, I will review the accomplishments of the three aims and discuss what I believe are potentials for future work related to each of the devices and methods presented in this thesis.

6.1 Summary of Results

6.1.1 Aim 1

I successfully built a new model device for measuring the viscoelasticity of biomaterials using a magnetically-enhanced PDMS post. The device was used to measure the viscoelasticity of collagen gels, and it could be integrated into disposable devices for measuring viscoelasticity of other biomaterials. The device has a small size and is inexpensive to build and can produce significant motions.

6.1.2 Aim 2

I miniaturized the magnetic post system for use in a microfluidic channel that could be used with blood to form shear-developed platelet clots. This system was capable of forming platelet plugs as well as measuring the elastic modulus of the plugs and collagen gels formed in the channels. It is now possible to perform *in situ* measurements of platelet clots form in microfluidic channels. I demonstrated the ability to measure the stiffness and showed that the measured stiffnesses of clots and collagen gels are greater than typical errors due to post

position and force generation. The results showed that shear-developed platelet clots had a stiffness on order with previous results.

6.1.3 Aim 3

I developed, fabricated, characterized, and used a new device for measuring twitch forces of human engineered heart tissues. The device was extensively characterized to show that the response of the sensors is linear with the force applied to the sensors. Magnetic sensors were not affected by pacing experiments or the presence of the engineered heart tissues. Drugs could be added to media while engineered heart tissues were beating, and the response was monitored in real time. Forces and frequency were tracked over time and provided input about the effects of the drugs and the maturity of the engineered heart tissues.

The main advantage of aim 3 was a significant reduction in the time to generate and understand results related to adding drugs. Researchers were able to see results immediately, and there was a significant reduction in storage space for the experimental results. This device provided a simple and rapid way to assess both force and frequency performance of engineered heart tissues.

6.2 Broader Impacts and Future Directions

The devices and experiments that I ran investigated biomaterials and myocardial forces using new techniques that either provided new capabilities or were easier to use and inexpensive compared with current techniques. The results showed promise for these tools to be continued for use in studying biomaterials and myocardial forces.

6.2.1 Aim 1

The goals of my first aim were to develop an understanding of a magnetic post system and how it performs in a viscoelastic environment. I think the device could continue to be extended by producing more force on the post, and tracking the post magnetically. The use

of a magnetic tracking method would enable disposable and remote tools that do not require microscopes and image analysis software. Measuring the post motion magnetically would be challenging due to the impact of the external magnetic field. External fields would require some form of compensation to fully use the device without a microscope.

6.2.2 Aim 2

I miniaturized the device from aim 1 and characterized it for use in measuring platelet clot elasticity. This device provides benefits of *in situ* measurements of platelet clots, and can be used to study the effects of inhibitors on clot stiffness and to add drugs after plugs have formed to further alter clot stiffness. This information can provide more insight into how the biological cues are converted into mechanical changes in clots, and that can change how trauma and platelet treatments are administered in the future.

Now that clot elasticity can be measured *in situ* for shear-developed platelet clots, there are many experiments that can be run to understand the effects of various antagonists on the elasticity of platelet clots. Additionally, the device can be modified, as described in Chapter 3 to measure viscoelasticity in addition to elasticity. Measurements could be made while shear-developed clots are forming, or in clots developed with much lower shear rates. The magnetic posts can be used in many ways to understand shear-developed platelet clot formation and function.

Platelet function, especially mechanical function, is vital to proper recovery from trauma, and understanding how platelets form clots, and the mechanical properties of those clots is vital to understanding hemostasis and treating patients with abnormal conditions. This device helps to provide more insight and encourage new means of discovering platelet function.

6.2.3 Aim 3

The sensors for measuring myocardial forces can be expanded for use in a full 24-well plate. The analysis I showed in Chapter 5 indicates that it is merely a design problem for aligning the sensors on breadboards in the dish. A full 24-well plate connected to continual analysis

can allow for rapid and easy drug screening. Additionally, expanding the sensing algorithm and filtering to measure both passive and active myocardial tissues can also provide more information to expand this device beyond the 24-well plate and to be used in drug screening applications.

In addition to drug screening applications, the measurement device could be coupled with force actuation to apply forces to engineered heart tissues using a feedback loop that allows for the mimicking of loading forces in the heart. This method would allow for new understanding of how to grow tissues for potential replacement therapies. Heart cells do not reproduce as humans age, leaving the need for alternative replacement therapies, but current replacement methods do not produce strong enough tissues on the order of adult heart tissues. A new method to grow tissues could provide a way to take immature induced pluripotent stem cells, differentiate them into heart cells, then create strong enough tissues through a "workout" system using a feedback loop until the tissues are strong enough for a replacement therapy.

Heart disease is the leading cause of death in the United States, and this device provides methods to screen for drugs that can improve heart health as well as a platform for a potential bioreactor to improve the strength of engineered heart tissues for replacement therapy.

6.3 Conclusions

Magnetic devices provide means to apply forces at a distance for a greater understanding of biomaterials. Additionally, magnetic devices can be used for significantly lowering researcher time when measuring forces and devices. I have developed, characterized, and used several devices for measuring properties of biomaterials and forces of myocardial tissues, and I hope that some of the work forms a basis for future inventions and findings.

BIBLIOGRAPHY

[1] Collagen i, rat tail, 2014.

[2] Kweku A Addae-Mensah and John P Wikswo. Measurement techniques for cellular biomechanics in vitro. *Experimental biology and medicine (Maywood, N.J.)*, 233(7):792–809, July 2008.

[3] Ashutosh Agarwal, Josue Adrian Goss, Alexander Cho, Megan Laura McCain, and Kevin Kit Parker. Microfluidic heart on a chip for higher throughput pharmacological studies. *Lab on a Chip*, 13(18):3599–3608, 2013.

[4] J. Alcaraz, L. Buscemi, M. Grabulosa, X. Trepat, B. Fabry, R. Farre, and D. Navajas. Microrheology of human lung epithelial cells measured by atomic force microscopy. *Biophysical Journal*, 84(3):2071–2079, 2003.

[5] Aereas Aung, Ivneet Singh Bhullar, Jomkuan Theprungsirikul, Shruti Krishna Davey, Han Liang Lim, Yu-Jui Chiu, Xuanyi Ma, Sukriti Dewan, Yu-Hwa Lo, and Andrew McCulloch. 3d cardiac tissues within a microfluidic device with real-time contractile stress readout. *Lab on a Chip*, 16(1):153–162, 2016.

[6] L Badimon, V Turitto, JA Rosemark, JJ Badimon, and V Fuster. Characterization of a tubular flow chamber for studying platelet interaction with biologic and prosthetic materials: deposition of indium 111-labeled platelets on collagen, subendothelium, and expanded polytetrafluoroethylene. *The Journal of laboratory and clinical medicine*, 110(6):706–718, 1987.

[7] Mario Norberto Baibich, Jean Marc Broto, Albert Fert, F Nguyen Van Dau, Frdric Petroff, P Etienne, G Creuzet, A Friederich, and J Chazelas. Giant magnetoresistance of (001) fe/(001) cr magnetic superlattices. *Physical review letters*, 61(21):2472–, 1988.

[8] Marsha D. Bale, Michael F. Mller, and John D. Ferry. Rheological studies of creep and creep recovery of unligated fibrin clots: Comparison of clots prepared with thrombin and ancrod. *Biopolymers*, 24(3):461–482, March 1985.

[9] Nathan Banka and Santosh Devasia. Nonlinear models for optimal placement of magnetically-actuated cilium. In *ASME 2013 Dynamic Systems and Control Conference*, pages V003T42A003–V003T42A003. American Society of Mechanical Engineers, 2013.

[10] A. R. Bausch, U. Hellerer, M. Essler, M. Aepfelbacher, and E. Sackmann. Rapid stiffening of integrin receptor-actin linkages in endothelial cells stimulated with thrombin: A magnetic bead microrheology study. *Biophysical Journal*, 80(6):2649–2657, 2001.

[11] Andreas R Bausch, Florian Ziemann, Alexei A Boulbitch, Ken Jacobson, and Erich Sackmann. Local measurements of viscoelastic parameters of adherent cell surfaces by magnetic bead microrheometry. *Biophysical journal*, 75(4):2038–2049, 1998.

[12] Haym Benaroya. *Mechanical vibration : analysis, uncertainties, and control*. Prentice Hall, Upper Saddle River, N.J., 1998.

[13] Anne K Bentley, Mohammed Farhoud, Arthur B Ellis, Anne-Marie L Nickel, George C Lisensky, and Wendy C Crone. Template synthesis and magnetic manipulation of nickel nanowires. *Journal of chemical education*, 82(5):765–, 2005.

[14] Kevin S Bielawski and Nathan J Sniadecki. Micropost methods for cell biomechanics of the cardiovascular system. In *Cells, Forces, and the Microenvironment*, pages 291–310–. Pan Stanford, February 2015.

[15] Kevin S Bielawski and Nathan J Sniadecki. A magnetic post approach for measuring the viscoelasticity of biomaterials. 25(1):153–159, Feb 2016. ©2016 IEEE. Reprinted, with permission.

[16] Dimitar Borissov, Sonnur Isik-Uppenkamp, and Michael Rohwerder. Fabrication of iron nanowire arrays by electrodeposition into porous alumina. *The Journal of Physical Chemistry C*, 113(8):3133–3138, 2009.

[17] Thomas Boudou, Wesley R Legant, Anbin Mu, Michael A Borochin, Nimalan Thavandiran, Milica Radisic, Peter W Zandstra, Jonathan A Epstein, Kenneth B Margulies, and Christopher S Chen. A microfabricated platform to measure and manipulate the mechanics of engineered cardiac microtissues. *Tissue Engineering Part A*, 18(9-10):910–919, 2011.

[18] R. M. (Richard M.) Bozorth. *Ferromagnetism*. Piscataway, NJ : IEEE Press, Piscataway, NJ, 1978.

[19] Katleen Broos, Hendrik B. Feys, Simon F. De Meyer, Karen Vanhoorelbeke, and Hans Deckmyn. Platelets at work in primary hemostasis. *Blood Reviews*, 25(4):155–167, July 2011.

[20] L. Chevry, N. K. Sampathkumar, A. Cebers, and J. F. Berret. Magnetic wire-based sensors for the microrheology of complex fluids. *Physical Review E*, 88(6):062306–062306, 2013.

[21] KM Chui, AO Adeyeye, and Mo-Huang Li. Detection of a single magnetic dot using a planar hall sensor. *Journal of Magnetism and Magnetic Materials*, 310(2):e992–e993, 2007.

[22] Koo-Hyun Chung, Kiran Bhadriraju, Tighe A. Spurlin, Robert F. Cook, and Anne L. Plant. Nanomechanical properties of thin films of type i collagen fibrils. *Langmuir*, 26(5):3629–3636, March 2010.

[23] Pietro Cicuta and Athene M. Donald. Microrheology: a review of the method and applications. *Soft Matter*, 3:1449–1455, 2007.

[24] JMD Coey. Permanent magnets: Plugging the gap. *Scripta Materialia*, 67(6):524–529, 2012.

[25] Michael Coey. *Magnetism and Magnetic Materials*. Cambridge : Cambridge University Press, Leiden, 2010.

[26] Charles M. Cuerrier and Andrew E. Pelling, editors. *Cells, forces, and the microenvironment*. Singapore : Pan Stanford Publishing, 2015.

[27] Luis Teodoro Da Luz, Bartolomeu Nascimento, Ajith Kumar Shankarakutty, Sandro Rizoli, and Neill KJ Adhikari. Effect of thromboelastography (teg) and rotational thromboelastometry (rotem) on diagnosis of coagulopathy, transfusion guidance and mortality in trauma: descriptive systematic review. *Critical Care*, 18(5):518–, August 2014.

[28] Earl W Davie, Kazuo Fujikawa, and Walter Kisiel. The coagulation cascade: initiation, maintenance, and regulation. *Biochemistry*, 30(43):10363–10370, 1991.

[29] Micah Dembo and Yu-Li Wang. Stresses at the cell-to-substrate interface during locomotion of fibroblasts. *Biophysical journal*, 76(4):2307–2316, 1999.

[30] Thomas Ebinger. Concerning hnecke p, klouche m: Thrombelastography today: Practicability and analytical power. transfus med hemother 2007;34:421428. *Transfusion Medicine and Hemotherapy*, 35(4):324–326, July 2008.

[31] Alexandra Eder, Ingra Vollert, Arne Hansen, and Thomas Eschenhagen. Human engineered heart tissue as a model system for drug testing. *Advanced Drug Delivery Reviews*, page in press, 2015.

[32] Masao Endoh. The effects of various drugs on the myocardial inotropic response. *General Pharmacology: The Vascular System*, 26(1):1–31, 1995.

[33] T Eschenhagen, C Fink, U Remmers, H Scholz, J Wattchow, J Weil, W Zimmermann, HH Dohmen, H Schfer, and N Bishopric. Three-dimensional reconstitution of embryonic cardiomyocytes in a collagen matrix: a new heart muscle model system. *The FASEB Journal*, 11(8):683–694, 1997.

[34] Thomas Eschenhagen, Michael Didi, Jrgen Heubach, Ursula Ravens, and Wolfram-Hubertus Zimmermann. Cardiac tissue engineering. *Transplant immunology*, 9(2):315–321, 2002.

[35] B. A. Evans, A. R. Shields, R. Lloyd Carroll, S. Washburn, M. R. Falvo, and R. Superfine. Magnetically actuated nanorod arrays as biomimetic cilia. *Nano Letters*, 7(5):1428–1434, 2007.

[36] M. C. Evans and V. H. Barocas. The modulus of fibroblast-populated collagen gels is not determined by final collagen and cell concentration: Experiments and an inclusion-based model. *Journal of Biomechanical Engineering-Transactions of the Asme*, 131(10):101014, 2009.

[37] Shirin Feghhi and Nathan J Sniadecki. Mechanobiology of platelets: Techniques to study the role of fluid flow and platelet retraction forces at the micro- and nano-scale. *International Journal of Molecular Sciences*, 12(12):9009–9030, November 2011.

[38] HA Ferreira, DL Graham, PP Freitas, and JMS Cabral. Biodetection using magnetically labeled biomolecules and arrays of spin valve sensors. *Journal of Applied Physics*, 93(10):7281–7286, 2003.

[39] A Fert, P Grnberg, A Barthelemy, F Petroff, and W Zinn. Layered magnetic structures: interlayer exchange coupling and giant magnetoresistance. *Journal of Magnetism and Magnetic Materials*, 140:1–8, 1995.

[40] Mathew H Flamm and SL Diamond. Multiscale systems biology and physics of thrombosis under flow. *Annals of biomedical engineering*, 40(11):2355–2364, 2012.

[41] Albert Folch and Mehmet Toner. Cellular micropatterns on biocompatible materials. *Biotechnology Progress*, 14(3):388–392, 1998.

[42] PP Freitas, R Ferreira, S Cardoso, and F Cardoso. Magnetoresistive sensors. *Journal of Physics: Condensed Matter*, 19(16):165221–, 2007.

[43] D. Fuard, T. Tzvetkova-Chevolleau, S. Decossas, P. Tracqui, and P. Schiavone. Optimization of poly-di-methyl-siloxane (pdms) substrates for studying cellular adhesion and motility. *Microelectron. Eng.*, 85(5-6):1289–1293, May 2008.

[44] Julie R Fuchs, Boris A Nasseri, and Joseph P Vacanti. Tissue engineering: a 21st century solution to surgical reconstruction. *The Annals of thoracic surgery*, 72(2):577–591, 2001.

[45] Peter Galie, Fitzroy J Byfield, Christopher S Chen, J Yasha Kresh, and Paul Janmey. Mechanically stimulated contraction of engineered cardiac constructs using a microcantilever. *Biomedical Engineering, IEEE Transactions on*, 62(2):438–442, 2015.

[46] Kristin H Gilchrist, Gregory F Lewis, Elaine A Gay, Katelyn L Sellgren, and Sonia Grego. High-throughput cardiac safety evaluation and multi-parameter arrhythmia profiling of cardiomyocytes using microelectrode arrays. *Toxicology and applied pharmacology*, 288(2):249–257, 2015.

[47] Bernhard Gleich and Jrgen Weizenecker. Tomographic imaging using the nonlinear response of magnetic particles. *Nature*, 435(7046):1214–1217, 2005.

[48] Shinya Goto, Yasuo Ikeda, Enrique Saldvar, and Zaverio M Ruggeri. Distinct mechanisms of platelet aggregation as a consequence of different shearing flow conditions. *Journal of Clinical Investigation*, 101(2):479–, 1998.

[49] W. P. Graebel. *Advanced fluid mechanics*. Academic Press, Burlington, MA, 2007.

[50] V Haehnel, S Fhler, P Schaaf, M Miglierini, C Mickel, L Schultz, and H Schlrb. Towards smooth and pure iron nanowires grown by electrodeposition in self-organized alumina membranes. *Acta Materialia*, 58(7):2330–2337, 2010.

[51] Sangyoon J Han, Kevin S Bielawski, Lucas H Ting, Marita L Rodriguez, and Nathan J Sniadecki. Decoupling substrate stiffness, spread area, and micropost density: a close spatial relationship between traction forces and focal adhesions. *Biophysical journal*, 103(4):640–648, 2012.

[52] Albert K Harris, Patricia Wild, and David Stopak. Silicone rubber substrata: a new wrinkle in the study of cell locomotion. *Science*, 208(4440):177–179, 1980.

[53] Tomohiro Hayakawa, Takeshi Kunihiro, Tomoko Ando, Seiji Kobayashi, Eriko Matsui, Hiroaki Yada, Yasunari Kanda, Junko Kurokawa, and Tetsushi Furukawa. Image-based evaluation of contractionrelaxation kinetics of human-induced pluripotent stem cell-derived cardiomyocytes: Correlation and complementarity with extracellular electrophysiology. *Journal of molecular and cellular cardiology*, 77:178–191, 2014.

[54] E. J. Hearn. Mechanics of materials, volume 1 - an introduction to the mechanics of elastic and plastic deformation of solids and structural materials (3rd edition), 1997.

[55] Matthew Hein, Mazin M Maqableh, Michael J Delahunt, Mark Tondra, Alison B Flatau, Carol K Shield, and Bethanie JH Stadler. Fabrication of bioinspired inorganic nanocilia sensors. *Magnetics, IEEE Transactions on*, 49(1):191–196, 2013.

[56] M. Hetnyi. *Beams on elastic foundation; theory with applications in the fields of civil and mechanical engineering*. University of Michigan Press, Ann Arbor, 1946.

[57] Herbert M Himmel. Drug-induced functional cardiotoxicity screening in stem cell-derived human and mouse cardiomyocytes: effects of reference compounds. *Journal of pharmacological and toxicological methods*, 68(1):97–111, 2013.

[58] Marc N Hirt, Arne Hansen, and Thomas Eschenhagen. Cardiac tissue engineering state of the art. *Circulation research*, 114(2):354–367, 2014.

[59] G. N. B. Jackson, K. J. Ashpole, and S. M. Yentis. The teg vs the rotem thromboelastography/thromboelastometry systems. *Anaesthesia*, 64(2):212–215, February 2009.

[60] Shaun P Jackson. The growing complexity of platelet aggregation. *Blood*, 109(12):5087–5095, 2007.

[61] David Jiles. *Introduction to magnetism and magnetic materials*. Chapman and Hall, London; New York, 1991.

[62] Kerstin Jurk and Beate E Kehrel. Platelets: physiology and biochemistry. In *Seminars in thrombosis and hemostasis*, volume 31, pages 381–392, 2004.

[63] B Kalska-Szostko, E Brancewicz, P Mazalski, J Sveklo, W Olszewski, K Szymanski, and A Sidor. Electrochemical deposition of nanowires in porous alumina. *Acta Physica Polonica-Series A General Physics*, 115(2):542–, 2009.

[64] Makoto Kawamori, Shunsuke Yagi, and Eiichiro Matsubara. Formation of nickel nanowires via electroless deposition under a magnetic field. *Journal of The Electrochemical Society*, 158(8):E79–E83, 2011.

[65] Jong J Kim, Lei Yang, Bo Lin, Xiaodong Zhu, Bin Sun, Aaron D Kaplan, Glenna CL Bett, Randall L Rasmusson, Barry London, and Guy Salama. Mechanism of automaticity in cardiomyocytes derived from human induced pluripotent stem cells. *Journal of molecular and cellular cardiology*, 81:81–93, 2015.

[66] Timothy R Kline, Mingliang Tian, Jinguo Wang, Ayusman Sen, Moses WH Chan, and Thomas E Mallouk. Template-grown metal nanowires. *Inorganic chemistry*, 45(19):7555–7565, 2006.

[67] David M. Knapp, Victor H. Barocas, Alice G. Moon, Kyeongah Yoo, Linda R. Petzold, and Robert T. Tranquillo. Rheology of reconstituted type i collagen gel in confined compression. *Journal of Rheology*, 41(5):971–993, 1997.

[68] T Kofidis, P Akhyari, J Boublik, P Theodorou, U Martin, A Ruhparwar, S Fischer, T Eschenhagen, HP Kubis, and T Kraft. In vitro engineering of heart muscle: artificial myocardial tissue. *The Journal of Thoracic and Cardiovascular Surgery*, 124(1):63–69, 2002.

[69] S. Krenk. *Mechanics and analysis of beams, columns and cables : a modern introduction to the classic theories*. Springer, Berlin; New York, 2001.

[70] Michael A Laflamme, Kent Y Chen, Anna V Naumova, Veronica Muskheli, James A Fugate, Sarah K Dupras, Hans Reinecke, Chunhui Xu, Mohammad Hassanipour, and Shailaja Police. Cardiomyocytes derived from human embryonic stem cells in pro-survival factors enhance function of infarcted rat hearts. *Nature biotechnology*, 25(9):1015–1024, 2007.

[71] Roderic S Lakes and Roderic Lakes. *Viscoelastic materials*. New York : Cambridge University Press, Cambridge, 2009.

[72] Juliet Lee, Michelle Leonard, Tim Oliver, Akira Ishihara, and Ken Jacobson. Traction forces generated by locomoting keratocytes. *The Journal of cell biology*, 127(6):1957–1964, 1994.

[73] Giuseppe Lippi, Emmanuel J Favaloro, Massimo Franchini, and Gian Cesare Guidi. Milestones and perspectives in coagulation and hemostasis. *Seminars in thrombosis and hemostasis*, 35(1):922, February 2009.

[74] JA Lopez Perez, MA Lopez Quintela, J Mira, J Rivas, and SW Charles. Advances in the preparation of magnetic nanoparticles by the microemulsion method. *The Journal of Physical Chemistry B*, 101(41):8045–8047, 1997.

[75] M Arturo Lpez-Quintela and Jos Rivas. Nanoscale magnetic particles: synthesis, structure and dynamics. *Current Opinion in Colloid & Interface Science*, 1(6):806–819, 1996.

[76] R. J. Luddington. Thrombelastography/thromboelastometry. *Clinical & Laboratory Haematology*, 27(2):81–90, April 2005.

[77] A. Magnin and J.M. Piau. Cone-and-plate rheometry of yield stress fluids. study of an aqueous gel. *Journal of Non-Newtonian Fluid Mechanics*, 36(0):85–108, 1990.

[78] Vernica C Martins, Jos Germano, Filipe A Cardoso, Joana Loureiro, Susana Cardoso, Leonel Sousa, Moiss Piedade, Lus P Fonseca, and PP Freitas. Challenges and trends in the development of a magnetoresistive biochip portable platform. *Journal of Magnetism and Magnetic Materials*, 322(9):1655–1663, 2010.

[79] Anurag Mathur, Peter Loskill, Kaifeng Shao, Nathaniel Huebsch, SoonGweon Hong, Sivan G Marcus, Natalie Marks, Mohammad Mandegar, Bruce R Conklin, and Luke P Lee. Human ipsc-based cardiac microphysiological system for drug screening applications. *Scientific reports*, 5:–, 2015.

[80] Patrick D McGary, Liwen Tan, Jia Zou, Bethanie JH Stadler, Patrick R Downey, and Alison B Flatau. Magnetic nanowires for acoustic sensors. *Journal of Applied Physics*, 99(8):08B310–, 2006.

[81] Ashish Mehta, Ying Ying Chung, Alvin Ng, Fahamy Iskandar, Shirhan Atan, Heming Wei, Greg Dusting, William Sun, Philip Wong, and Winston Shim. Pharmacological response of human cardiomyocytes derived from virus-free induced pluripotent stem cells. *Cardiovascular research*, 91(4):577–586, 2011.

[82] G Mihajlovi, A Hoffmann, and S von Molnar. Micro-hall position sensing of magnetic nanowires. *Journal of Applied Physics*, 106(7):074518–, 2009.

[83] MW Mosesson. Fibrinogen and fibrin structure and functions. *Journal of Thrombosis and Haemostasis*, 3(8):1894–1904, 2005.

[84] Enrique G Navarrete, Ping Liang, Feng Lan, Vernica Sanchez-Freire, Chelsey Simmons, Tingyu Gong, Arun Sharma, Paul W Burridge, Bhagat Patlolla, and Andrew S Lee. Screening drug-induced arrhythmia using human induced pluripotent stem cellderived cardiomyocytes and low-impedance microelectrode arrays. *Circulation*, 128(11 suppl 1):S3–S13, 2013.

[85] Warwick S Nesbitt, Erik Westein, Francisco Javier Tovar-Lopez, Elham Tolouei, Arnan Mitchell, Jia Fu, Josie Carberry, Andreas Fouras, and Shaun P Jackson. A shear gradientdependent platelet aggregation mechanism drives thrombus formation. *Nature medicine*, 15(6):665–673, 2009.

[86] Matteo Nobili, Jawaad Sheriff, Umberto Morbiducci, Alberto Redaelli, and Danny Bluestein. Platelet activation due to hemodynamic shear stresses: damage accumulation model and comparison to in vitro measurements. *ASAIO journal (American Society for Artificial Internal Organs: 1992)*, 54(1):64–, 2008.

[87] Kentaro Noda, Kazunori Hoshino, Kiyoshi Matsumoto, and Isao Shimoyama. A shear stress sensor for tactile sensing with the piezoresistive cantilever standing in elastic material. *Sensors and Actuators A: physical*, 127(2):295–301, 2006.

[88] Gordana Vunjak Novakovic, Thomas Eschenhagen, and Christine Mummery. Myocardial tissue engineering: in vitro models. *Cold Spring Harbor perspectives in medicine*, 4(3):a014076–, 2014.

[89] Tao Peng. Detect circles with various radii in grayscale image via hough transform, 2005.

[90] Sophie L. Peterson, Anthony McDonald, Paul L. Gourley, and Darryl Y. Sasaki. Poly(dimethylsiloxane) thin films as biocompatible coatings for microfluidic devices: Cell culture and flow studies with glial cells. *Journal of Biomedical Materials Research Part A*, 72A(1):10–18, 2005.

[91] Frank Pillekamp, Moritz Haustein, Markus Khalil, Markus Emmelheinz, Rewa Nazzal, Roland Adelmann, Filomain Nguemo, Olga Rubenchyk, Kurt Pfannkuche, and Matthias Matzkies. Contractile properties of early human embryonic stem cell-derived cardiomyocytes: beta-adrenergic stimulation induces positive chronotropy and lusitropy but not inotropy. *Stem cells and development*, 21(12):2111–2121, 2012.

[92] Gary A Prinz. Magnetoelectronics. *Science*, 282(5394):1660–1663, 1998.

[93] L. M. Rebelo, J. S. de Sousa, J. Mendes, J. Schape, H. Doschke, and M. Radmacher. Microrheology of cells with magnetic force modulation atomic force microscopy. *Soft Matter*, 10(13):2141–2149, 2014.

[94] Alexandre J.S. Ribeiro, Aleksandra K. Denisin, Robin E. Wilson, and Beth L. Pruitt. For whom the cells pull: Hydrogel and micropost devices for measuring traction forces. *Methods*, pages –, 2015.

[95] Marita L Rodriguez, Brandon T Graham, Lil M Pabon, Sangyoon J Han, Charles E Murry, and Nathan J Sniadecki. Measuring the contractile forces of human induced pluripotent stem cell-derived cardiomyocytes with arrays of microposts. *Journal of biomechanical engineering*, 136(5):051005–, 2014.

[96] Bryan A Roecklein and B Torok-Storb. Functionally distinct human marrow stromal cell lines immortalized by transduction with the human papilloma virus e6/e7 genes. *Blood*, 85(4):997–1005, 1995.

[97] B. A. Roeder, K. Kokini, J. E. Sturgis, J. P. Robinson, and S. L. Voytik-Harbin. Tensile mechanical properties of three-dimensional type i collagen extracellular matrices with varied microstructure. *J Biomech Eng*, 124(2):214–22, 2002.

[98] Michael M Rooney, Leslie V Parise, and Susan T Lord. Dissecting clot retraction and platelet aggregation clot retraction does not require an intact fibrinogen chain c terminus. *Journal of Biological Chemistry*, 271(15):8553–8555, 1996.

[99] Jesse W Rowley, Aloke V Finn, Patricia A French, Lisa K Jennings, Danny Bluestein, Peter L Gross, Jane E Freedman, Steven R Steinhubl, Guy A Zimmerman, and Richard C Becker. Cardiovascular devices and platelet interactions understanding the role of injury, flow, and cellular responses. *Circulation: Cardiovascular Interventions*, 5(2):296–304, 2012.

[100] JiaLing Ruan, Nathaniel L Tulloch, Mark Saiget, Sharon L Paige, Maria V Razumova, Michael Regnier, Kelvin Chan Tung, Gordon Keller, Lil Pabon, and Hans Reinecke. Mechanical stress promotes maturation of human myocardium from pluripotent stem cellderived progenitors. *Stem Cells*, 33(7):2148–2157, 2015.

[101] Kjell S Sakariassen, PA Aarts, Ph G De Groot, WP Houdijk, and JJ Sixma. A perfusion chamber developed to investigate platelet interaction in flowing blood with human vessel wall cells, their extracellular matrix, and purified components. *The Journal of laboratory and clinical medicine*, 102(4):522–535, 1983.

[102] Ajith Sankarankutty, Bartolomeu Nascimento, Luis Teodoro da Luz, and Sandro Rizoli. Teg() and rotem() in trauma: similar test but different results? *World Journal of Emergency Surgery : WJES*, 7(Suppl 1):S3–S3, August 2012.

[103] Sebastian Schaaf, Alexandra Eder, Ingra Vollert, Andrea Sthr, Arne Hansen, and Thomas Eschenhagen. Generation of strip-format fibrin-based engineered heart tissue (eht). *Cardiac Tissue Engineering: Methods and Protocols*, pages 121–129, 2014.

[104] Sebastian Schaaf, Aya Shibamiya, Marco Mewe, Alexandra Eder, Andrea Sthr, Marc N Hirt, Thomas Rau, Wolfram-Hubertus Zimmermann, Lenard Conradi, and Thomas Eschenhagen. Human engineered heart tissue as a versatile tool in basic research and preclinical toxicology. *PloS one*, 6(10):e26397–, 2011.

[105] Kelly M. Schultz and Eric M. Furst. Microrheology of biomaterial hydrogelators. *Soft Matter*, 8:6198–6205, 2012.

[106] J. B. Segur and H. E. Oberstar. Viscosity of glycerol and its aqueous solutions. *Industrial and Engineering Chemistry*, 43(9):2117–2120, 1951.

[107] Boris Shenkman, Naphtali Savion, Rima Dardik, Ilya Tamarin, and David Varon. Testing of platelet deposition on polystyrene surface under flow conditions by the cone and plate (let) analyzer: role of platelet activation, fibrinogen and von willebrand factor. *Thrombosis research*, 99(4):353–361, 2000.

[108] Jawaad Sheriff, Joo Silva Soares, Michalis Xenos, Jolyon Jesty, and Danny Bluestein. Evaluation of shear-induced platelet activation models under constant and dynamic shear stress loading conditions relevant to devices. *Annals of biomedical engineering*, 41(6):1279–1296, 2013.

[109] Ming-Thau Sheu, Ju-Chun Huang, Geng-Chang Yeh, and Hsiu-O Ho. Characterization of collagen gel solutions and collagen matrices for cell culture. *Biomaterials*, 22(13):1713 – 1719, 2001.

[110] Zhiwei Shi and Amy V Walker. Synthesis of nickel nanowires via electroless nanowire deposition on micropatterned substrates. *Langmuir*, 27(18):11292–11295, 2011.

[111] Masashige Shinkai. Functional magnetic particles for medical application. *Journal of bioscience and bioengineering*, 94(6):606–613, 2002.

[112] Constance L Slaboch, Mark S Alber, Elliot D Rosen, and Timothy C Ovaert. Mechanorheological properties of the murine thrombus determined via nanoindentation and finite element modeling. *Journal of the mechanical behavior of biomedical materials*, 10:75–86, 2012.

[113] N. J. Sniadecki, A. Anguelouch, M. T. Yang, C. M. Lamb, Z. Liu, S. B. Kirschner, Y. Liu, D. H. Reich, and C. S. Chen. Magnetic microposts as an approach to apply forces to living cells. *Proceedings of the National Academy of Sciences of the United States of America*, 104(37):14553–14558, 2007.

[114] Nicholas Sperelakis. Electrophysiology of calcium antagonists. *Journal of molecular and cellular cardiology*, 19:19–47, 1987.

[115] Andrew M. Stein, David A. Vader, David A. Weitz, and Leonard M. Sander. The micromechanics of three-dimensional collagen-i gels. *Complexity*, 16(4):22–28, 2011.

[116] Andrea Stoehr, Christiane Neuber, Christina Baldauf, Ingra Vollert, Felix W Friedrich, Frederik Flenner, Lucie Carrier, Alexandra Eder, Sebastian Schaaf, and Marc N Hirt. Automated analysis of contractile force and ca2+ transients in engineered heart tissue. *American Journal of Physiology-Heart and Circulatory Physiology*, 306(9):H1353–H1363, 2014.

[117] John L Tan, Joe Tien, Dana M Pirone, Darren S Gray, Kiran Bhadriraju, and Christopher S Chen. Cells lying on a bed of microneedles: an approach to isolate mechanical force. *Proceedings of the National Academy of Sciences*, 100(4):1484–1489, 2003.

[118] Tomofumi Tanaka, Shugo Tohyama, Mitsushige Murata, Fumimasa Nomura, Tomoyuki Kaneko, Hao Chen, Fumiyuki Hattori, Toru Egashira, Tomohisa Seki, and Yohei Ohno. In vitro pharmacologic testing using human induced pluripotent stem cell-derived cardiomyocytes. *Biochemical and biophysical research communications*, 385(4):497–502, 2009.

[119] Monica Tanase, Edward J Felton, Darren S Gray, Anne Hultgren, Christopher S Chen, and Daniel H Reich. Assembly of multicellular constructs and microarrays of cells using magnetic nanowires. *Lab on a Chip*, 5(6):598–605, 2005.

[120] Jos Miguel Teixeira, Joo Oliveira Ventura, Rui Pedro Fermento, Joo Pedro Arajo, Joo Bessa Sousa, Susana Cardoso Freitas, and Paulo Jorge Freitas. Interlayer coupling and magnetoresistance of mnir-based spin valves: Dependencies on deposition rate, spacer thickness, and temperature. *IEEE transactions on magnetics*, 43(7):3143–3145, 2007.

[121] Lucas Ting, Shirin Feghhi, Ari Karchin, Wes Tooley, and Nathan J White. Clot-on-a-chip: A microfluidic device to study platelet aggregation and contractility under shear. *Blood*, 122(21):2363–2363, 2013.

[122] Yiider Tseng, Thomas P. Kole, and Denis Wirtz. Micromechanical mapping of live cells by multiple-particle-tracking microrheology. *Biophysical Journal*, 83(6):3162–3176, December 2002.

[123] Nathaniel L Tulloch, Veronica Muskheli, Maria V Razumova, F Steven Korte, Michael Regnier, Kip D Hauch, Lil Pabon, Hans Reinecke, and Charles E Murry. Growth of engineered human myocardium with mechanical loading and vascular coculture. *Circulation research*, 109(1):47–59, 2011.

[124] Evangeline Tzatzalos, Oscar J Abilez, Praveen Shukla, and Joseph C Wu. Engineered heart tissues and induced pluripotent stem cells: Macro-and microstructures for disease modeling, drug screening, and translational studies. *Advanced drug delivery reviews*, 96:234–244, 2016.

[125] Zsolt Varga, Genovva Filipcsei, and Mikls Zrnyi. Magnetic field sensitive functional elastomers with tuneable elastic modulus. *Polymer*, 47(1):227–233, January 2006.

[126] Antti Virta, Jaakko VI Timonen, Robin HA Ras, and Quan Zhou. Force sensing using artificial magnetic cilia. In *Intelligent Robots and Systems (IROS), 2012 IEEE/RSJ International Conference on*, pages 1–6. IEEE, 2012.

[127] N Wang, JP Butler, and DE Ingber. Mechanotransduction across the cell surface and through the cytoskeleton. *Science*, 260(5111):1124–1127, May 1993.

[128] Daphne Weihs, Thomas G Mason, and Michael A Teitell. Bio-microrheology: A frontier in microrheology. *Biophysical Journal*, 91(11):4296–4305, August 2006.

[129] Nathan J. White, Erika J. Martin, Donald F. Brophy, and Kevin R. Ward. Examining platelet-fibrin interactions during traumatic shock in a swine model using platelet contractile force and clot elastic modulus. *Blood Coagulation & Fibrinolysis*, 22(5):379–387, July 2011.

[130] Nathan J White, Jason C Newton, Erika J Martin, Bassem M Mohammed, Daniel Contaifer Jr, Jessica L Bostic, Gretchen M Brophy, Bruce D Spiess, Anthony E Pusateri, and Kevin R Ward. Clot formation is associated with fibrinogen and platelet forces in a cohort of severely-injured emergency department trauma patients. *Shock (Augusta, Ga.)*, pages –, 2015.

[131] Withrow Gil Wier and Matthew N. Levy, editors. *Cardiovascular Physiology.* London : Elsevier Health Sciences, London, 2013.

[132] Laurence G. Wilson and Wilson C. K. Poon. Small-world rheology: an introduction to probe-based active microrheology. *Phys. Chem. Chem. Phys.*, 13:10617–10630, 2011.

[133] Banqiu Wu, Ajay Kumar, and Sharma Pamarthy. High aspect ratio silicon etch: a review. *Journal of applied physics*, 108(5):051101, 2010.

[134] Jiaoya Xi, Markus Khalil, Nava Shishechian, Tobias Hannes, Kurt Pfannkuche, Huamin Liang, Azra Fatima, Moritz Haustein, Frank Suhr, and Wilhelm Bloch. Comparison of contractile behavior of native murine ventricular tissue and cardiomyocytes derived from embryonic or induced pluripotent stem cells. *The FASEB Journal*, 24(8):2739–2751, 2010.

[135] Younan Xia and George M Whitesides. Soft lithography. *Annual review of materials science*, 28(1):153–184, 1998.

[136] Younan Xia, Peidong Yang, Yugang Sun, Yiying Wu, Brian Mayers, Byron Gates, Yadong Yin, Franklin Kim, and Haoquan Yan. One-dimensional nanostructures: synthesis, characterization, and applications. *Advanced materials*, 15(5):353–389, 2003.

[137] Shaoguang Yang, Hao Zhu, Dongliang Yu, Zhiqiang Jin, Shaolong Tang, and Youwei Du. Preparation and magnetic property of fe nanowire array. *Journal of Magnetism and Magnetic Materials*, 222(1):97–100, 2000.

[138] Xiulan Yang, Lil Pabon, and Charles E Murry. Engineering adolescence maturation of human pluripotent stem cellderived cardiomyocytes. *Circulation research*, 114(3):511–523, 2014.

[139] Ya-li Yang, Lindsay M. Leone, and Laura J. Kaufman. Elastic moduli of collagen gels can be predicted from two-dimensional confocal microscopy. *Biophysical Journal*, 97(7):2051–2060, 2009.

[140] Donghui Zhang, Ilya Y Shadrin, Jason Lam, Hai-Qian Xian, H Ralph Snodgrass, and Nenad Bursac. Tissue-engineered cardiac patch for advanced functional maturation of human esc-derived cardiomyocytes. *Biomaterials*, 34(23):5813–5820, 2013.

[141] Jianhua Zhang, Gisela F Wilson, Andrew G Soerens, Chad H Koonce, Junying Yu, Sean P Palecek, James A Thomson, and Timothy J Kamp. Functional cardiomyocytes derived from human induced pluripotent stem cells. *Circulation research*, 104(4):e30–e41, 2009.

[142] Wenru Zhao, Jinlou Gu, Lingxia Zhang, Hangrong Chen, and Jianlin Shi. Fabrication of uniform magnetic nanocomposite spheres with a magnetic core/mesoporous silica shell structure. *Journal of the American Chemical Society*, 127(25):8916–8917, 2005.

[143] Wolfram-Hubertus Zimmermann, Michael Didi, Gerald H Wasmeier, Uwe Nixdorff, Andreas Hess, Ivan Melnychenko, Oliver Boy, Winfried L Neuhuber, Michael Weyand, and Thomas Eschenhagen. Cardiac grafting of engineered heart tissue in syngenic rats. *Circulation*, 106(12 suppl 1):I–151, 2002.